

Spring 5-14-2016

Improvement of Soil Spring Model for the Analysis of Buried Arch Structures

Leo N. Helderma

University of Maine, leohelderma@gmail.com

Follow this and additional works at: <http://digitalcommons.library.umaine.edu/etd>



Part of the [Civil Engineering Commons](#)

Recommended Citation

Helderma, Leo N., "Improvement of Soil Spring Model for the Analysis of Buried Arch Structures" (2016). *Electronic Theses and Dissertations*. 2437.

<http://digitalcommons.library.umaine.edu/etd/2437>

This Open-Access Thesis is brought to you for free and open access by DigitalCommons@UMaine. It has been accepted for inclusion in Electronic Theses and Dissertations by an authorized administrator of DigitalCommons@UMaine.

**IMPROVEMENT OF SOIL SPRING MODEL FOR THE ANALYSIS OF
BURIED ARCH STRUCTURES**

By

Leo N. Helderma

B.S. University of Maine, 2014

A THESIS

Submitted in Partial Fulfillment of the

Requirements for the Degree of

Master of Science

(in Civil Engineering)

The Graduate School

The University of Maine

May 2016

Advisory Committee:

William G. Davids, Professor of Civil Engineering, Advisor

Melissa E. Landon, Associate Professor of Civil Engineering

Eric N. Landis, Professor of Civil Engineering

THESIS ACCEPTANCE STATEMENT

On behalf of the Graduate Committee for Leo Helderman, I affirm that this manuscript is the final accepted thesis. Signatures of all committee members are on file with the Graduate School at the University of Maine, 5755 Stodder Hall, Orono Maine 04469.

Dr. William G. Davids
Professor of Civil Engineering
Chair

Date

Copyright 2016 Leo N. Helderan

All Rights Reserved

LIBRARY RIGHTS STATEMENT

In presenting this thesis in partial fulfillment of the requirements for an advanced degree at the University of Maine, I agree that the Library shall make it freely available for inspection. I further agree that permission for “fair use” copying of this thesis for scholarly purposes may be granted by the Librarian. It is understood that any copying or publication of this thesis for financial gain shall not be allowed without my written permission.

Signature:

Date:

IMPROVEMENT OF SOIL SPRING MODEL FOR THE ANALYSIS OF BURIED ARCH STRUCTURES

By: Leo N. Helderma

Thesis Advisor: William Davids

An Abstract of the Thesis Presented
in Partial Fulfillment of the Requirements for the
Degree of Master of Science
(in Civil Engineering)
May, 2016

The University of Maine has developed concrete filled fiber-reinforced polymer (FRP) tubes (CFFTs) for use in bridge construction. A finite element model was previously developed to analyze these buried arch structures during construction, service live load, and ultimate load. Two shortcomings in that model include how the load distribution method and the soil reaction due to construction and service loads are modeled. There were two objectives to this research: to make a user-friendly software package to analyze a variety of buried arch structures and to improve the existing model to better predict the soil-structure interaction. Prototype software was developed complete with a graphical user interface using the existing model to allow engineers a tool to analyze a variety of materials, arch geometries, and soil conditions to predict the effect of diverse load cases. Changes to the model were planned to improve the model's ability to capture the response of the soil due to arch deformation and produce more efficient arch designs. A Boussinesq stress distribution was used in the model to predict the dispersal of the load through the soil. Load distribution was investigated and compared to a previous experimental work and soil-continuum models to gain insight on

the shortcomings of the existing load distribution model used in the analysis. The existing model used a horizontal soil-spring configuration with a nonlinear load-deflection relationship. Three changes to the soil-springs in the existing model were considered: radial soil-springs, friction angle soil-springs, and a three spring system. These alternative soil-spring models were implemented in place of the existing horizontal soil-springs and the arch internal moments and deflections were compared to the existing model and experimental results.

ACKNOWLEDGEMENTS

I would like to thank my advisors Bill Davids and Melissa Landon for their support, guidance and contributions throughout my graduate studies. I would like to thank my committee for their time and attention in reviewing this thesis and throughout this project.

Thanks to my friends and family for their support throughout my time at the University of Maine.

Funding that made this research possible was provided by Engineer Research and Development Center (ERDC).

TABLE OF CONTENTS

ACKNOWLEDGEMENTS.....	iv
LIST OF TABLES.....	xi
LIST OF FIGURES	xii
CHAPTER 1 INTRODUCTION.....	1
1.1. Background.....	1
1.1.1. Chapter Overviews.....	2
1.1.2. Chapter 2. Background Information	2
1.1.3. Chapter 3. Development of Prototype Analysis Software.....	3
1.1.4. Chapter 4. Existing Model and Methods for Improvement.....	3
1.1.5. Chapter 5. Results	4
1.1.6. Chapter 6. Conclusions	5
CHAPTER 2 BACKGROUND INFORMATION.....	6
2.1. Introduction.....	6
2.2. Modeling Soils and Soil Structure Interaction.....	6
2.3. Load Distribution.....	7
2.4. Review of Previous Work by Walton et al.	8
2.4.1. Experimental Work.....	8
2.4.1.1. Soil Box	8
2.4.1.2. Soil.....	9

2.4.1.3. Arches	9
2.4.1.4. Decking.....	10
2.4.1.5. Instrumentation	11
2.4.1.6. Loading Cases.....	11
2.4.2. Simulation.....	13
2.4.2.1. Soil-Spring Model.....	13
2.4.2.1.1. Soil-Springs.....	14
2.4.2.1.2. Arch Elements.....	15
2.4.2.1.3. Foundation	15
2.4.2.1.4. Backfilling.....	16
2.4.2.1.5. Live Load Application	16
2.4.2.1.6. Ultimate Load	17
2.4.2.2. ABAQUS Continuum Model.....	17
2.4.3. Conclusions.....	18
CHAPTER 3 DEVELOPMENT OF A USER-FRIENDLY ANALYSIS TOOL.....	20
3.1. Introduction.....	20
3.2. Overview of <i>CBAS Design</i>	20
3.3. Assumptions in the Model	23
3.4. Verification of Soil-Spring Design Software.....	24
3.4.1. Tall Arch Comparison.....	25

3.4.1.1. Backfilling.....	25
3.4.1.2. Apex Service Load.....	26
3.4.2. Short Arch Comparison	27
3.4.2.1. Backfilling.....	27
3.4.2.2. Apex Service Load.....	28
3.4.3. Simulation Test Structure	29
3.4.4. Mesh Convergence Study	30
3.4.5. Small vs. Large Deformation.....	31
3.4.6. Sensitivity to Soil Parameters	32
3.4.7. Effect of Different Lift Heights	34
3.5. Summary and Conclusions	35
CHAPTER 4 PROPOSED IMPROVEMENTS TO THE EXISTING MODEL.....	36
4.1. Introduction.....	36
4.2. Assessment of Load Distribution Model	36
4.2.1. Description of the Finite Element Models	38
4.2.2. Model Comparisons to Experimental Results.....	39
4.2.2.1. Backfill Results.....	40
4.2.2.2. Apex Service Load Results.....	42
4.2.2.3. Offset Service Load Results.....	43
4.2.3. Load Distribution Conclusions	47

4.3. Existing Soil-Spring Model	48
4.4. Proposed Modifications to the Existing Model	51
4.4.1. Implementation of Angled Soil-springs.....	52
4.4.1.1. Radial Springs.....	53
4.4.1.2. Friction Angle Springs.....	54
4.4.2. Three Spring Model	55
4.4.2.1. Modification to the Three Spring Model	59
4.4.2.2. Error in Three Spring Method.....	61
4.4.3. Implemented Modifications to the Model.....	63
4.5. Conclusions.....	64
 CHAPTER 5 MODEL PREDICTIONS AND COMPARISONS WITH EXPERIMENTAL RESULTS.....	 65
5.1. Introduction.....	65
5.2. Model Description	65
5.3. Backfilling Response for the Short Arch.....	66
5.4. Backfilling Response for the Tall Arch	73
5.5. Live Load Response of Short Arch.....	78
5.5.1. Apex Service Live Load	78
5.5.2. 20% Offset Service Live Load.....	81
5.5.3. 40% Offset Service Live Load.....	83

5.5.4. 60% Offset Service Live Load.....	85
5.6. Live Load Response of the Tall Arch.....	88
5.6.1. Apex Service Live Load	89
5.6.2. 20% Service Offset Live Load.....	91
5.6.3. 40% Service Offset Live Load.....	93
5.6.4. 60% Service Offset Live Load.....	95
5.7. Ultimate Load Response	98
5.8. Conclusions.....	102
CHAPTER 6 CONCLUSIONS	103
6.1. Summary and Conclusions	103
6.2. Future Work.....	106
REFERENCES	108
APPENDIX A USERS MANUAL.....	110
Introduction and Program Overview	112
Installation and Running CBAS Design	112
Creating and Opening Existing Models.....	113
Structure Properties.....	115
Load Configuration.....	117
Analysis.....	119
Results.....	120

Comparison to Experimental Results.....	120
Step by Step Example	124
Output Database Description	129
Input File Description	130
USER'S MANUAL REFERENCES	133
BIOGRAPHY OF THE AUTHOR.....	134

LIST OF TABLES

Table 3.1 Mesh Convergence	31
Table 5.1 Error of Each Model Moment Results, Short Arch	88
Table 5.2 Error of Each Model Moment Results, Tall Arch	98
Table A.1 - Structural Properties of Model Buried Arch.....	122
Table A.2 - Load Configuration of Model Buried Arch.....	122
Table A.3 - Structural Properties for Example	125
Table A.4 - Load Configuration for Example.....	125

LIST OF FIGURES

Figure 1.1 Existing Soil-spring Model (Walton 2015 c)	1
Figure 2.1 Live Load Application Positions	12
Figure 3.1 Screenshot of <i>CBAS Design</i> Structure Properties Page.....	21
Figure 3.2 Tall Arch Backfill Moments.....	26
Figure 3.3 Tall Arch Backfill Displacements	26
Figure 3.4 Tall Arch Apex Load Moments.....	27
Figure 3.5 Tall Arch Apex Load Displacements	27
Figure 3.6 Short Arch Backfill Moments	28
Figure 3.7 Short Arch Backfill Displacements	28
Figure 3.8 Short Arch Apex Load Moments	29
Figure 3.9 Short Arch Apex Load Displacements	29
Figure 3.10 Test Structure entered into <i>CBAS Design</i>	30
Figure 3.11 Error for varying number of elements, Mesh Convergence	31
Figure 3.12 Small vs Large Deformation Backfill Moments	32
Figure 3.13 Small vs Large Deformation Apex Load Moments	32
Figure 3.14 Effect of Different Soil Compaction, Backfill Moments	33
Figure 3.15 Effect of Different Soil Compaction, Apex Load Moments	33
Figure 3.16 Effect of Different Lift Heights, Backfill Moments.....	35
Figure 3.17 Effect of Different Lift Heights, Horizontal Earth Pressure Coefficient.....	35
Figure 4.1 Simulated Boussinesq Model Mesh	37
Figure 4.2 Soil Structure Interaction Mesh.....	38
Figure 4.3 Simulated Boussinesq Soil Stress Due to an Apex Load	40

Figure 4.4 SSI Soil Stress Due to an Apex Load.....	40
Figure 4.5 Short Arch Backfill Vertical Pressure	41
Figure 4.6 Tall Arch Backfill Vertical Pressure	41
Figure 4.7 Short Arch Apex Service Load Vertical Pressure	42
Figure 4.8 Tall Arch Apex Service Load Vertical Pressure	43
Figure 4.9 Short Arch 20% Offset Service Load Vertical Pressure	44
Figure 4.10 Short Arch 40% Offset Service Load Vertical Pressure	45
Figure 4.11 Short Arch 60% Offset Service Load Vertical Pressure	45
Figure 4.12 Tall Arch 20% Offset Service Load Vertical Pressure.....	46
Figure 4.13 Tall Arch 40% Offset Service Load Vertical Pressure.....	47
Figure 4.14 Tall Arch 60% Offset Service Load Vertical Pressure.....	47
Figure 4.15 Existing Model (Walton 2015c)	48
Figure 4.16 Soil Response Predicted Using NCHRP (1991).....	49
Figure 4.17 Horizontal Spring and Projected Arch Area.....	51
Figure 4.18 Angled Spring and Projected Arch Area	53
Figure 4.19 Radial Spring Model.....	54
Figure 4.20 Friction Angle Spring Model.....	55
Figure 4.21 Three Spring Model.....	56
Figure 4.22 Three-Spring Model Arch Node, Soil-springs, and Deflection.....	56
Figure 4.23 Soil-spring Deflection Limits	57
Figure 4.24 Spring Interpolation for Three Spring Model.....	59
Figure 4.25 Quadratic Spring Interpolation in the Three Spring Model.....	61
Figure 4.26 Normalized Spring Force vs Relative Deflection.....	63

Figure 5.1 Short Arch Backfilling Moments at Apex.....	68
Figure 5.2 Short Arch Backfilling Moments at Foundation	69
Figure 5.3 Short Arch Backfilling Moments at Shoulder	70
Figure 5.4 Short Arch End of Backfill Moment	71
Figure 5.5 Short Arch End of Backfill Moment, Three Spring Model Comparison	72
Figure 5.6 Short Arch End of Backfill Vertical Displacement.....	73
Figure 5.7 Tall Arch Backfilling Moments at Apex.....	74
Figure 5.8 Tall Arch Backfilling Moments at Foundation	75
Figure 5.9 Tall Arch Backfilling Moments at Shoulder	76
Figure 5.10 Tall Arch End of Backfill Moment	77
Figure 5.11 Tall Arch End of Backfill Vertical Displacement	78
Figure 5.12 Short Arch Apex Service Load Moments	79
Figure 5.13 Short Arch Apex Service Load Moment, Three Spring Model Comparison	80
Figure 5.14 Short Arch Apex Service Load Vertical Displacement.....	81
Figure 5.15 Short Arch 20% Offset Service Load Moments.....	82
Figure 5.16 Short Arch 20% Offset Service Load Vertical Displacement.....	83
Figure 5.17 Short Arch 40% Offset Service Load Moments.....	84
Figure 5.18 Short Arch 40% Offset Service Load Vertical Displacement.....	85
Figure 5.19 Short Arch 60% Offset Service Load Moments.....	86
Figure 5.20 Short Arch 60% Offset Service Load Vertical Displacement.....	87
Figure 5.21 Tall Arch Apex Service Load Moments.....	90
Figure 5.22 Tall Arch Apex Service Load Vertical Displacement.....	91

Figure 5.23 Tall Arch 20% Offset Service Load Moments	92
Figure 5.24 Tall Arch 20% Offset Service Load Vertical Displacements.....	93
Figure 5.25 Tall Arch 40% Offset Service Load Moments	94
Figure 5.26 Tall Arch 40% Offset Service Load Vertical Displacements.....	95
Figure 5.27 Tall Arch 60% Offset Service Load Moments	96
Figure 5.28 Tall Arch 60% Offset Service Load Vertical Displacements.....	97
Figure 5.29 Short Arch Ultimate Load Moments	100
Figure 5.30 Tall Arch Ultimate load Moments.....	101
Figure A.1 CBAS Design Directory	112
Figure A.2 Initial View of CBAS Design, Structure Properties Tab.....	114
Figure A.3 Load Configuration Tab	118
Figure A.4 Analysis Tab	119
Figure A.5 Tall Arch Backfill Moments.....	124
Figure A.6 Tall Arch Backfill Displacements	124
Figure A.7 Tall Arch Apex Load Moments.....	124
Figure A.8 Tall Arch Apex Load Displacements	124
Figure A.9 Structure Properties, Example Verification.....	126
Figure A.10 Load Configuration, Example Verification.....	127
Figure A.11 Analysis, Example Verification.....	128
Figure A.12 Analysis in Progress	128
Figure A.13 Results Tab, Moment Visualization	129

CHAPTER 1

INTRODUCTION

1.1. Background

Concrete filled fiber reinforced polymer (FRP) tube (CFFT) arches are seeing increased use as the main structural member in bridges since their development at the University of Maine (Walton 2015 c, Bannon 2007). A straightforward model was developed by Clapp and Davids (2011) to analyze soil-structure interaction of these buried arch structures. The model used small deformation and nonlinear, overburden- and deformation-dependent springs to represent soil reactions. Walton et al. (2015 a,b,c) tested a scaled version of the CFFT bridges and improved the previous model by implementing large deformations and more sophisticated foundations models. The existing soil-spring model is illustrated in Figure 1.1 and shows the arch, soil-spring, and foundation elements. A coarse mesh is shown for clarity. This method of using a 2-D finite element model using soil-springs is computationally efficient, resulting in shorter run times, and also yields comparable results to more advanced methods of modeling soils, such as 2-D nonlinear continuum models.

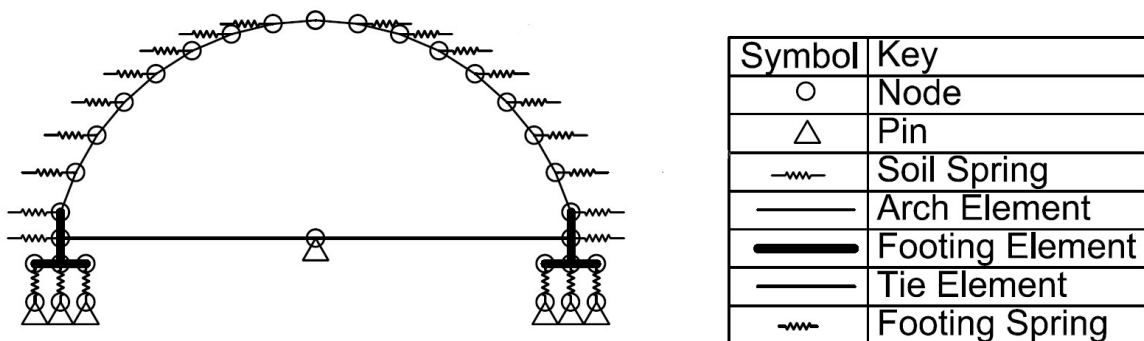


Figure 1.1 Existing Soil-spring Model (Walton 2015 c)

The two objectives of this thesis were to develop user-friendly prototype analysis software and improve model response in comparison to experimentally gathered moments and deflections to produce more efficient arch designs. The Existing Model, as improved by Walton (2015 c), was a research tool, and was not intuitive to use. The prototype software package will allow engineers to analyze buried arch structures of various geometric and material properties through an intuitive user interface. While the Existing Model adequately predicted the arch response during certain load steps (e.g. backfilling and apex service loading), improvements should be made to improve model results for all load cases to obtain more realistic response.

1.1.1. Chapter Overviews

This thesis consists of six chapters. Chapter 2 contains background information; Chapter 3 addresses the development of the prototype software; Chapter 4 addresses the improvements being made; Chapter 5 contains model results and comparisons to previous modeling and experimental work; and Chapter 6 contains a summary and recommendations for future work.

1.1.2. Chapter 2. Background Information

Chapter 2 contains the essential background information that was the basis of the model improvements and the prototype software. Information is given on the basic assumptions of the model such as the Boussinesq live load distribution, National Cooperative Highway Research Program (NCHRP) Report 343s (Barker et al. 1991) nonlinear soil load-deformation relationship, and a summary of the experimental and simulation work conducted by Walton et al. (2015 a,b,c).

1.1.3. Chapter 3. Development of Prototype Analysis Software

Chapter 3 details the development of the prototype analysis software for analyzing the buried arch structures. This chapter details the assumptions made by the analysis software to decrease the computational cost and increase software efficiency. The model used in the prototype software was compared to the Existing Model's predictions as well as the experimental results gathered from Walton (2015 c). Further studies on the prototype software included a mesh convergence, a parameter analysis on sensitivity of results to soil parameters, and the effect of varied lift heights.

1.1.4. Chapter 4. Existing Model and Methods for Improvement

Chapter 4 critically examines the Existing Model's live load distribution model and details planned improvements by changing the orientation of the soil-springs. The Boussinesq model is widely used to predict soil stresses on buried structures, though it assumes an infinite, linear elastic soil-continuum. The stress distribution model does not account for any obstructions in the soil, the change in soil elasticity with depth, or soil arching, situations that can possibly affect the stress distribution on a buried structures. To assess these factors, experimentally observed pressures were compared to pressures predicted by the Boussinesq distribution as well as a simple elastic finite element model that simulates the soil-structure interaction.

Four different options were considered to improve the predictions of the current soil-spring model: a Three Spring Model, Radial Spring Model, and a Friction Angle Spring Model. The Three Spring Model added friction between the soil and the arch based on Coulomb retaining wall design. Three soil-springs were attached to each arch node and the soil reaction was interpolated between the springs depending on the arch

deformation. Error was introduced into the model by interpolation between the three soil-springs, and a study was conducted to quantify this error. The Radial and Friction Angle Spring Models included angled springs that give the soil the ability to restrain the arch in the vertical directions. The Radial Spring Model orients the soil-springs radially away from the arch, and the Friction Angle Spring Model orients the soil-springs at the soil's characteristic friction angle, determined experimentally by Walton et al. (2015 a).

1.1.5. Chapter 5. Results

Chapter 5 contains comparisons between the results of the improved model detailed in Chapter 4 and the model predictions from Walton et al. (2015 b). Additionally, comparisons of model predictions and the experimental results gathered by Walton (2015 a) during the scale bridge tests are also presented. Each model was subject to the same load cases applied to the experimental scale bridge. The main structural arches in the models were made of steel to facilitate convergence and ensure the accuracy of critical experimental results.

Load cases included staged backfilling, service live loads applied at various positions over the center 60% of the span, and an ultimate live load applied at the apex. The backfill loading simulated the unsymmetric soil installation typically seen for buried arch structures. Lifts of consistent height were applied to alternating sides of the arch until the specified height of soil was achieved. The service load simulated a scaled HL-93 tandem typically used to design bridges applied as uniform strip loads at discrete locations along the span of the arch. Service Live Load results were calculated to only include the response of the structure to the service live load; the backfilling results were subtracted from the total load effect due to the backfilling and live load. The ultimate

load case featured an apex strip load that increased in magnitude until an irrecoverable loss in capacity of the arches was reached. Internal arch moments are the typically the critical design values for CFFT arches. Moment distributions along the span are presented for all load cases as well as moments at the apex, foundations, and shoulders during backfilling.

1.1.6. Chapter 6. Conclusions

Chapter 6 contains a summary and conclusions for each of the previous chapters as well as recommendations for future work.

CHAPTER 2

BACKGROUND INFORMATION

2.1. Introduction

This chapter introduces the concepts and ideas used in this research which include: soil-spring models, retaining wall design, and Boussinesq load distribution. In addition, previous experimental and modeling work discussed by Walton et al. (2015 a,b,c) was built upon and improved in later chapters.

2.2. Modeling Soils and Soil Structure Interaction

An effective way to model Soil Structure Interaction (SSI) is by using soil-spring models to capture the reactive forces and stresses acting on buried structures from the soil. Soil-spring models are also known as p-y models and have been used in applications such as piles (Reese and Wang 2006), retaining walls (Chen et al. 2010, Wang et al. 2013), and integral abutment bridges (Faraji 2001) to calculate critical design values. Soil-springs have been modeled as linear (Rani and Prashant 2014) or nonlinear (Barker et al. 1991, Faraji 2001, Chen et al. 2010). Previous buried arch modeling has implemented horizontal (Walton 2015 b) and radial (Bannon 2009) soil-springs.

In retaining wall design, reactive forces from the soil are calculated based on the movement of the retaining wall relative to the soil mass (Das 2011). To calculate the horizontal stress on a vertical retaining wall, the vertical stress due to the soil and the applied load is multiplied by the ratio of horizontal soil stress to vertical soil stress called the coefficient of lateral earth pressure (K). K values differ depending on the in situ soil state stress categorized into three cases: at-rest, active, and passive. For an at-rest soil state, which indicates that the wall is not moving relative to the soil, typical K values for

uncompacted granular fill are 0.3-0.5 (Barker et al. 1991) while compacted fill can be assumed to have a K value of 1 (Clough 1990). As a wall moves away from the soil, the soil enters an active soil state, lowering the K value and therefore the horizontal stress acting on the wall. Similarly, as a wall moves toward the soil, the soil enters a passive soil state, increasing the K value and the horizontal stress acting on the wall. Clough (1990) developed a K -deflection relationship that describes the horizontal stress on the wall as a nonlinear relationship dependent on the amount of movement into and out of the soil. This is further described in Chapters 3 and 4.

Two methods used to calculate the active and passive pressures were developed by Rankine and Coulomb (Barker et al. 1991, Das 2011) for granular cohesionless soils. The Rankine method to calculate the horizontal pressures assumes there is no friction between the soil and the wall, therefore a vertical wall will see only horizontal pressure. The Coulomb method assumes friction acts between the soil and the wall at the soil-wall friction angle (δ). Both methods assume a linear shear failure plane in the soil and the full shear strength of the soil is activated to counter the movement of the wall.

2.3. Load Distribution

Boussinesq Theory is a method to calculate the vertical stresses in soil by assuming the soil is linear elastic, homogeneous, and isotropic (Holtz et al. 2011). Although soil is not linear elastic, homogeneous, or isotropic, the Boussinesq method for calculating vertical soil stress is commonly accepted by engineers. Westergaard theory is used to calculate stress assuming discrete layers in the soil; however this method was not pursued since it would introduce complications in calculating stresses within the existing model.

2.4. Review of Previous Work by Walton et al.

Walton et al. (2015 a) conducted scale buried arch laboratory experiments and developed advanced finite element simulations to predict the response of these structures. The work completed by Walton et al. (2015 a,b) sets the groundwork for the research in this project. Data received through the experimental work was used as a baseline on which to base model improvements developed as part of this research were compared. Further, Walton et al. (2015 b) developed nonlinear soil-spring finite-element modeling strategies that were the basis for the models of this study. Walton's experimental program and an introduction of the developed model are explained in detail in the following sections.

2.4.1. Experimental Work

Four half-scale arch configurations were tested at the Advanced Structures and Composites Center at the University of Maine. The structures were made of three parallel arches set in concrete footings and topped with decking made of plywood. The arches were made of either plate steel or concrete filled composite tubes. The shell of the composite tubes were made of Fiber Reinforced Polymers (FRP) made of two layers of E-glass resulting with a laminate thickness of 1.9 mm, which were then filled with concrete to make the main structural members, a concrete-filled FRP tube (CFFT). Three phases of testing occurred to replicate the loads the structure would possibly see in the field: a staged backfill, service live loading, and loading to ultimate failure.

2.4.1.1. Soil Box

A self-reacting soil box was constructed in the Advanced Structures and Composites Center at the University of Maine to contain the soil. The soil box had inner

dimensions of 12.2 m long, 2.3 m wide, and 3.6 m deep. The walls were made of 100 mm by 100 mm rough sawn lumber supported vertically by 200 mm by 200 mm rough-sawn soldier beams. One end of the soil box was made of a modular vertical reaction wall that acted as a fixed boundary. The soil box was lined with low friction plastic to minimize friction between the soil and the timber walls.

2.4.1.2. Soil

Soil used for backfill was a scaled version of the typical soil used for backfilling CFFT arches. Soil classification typically used for fill for CFFT bridges is well-graded with 10% fines (e.g., passing the #200 sieve) and a maximum particle size less than 75 mm (Walton et al. 2015 a). To scale down the soil for the experiment, the maximum grain size was reduced to less than 25 mm to match a typical lift height scaled to 200 mm. Backfill soil was tested and classified as AASHTO A-1-a to A-1-b. The soil had an average of 37% gravel (particles 6.4 mm and larger), 61% sand, and 1% fines (passing the #200 sieve). The soil had an average dry density of 2.2 Mg/m^3 . The soil friction angle was measured between 42 and 44 degrees. Water content in the soil was measured between 2.5% and 7% with most specimens in the 3.5% to 4.5% range.

2.4.1.3. Arches

Two circular-segment arch geometry bridges were tested in the lab, a 1.2 m rise arch and a 2.3 m rise arch characterized ‘short’ and ‘tall’ respectively for the remainder of this thesis. Both arches spanned 20 feet. Two bridges of each geometry were constructed: one of steel and one of CFFT. Each bridge was comprised of three arches. Solid rectangular sections of grade 50 steel were designed to have the same stiffness as the CFFT member under service loading. The short steel arch cross-section was 50 mm

by 50 mm and the tall arch steel cross-section was 38 mm by 100 mm, oriented in weak axis bending. The steel sections were also designed to stay in the linear elastic region of the stress-strain relationship during service loading. The yield stress was determined experimentally to be 350 MPa. To scale the CFFT arches, the diameter was decreased from a typical 300-380 mm to 114 mm. The thickness of the shell was 1.9 mm and was made up of two layers of E-glass, an inner layer with a bias angle of ± 75 degrees and an outer layer with a bias angle of ± 25 degrees.

The three arches were cast into the center of a single footing at either end. The footings were supported by the lab's concrete reaction floor with a layer of OSB and two layers of low-friction HDPE pads between the footings and the concrete floor. The layers of low-friction material were included to reduce the effect of shear transfer between the footing and the concrete floor, mimicking the effect of piles supporting the arch foundations. A tie was used during backfilling and a selection of service load tests, to support the arches from collapse, allow the arches to be self-reacting, and minimize the foundation spread. The ties represented the resistance the footings would have seen between the footing and the soil under the footing.

2.4.1.4. Decking

Wooden decking spanned the three arches at a spacing of 760 mm on center. The decking was designed as a continuous span, supported by each of the three arches. The overhang at each end was designed so that the deck would have theoretically no rotation at the arches under a uniform load. The stiffness of the decking was designed to be intermediate between that of concrete and FRP decking typically used in CFFT construction.

2.4.1.5. Instrumentation

The bridges were instrumented with over 100 sensors, most of which were distributed at 1/8th points along the arch length. Each arch was equipped with strain gauges at these points along the arc length at the top, bottom, and center of the sections to allow axial forces, moments and curvatures to be calculated in post processing. Total Pressure Cells (TPCs) were positioned during backfilling to capture the soil pressures in different directions. For the tall steel arch, TPCs were positioned to capture the horizontal and vertical pressures on half of the arch and radial pressures on the other half. Due to difficulties placing the pressure cells accurately during the tall steel arch test, pressure cells were placed in horizontal and vertical directions only for the short steel and both CFFT arch tests. TPCs were also placed behind each footing to gather the horizontal footing thrust. Deflection was measured using a combination of string pots and LVDTs to measure horizontal and vertical movement at these same points along the arch as well as the top and bottom of the footings for the short arch to capture footing rotations.

2.4.1.6. Loading Cases

The arch bridges were subjected to three load cases similar to the conditions seen in the field, backfill, service live load, and ultimate load phases. The backfill phase consisted of applying soil lifts of equal height to alternating sides of the arch to replicate the typically asymmetric construction. For all arches the lift height was 200 mm and each lift was compacted using a vibratory plate compactor. The tall steel arch was retested with un-compacted soil due to the dry soil density being relatively high and was the only arch to be tested with un-compacted soil.

Service loads were applied to the arches equally using an HSS 8x6x $\frac{1}{2}$ box beam spanning the inner width of the soil box transverse to the arch span with the 152 mm (6 in) side of the HSS in contact with the soil. The applied load was based off a scaled version of the AASHTO HL-93 tandem which was simplified to a line load. The resulting scaled load was 48 kN but was doubled to 84 kN since the first set of live load testing did not produce substantial deformation of the arches. The load was applied to the inner 60% of the arch span, starting at the apex and alternating from the north and south sides in increments of 20% of the span. Service live loads were applied to the Apex, 60% North, 60% South, 40% North, 40% South, 20% North, 20% South, and a retest was done at the Apex. The live load locations are shown in Figure 2.1. Service loading was applied to alternating sides of the arch to limit the effect of side sway that would have occurred if the load had been moved incrementally from one side of the span to the other. Load was ramped from a preload of 2.2 kN to 84 kN over the course of 3 minutes, held for 3 minutes and ramped back down to the initial preload over 3 minutes. This cycle was repeated 3 times to allow for data collection of the locked in effects.

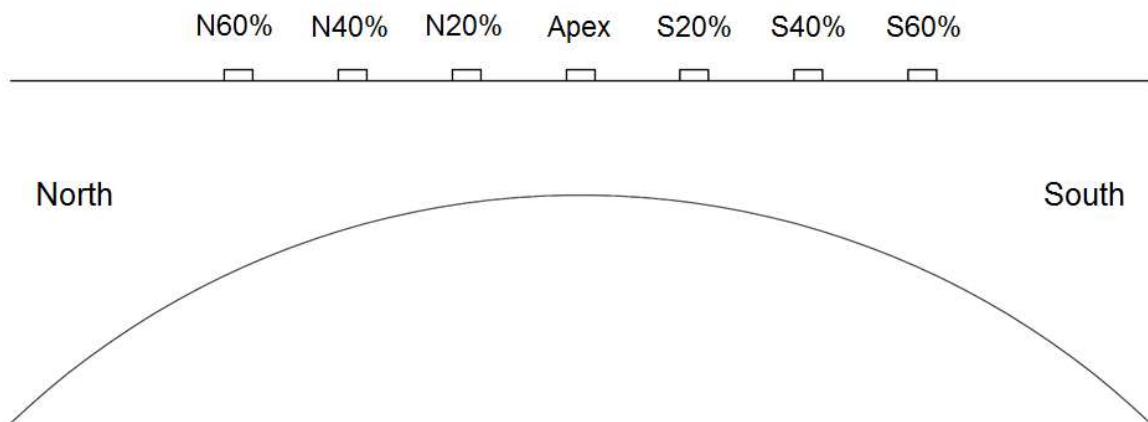


Figure 2.1 Live Load Application Positions

Ultimate load was defined as the irrecoverable loss in capacity of the arch.

Ultimate load was initially tested using the box beam at the apex for the tall steel arch.

During testing, the actuator caused a bearing failure in the cover soil and traveled through 70% of the apex soil cover before the test concluded. Subsequent ultimate load tests included a timber mat under the load beam to replicate pavement and spread the load.

2.4.2. Simulation

Two models were developed by Walton et al. (2015 b) to simulate the experiments conducted in the lab: a soil-continuum model and a soil-spring model. The soil-spring model developed by Walton herein is referred to as the ‘Existing Model’. The models focused on the SSI between the arch and the soil due the loading conditions. ABAQUS Explicit was used to develop the soil-continuum model. The soil-spring model was developed in MATLAB (2014).

2.4.2.1. Soil-Spring Model

The soil-spring model developed by Walton et al. (2015 b) was the basis for the continuing effort to improve the analysis of composite buried arch structures. Code was written in MATLAB (2014) to model a 2-D singular arch. Loading consisted of three main phases, similar to experimental loading cases. In order, the analysis solved the model for self-weight and backfilling, service live load, and ultimate load at the apex of the arch. The solver in the model was an iterative Newton’s solver that minimized the residual force until buckling (ultimate analysis), at which point a Riks-Wepner solver (Crisfield, 1991) was utilized. Initially, the model assumed small deformations, but upon further investigation, the effect of large axial arch forces through small deformations created additional moment that the small deformation solver did not include, called the P-

delta effect. Large deformations were implemented by Walton et al. (2015 b) and the new member forces were computed using updated nodal locations, which gave predictions that were much more consistent with experimental results.

2.4.2.1.1. Soil-Springs

The Existing Model represented the soil as horizontal soil-springs attached to each arch node based on the assumption that there was an infinite soil mass horizontally outward from the arch to push into. Pore pressure was assumed to be zero when calculating vertical stresses in the soil; therefore the effective stress was equal to the total stress. The spring force depended on the vertical stress in the soil, the coefficient of lateral earth pressure (K), and the tributary area of each soil-spring equal to the vertical projection of the arch element multiplied by the arch spacing. The springs were based on a Rankine model for use in retaining wall design. Rankine theory for retaining wall design assumes that the wall is frictionless and the soil is granular with no cohesion to calculate active and passive soil reaction forces.

Soil-springs depended on a nonlinear K -deformation relationship described in NCRHP (1991), which defined active and passive soil states depending on the wall movement relative to the soil. As the wall moves into the soil mass, the soil enters a passive soil state. Similarly, as the wall moves away from the soil, the soil enters an active soil state. The movement of the arch had a nonlinear relationship with the coefficient of lateral earth pressure. As the soil enters an active state the coefficient of lateral earth pressure decreases and results in a lower horizontal force. As the soil enters a passive soil state the coefficient of lateral earth pressure increases to give a higher horizontal force. Soil was assumed to be compacted to replicate the conditions of the

experiment, and the at-rest K was equal to 1, meaning that the vertical and horizontal stresses acting on the arch from the soil were identical. Each soil-spring was also independent of other soil-springs, allowing soil-springs adjacent to one another to be in completely different soil states. This was not completely realistic since friction in the soil between each node will shed stresses and affect the stress of nearby soil.

2.4.2.1.2. Arch Elements

Arch elements were defined as 2-D Euler-Bernoulli beam elements with a nonlinear moment-curvature relationship. Coupons were tested using stock from which the arches were made to get the stress-strain relationship, then the moment-curvature relationship to accurately model the response of the arch. Each arch typically had 80 arch elements throughout the span, which aligned the gauges used experimentally in the arch and in the soil to nodes of the arch to allow for better comparison.

Modeled CFFT arch structural members were also used in the analysis. A material model developed by Burgueño (2001) was used to calculate the nonlinear moment-curvature relationship of the CFFT members by applying a curvature to a section of the structural member and solving for equilibrium. The Burgueño model accounts for the different material properties of the FRP shell and the self-consolidating concrete fill. This research primarily focuses on the steel arch to limit the amount of nonlinearities present in the model.

2.4.2.1.3. Foundation

Initially, the arch was assumed to be fixed at the top of the foundation. It was found during backfilling and live loading that the foundations had undergone appreciable rotation and movement. The updated foundation elements were modeled as stiff beam

elements with soil-springs in the horizontal and vertical directions to capture the soil response due to foundation thrusts and rotations. Horizontal soil-springs acting on the foundation were identical to the horizontal springs acting on the arch. Vertical soil-springs acting on bottom of the foundation were stiffer to support the weight of the system.

2.4.2.1.4. Backfilling

Backfilling the arch bridge with soil was simulated in the model by installing 'lifts' representing soil weight and geometry to alternating sides of the arch then solving for equilibrium. As each lift was installed, newly covered soil-springs were activated and the nodal deformation was saved as the soil-spring's zero position. The spring's zero position was the deformation in the spring for it to be considered at-rest with a lateral earth coefficient of 1. Lifts were installed in equal heights on alternating sides of the arch until the grade was at the apex. Then each successive lift was applied over the whole arch system to the specified apex cover depth.

2.4.2.1.5. Live Load Application

Live load was applied as a strip load 152 mm wide to the surface of the backfilled soil. The load was applied to the same locations as in the experimental regime: Apex, 60% North, 60% South, 40% North, 40% South, 20% North, and 20% South. For each location the load was tested, arch member forces and deformations were reset to the end of backfill so that the previous live load did not have an effect on the current load step. The live load was applied incrementally to facilitate convergence.

Live load was distributed throughout the soil using a Boussinesq model for soil stress distribution due to a uniform rectangular load at the surface. For this 2-D analysis

the model assumed that the stress due to the live load was the same over the tributary spacing of the arch.

2.4.2.1.6. Ultimate Load

Ultimate load was applied using a strip load at the apex. The load was increased in small increments until the arch starts to undergo significant deformations that hinder convergence. At this point the solver switched from a Newton solver to a Riks-Wepner solver that has a better ability to solve relatively fast moving, large deformation systems. When the load applied was too high and a solution cannot be found, the load increment was halved and the solver tries again with the new load.

2.4.2.2. ABAQUS Continuum Model

The soil-spring model did an adequate job at quickly calculating the arch internal forces, but was unable to capture the true stresses in the soil. A soil-continuum model was developed by Walton et al. (2015 b) in ABAQUS Explicit. This model was much more computationally intensive than the soil-spring model and was used as a research tool only, with limited applications for widespread use. The soil-continuum model used a realistic material model for the soil. A tensionless soil-continuum was applied in lifts to the steel arch to get a look at the stress distribution inside the soil mass. Soil failure was included in the model as a Mohr-Coulomb Failure criterion. The soil was modeled as three-noded triangular elements to match the curvature of the arch. The arch was modeled as a two dimensional beam element with material properties taken from coupon level tests of the material in the arch. The foundation was modeled as a stiff continuum. The arch was linked to the foundation to enable moment transfer at the arch base. Soil was in contact with the arch and the foundation with a hard normal behavior and a penalty

tangential with a frictional coefficient of 0.6 (NAVFAC 1986). The soil-continuum model had two phases, backfilling and service live load. The backfilling phase was a complex series consisting of creating the new soil lift and installing it, solving for equilibrium, then creating a new assembly using the final solution from the previous lift and iterating until the end of backfilling. Service live load was applied using beam impactor elements at the surface of the backfilled soil.

2.4.3. Conclusions

The current soil stress distribution model may be inadequate for use during service and ultimate load analyses. The Boussinesq model assumes a continuous soil with uniform material properties not seen in a buried arch structure. Also, the actual soil stresses are redistributed due to the movement of the flexible arch due to intergranular frictional forces.

The two objectives of this research were to improve the soil-spring model and to create prototype software to allow these models to be used easily by other engineers. The experimental and simulation work, particularly the soil-spring model, that Walton et al. (2015 a,b) has conducted were the basis for the continued research presented here. There is work to be done to improve the soil-spring model. Walton et al. (2015 a,b,c) had recommended several aspects to investigate such as the live load distribution and soil-spring orientation that will ideally improve the model response and more accurately simulate these buried arch structures. The model was also highly specialized and inconvenient to be used as everyday analysis software. Results gathered from the experimental and simulation work from Walton et al. (2015 a,b,c) were compared to the

work presented in this thesis, and are denoted as “Experiment” and “Existing Model” when appropriate.

CHAPTER 3

DEVELOPMENT OF A USER-FRIENDLY ANALYSIS TOOL

3.1. Introduction

As detailed in the previous chapter, a viable method for analyzing soil-structure interaction for buried CFFT arches is a nonlinear soil-spring model. The software developed by Walton et al. (2015 b), defined as the Existing Model in Chapter 2 and described in more detail in Chapter 4, took this approach. However, the Existing Model was developed as a research tool, and thus incorporates a flexible sophisticated boundary condition simulation method needed to capture the response of a range of test specimens. Further, the Existing Model was not user-friendly, but relied entirely on text-based input and gives text-based output. The analysis software developed as part of this project was named *CBAS Design*. It is a tool that allows an engineer to analyze a composite buried arch structure using the underlying finite element analysis model developed by Walton et al. (2015 b), i.e. the Existing Model, with some simplifications. Users are able to select different materials, geometries, soils, and analysis parameters to define a range of linear elastic or nonlinear buried arch structures. Predefined composite FRP layups are available that are representative of FRP typically used in the field. Further, *CBAS Design* incorporates a highly interactive user interface for model generation and result interpretation.

3.2. Overview of *CBAS Design*

Analysis of the structure proceeds in one or two phases, depending on the user's objective. The first phase is the soil backfilling to a specified apex crown depth. Backfilling process allows for different soil types and compaction levels. Application of

an additional distributed load is the optional second phase. Application of loads is possible through discrete patches or as a surcharge.

The user is allowed to change parameters of the structural properties, load configuration, and analysis conditions. These three fields correspond to pages in the *CBAS Design* UI. The first page ‘Structure Properties’ is shown in Figure 3.1.

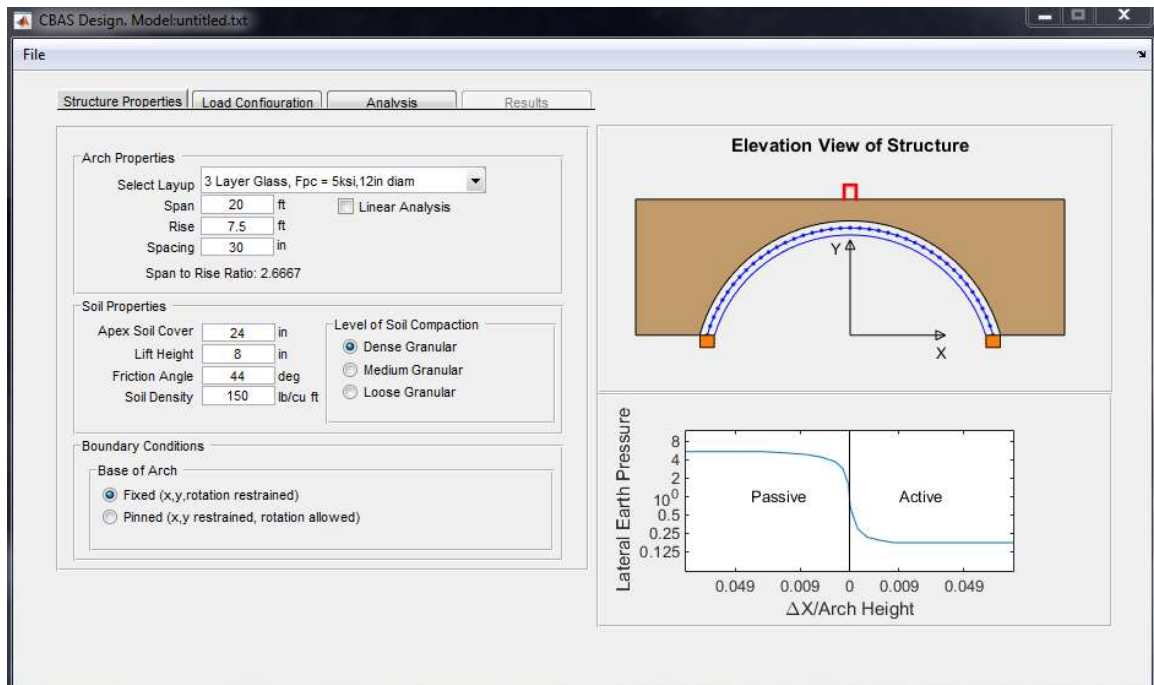


Figure 3.1 Screenshot of *CBAS Design* Structure Properties Page

The structural properties field allows the user to specify the type of material used for the arches, including linear elastic materials or concrete-filled FRP tubes with predefined layups, diameters, and concrete strengths that exhibit nonlinear moment-curvature response. Arch geometry is defined by span, rise, and spacing. Boundary conditions are applied at the base of the arch as either fixed or pinned on both ends. Soil parameters are also entered in this page. A range of crown depth and lift heights can be selected for an analysis. Characteristic soil properties such as friction angle and density

allow the user to define different types of soils for backfilling. Soil compaction level is predicted using NCHRP deflection-stiffness curves for soils with different friction angles. The level of soil compaction adjusts the NCHRP curve response to simulate the effect of different soil compactions. A denser soil would reach a fully active or passive soil under less deformation than a loosely compacted soil.

The software has the ability to analyze the structure using a small or large deformation solver. In a small deformation solver, the forces are not recalculated for the new nodal positions due to the assumption that the nodal displacements are small. In the arches under compression, there is a high axial component of the member force. The axial force and nodal displacement generates an additional moment on the member not captured by a small deformation solver, known as the P-delta effect. The large deformation solver tracks the nodal positions as the structure deforms and allows these increased moments and deflections to be taken into account.

After the completion of the soil lift phase up to eight patch loads of different size can be applied to the top of the backfilled soil simultaneously. These patches can be different sizes and occur at different locations on the span of the arch in the x and z directions. It is possible to analyze a structure under only backfilling loads if the user is only interested in a construction load case. In addition to this, it is possible to apply a uniform surcharge over the whole structure. This is applied in the same step as any patches. While a surcharge can be used to represent additional soil cover, all patches are still applied at the original top of backfill.

For more detailed information on the variables and their limits along with a guide on how to install and use *CBAS Design* refer to the *CBAS Design* User's Manual in Appendix A.

3.3. Assumptions in the Model

To increase efficiency of the software and decrease calculation time relative to the Existing Model, several assumptions were made. This solver used a finite element approach to modeling the arch using two types of elements. Two dimensional beam elements were used for the arch members, while horizontal axial spring elements represented the soil. Soil pressures were distributed over a tributary width equal to the arch spacing and were supported only by arch elements. All soils were assumed to have an at rest lateral earth pressure coefficient (K_o) of 1, consistent with that of compacted soils (Clough, 1990).

Soil was modeled as springs that contribute to the horizontal restraint in the system. Only granular soil material was modeled in the software and soil cohesion was not included. Applied loads were distributed through the soil using Boussinesq theory for stress distribution. Boussinesq theory assumes an elastic, homogeneous, infinite soil mass below the applied load. This was not the case when calculating the applied vertical stresses at the arch, however Boussinesq is a widely accepted approach to approximate the stresses on buried structures as previously discussed.

Test analyses were run on the software to gauge the *CBAS Design*'s reliability for each of the twelve predefined layouts. These test models had spans of 3, 7.6, 12.2, and 18.3 meters with span-to-rise ratios of 2, 3.5, 5, and 6 resulting in 192 different models. For each analysis the following were identical: the large deformation solver was used, the

arch was discretized with 40 elements, arch boundaries were fixed against displacement and rotation, there was a 610 mm apex soil depth and lift heights were 200 mm, the soil density was 2.4 Mg/m^3 , arch spacing was 762 mm, the soil friction angle was taken as 44 degrees, and the first soil compaction curve corresponding to dense granular material was used. The analysis was able to run for most cases, and was able to alert the user in the three situations where a converged solution could not be found in either the backfill sequence or the application of the patch load. Analyses where the solver failed to find a solution were all situations with a span of 18.3m and a span-to-rise ratio of 3.5. *CBAS Design* predicted a sideway failure for these load cases. In the event that the software was unable to find a solution, the user was notified and given tips to facilitate convergence on subsequent analyses.

3.4. Verification of Soil-Spring Design Software

Results for both steel arches tested experimentally by Walton et al. (2015 a) were compared against predictions from nearly identical models created with *CBAS Design* and the Existing Model. Models in *CBAS Design* and in the Existing Model only differed by the boundary conditions applied to the base of the arch as well as *CBAS Design*'s neglect of the decking over the arches. *CBAS Design* assumes a fixed boundary, restraining all translation and rotation, while the Existing Model defined the arch footing as a stiff linear elastic footing supported by soil-springs in both the horizontal and vertical directions. This allowed the Existing Model to capture footing rotation that more closely resembled the experiment. Both models were discretized using 80 arch elements with identical properties for both the steel arch and the soil. Lifts were set at 200 mm for both models and an apex crown depth of 610 mm. The Existing Model and *CBAS Design*

included identical simulated line loads to the apex of the structure: a patch 152 mm wide and 21.3 m long with a total force of 834 kN. The longer patch in the model more closely represented a strip load than the load applied during the experiment. Moment and displacement effects for both the tall and short bridges due to backfilling and apex load were investigated in the following sections. Apex load effects were the total effect of apex service load and backfilling minus the effect of backfilling. The shoulder of an arch was defined as the location where the peak moment offset from the apex occurred and the location was roughly halfway between the arch apex and foundation.

3.4.1. Tall Arch Comparison

The tall arch had a span of 6.1 m and a rise of 2.3 m and 610 mm of soil cover over the apex. Moments and vertical displacements of the arch predicted by both models were compared to the experimental results and can be seen in Figure 3.2 through Figure 3.5. Model results were presented continuously along the span while experimentally gathered values appear at discrete points to represent the gauge's location along the span.

3.4.1.1. Backfilling

Backfilling moments were taken at the end of backfilling for each model. Both models gave similar results throughout the arch length. For the tall arch, *CBAS Design* predicted a 4% higher shoulder moment compared to the Existing Model and a 17% higher shoulder moment than experimental results, seen in Figure 3.2. Moments at the apex due to backfilling from both models were enveloped by the moments measured experimentally by the three tall steel arches with compacted soil and with loose soil, and both the Existing Model and *CBAS Design* predicted the same apex moment within 1%.

Tall arch model moments at the footing were within 2% of the experimental value on the left side but the models over-predicted the footing moment on the right side. *CBAS Design* predicted a footing moment 35% higher than the experiment, while the Existing Model predicted a footing moment 45% higher than experimental. Both models over-predicted the maximum vertical deflection at the apex compared to experimental results (Figure 3.3). Experimental results could indicate that the deflection followed the same trend as the models but was shifted by about -5 mm.

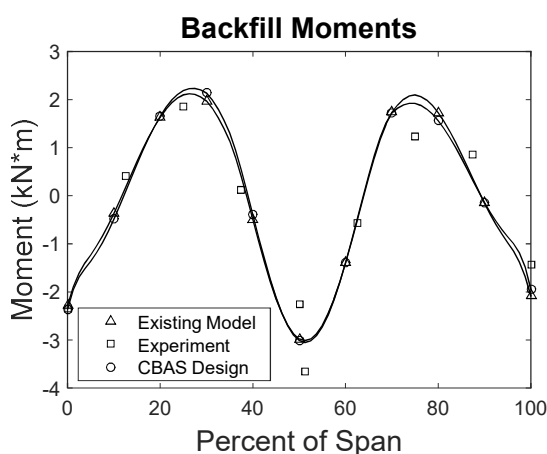


Figure 3.2 Tall Arch Backfill Moments

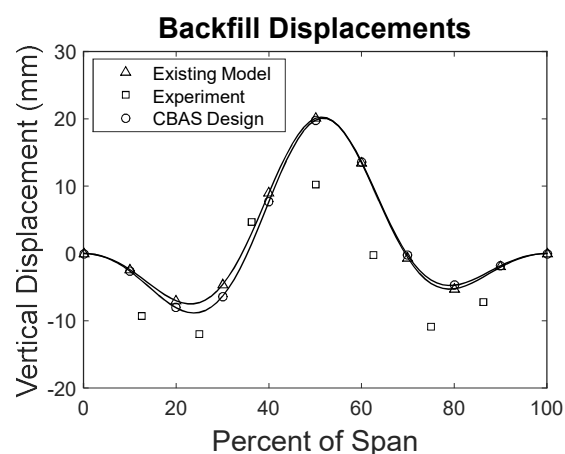


Figure 3.3 Tall Arch Backfill Displacements

3.4.1.2. Apex Service Load

The moments and displacements comparisons between the Existing Model, *CBAS Design*, and experiment due to an apex service load are illustrated in Figure 3.4 and Figure 3.5. Predictions of apex moment due to a line load for both models of the tall arch were within 2% of experimental moments. The maximum negative moment at the shoulder was over-predicted by 2% for the *CBAS Design* and 7% for the Existing Model. Footing moments were over-predicted by both models. *CBAS Design* uses an absolute

boundary condition, restricting all rotation and resulting in a 300% higher footing moment. The Existing Model allowed some footing rotation, but still predicted a footing moment 200% higher than experimentally observed. Vertical deflections, seen in Figure 3.5, due to the line load were also over-predicted almost everywhere along the arch span by both models.

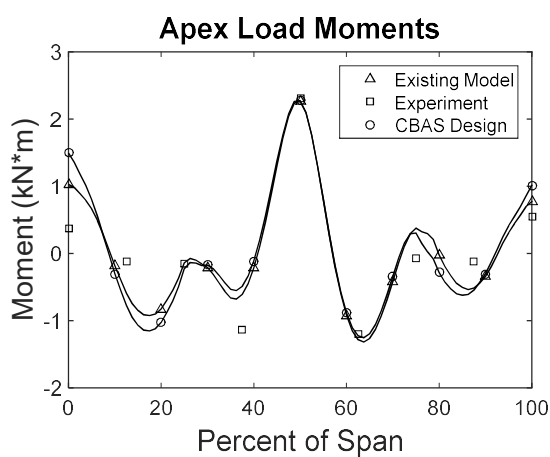


Figure 3.4 Tall Arch Apex Load Moments

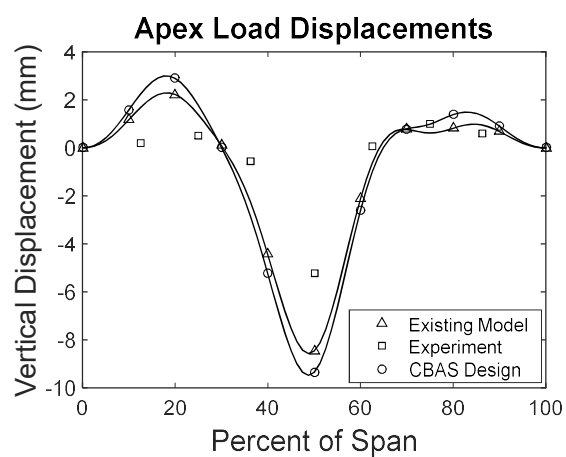


Figure 3.5 Tall Arch Apex Load Displacements

3.4.2. Short Arch Comparison

The short steel structure had a span of 6.1 m, a rise of 1.2 m, and 610 mm of soil cover over the apex. Moments and vertical deflections predicted by the Existing Model and *CBAS Design* were compared to results from the experiment. *CBAS Design* and the Existing Model did a better job at predicting the backfilling moments and vertical displacements for the short arch than for the tall arch model.

3.4.2.1. Backfilling

Backfill moments for the short arch are shown in Figure 3.6. Apex moments were under-predicted by about 10% by both models. At 75% of the span, the Existing Model

predicted the moment 2% above experimental and *CBAS Design* predicted a moment 1% above experimental. Moments were under-predicted compared to the experiment at 12% and 87% of the span, the most extreme being the side loaded first (87%), with moments measured 50-55% higher than the models predicted. Footing moments were over-predicted due to the restraint assumed by the models, predicting high moments not seen in the experimental results. However, the over-prediction by *CBAS Design* was greater due to its inability to account for rotation of the arch at the footing. Vertical displacements in Figure 3.7 were predicted by the *CBAS Design* to be 44% higher than experimental and predicted by the Existing Model to be 27% higher.

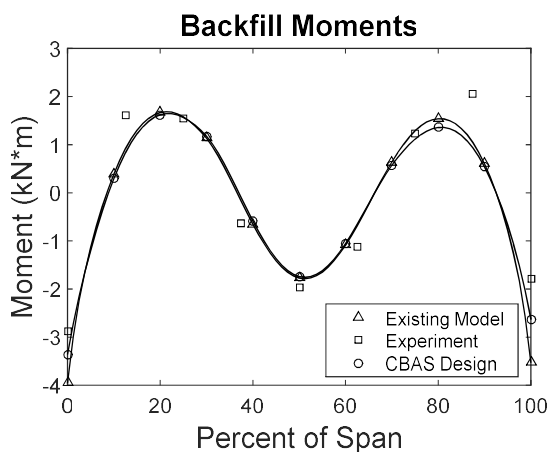


Figure 3.6 Short Arch Backfill Moments

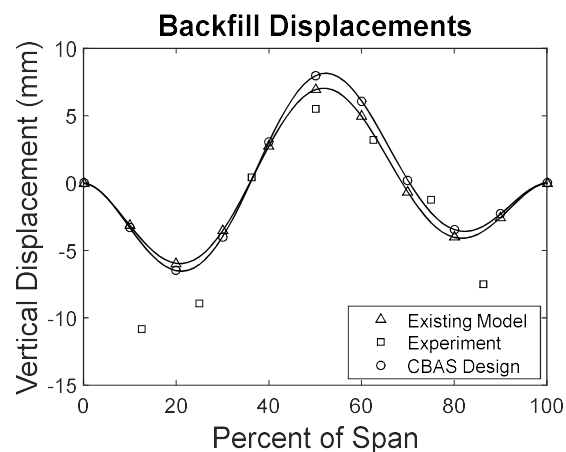


Figure 3.7 Short Arch Backfill Displacements

3.4.2.2. Apex Service Load

Apex service load moments were captured within 5% at the apex for both the Existing Model and *CBAS Design* shown in Figure 3.8. Shoulder moments due to the apex service load were over-predicted and shifted away from the center of the arch by both models. Vertical deflections can be seen in Figure 3.9. Apex vertical deflections

were under-predicted by both models. *CBAS Design* predicted a deflection 10% less than experimental and the Existing Model predicted a deflection 20% less than experimental seen in Figure 3.9.

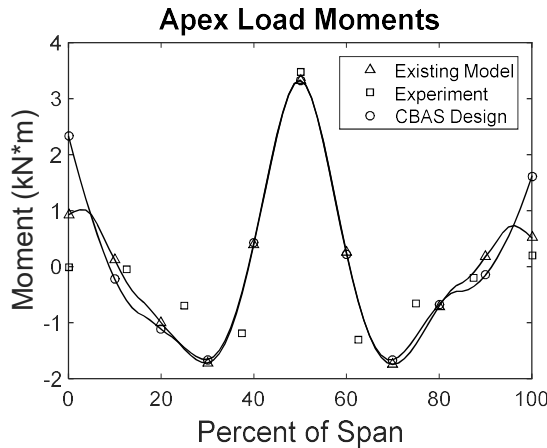


Figure 3.8 Short Arch Apex Load Moments

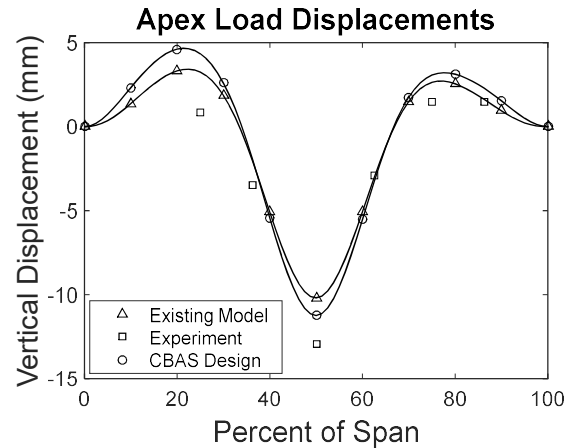


Figure 3.9 Short Arch Apex Load Displacements

3.4.3. Simulation Test Structure

To consistently verify *CBAS Design* in the following studies, a simulation test structure was designed as a buried arch structure representative of bridges in the field today. The following parameters were used for all studies except the parameter under investigation: the test structure was a 12.2 m span and 3m rise arch, giving a span-to-rise ratio of approximately 4 (typical for buried arch FRP construction); the FRP layup used had 3 glass layers in the longitudinal direction with a 304 mm diameter tube; and the concrete compressive strength was taken as 34.5 MPa. Lifts were applied in 200 mm increments to a crown depth of 610 mm. Soil parameters were taken from the previously described experiments: a dense granular material with a friction angle of 44 degrees and a density of 2.4 Mg/m³. A screenshot of the structure when entered into *CBAS Design* can

be seen in Figure 3.10. Arch internal moments were compared between different models in each study since it is typically the controlling factor in design. Concrete filled FRP tubes are efficient in axial compression and shears are relatively small.

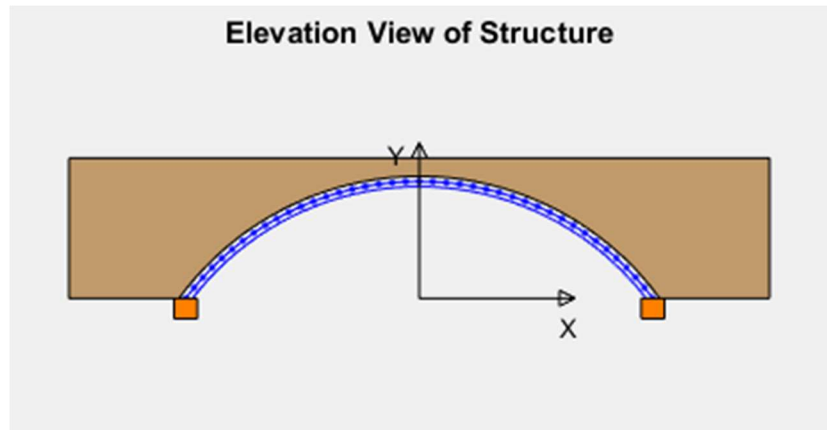


Figure 3.10 Test Structure entered into *CBAS Design*

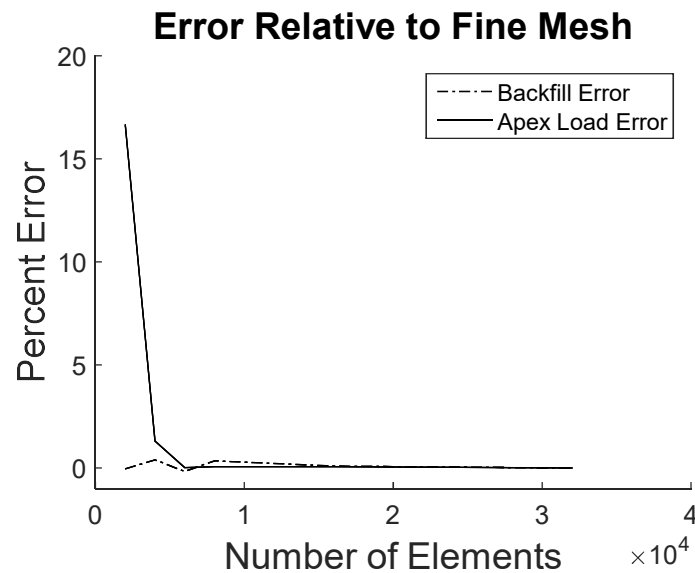
3.4.4. Mesh Convergence Study

To study mesh refinement, the same model was run using *CBAS Design* with an increasing number of elements. Each large deformation model used the same structural parameters and loading. Models were created for 20, 40, 60, 80, 160, and 320 arch elements. Apex moments were compared between each model to study convergence in

Table 3.1 and a visualization of the error in Figure 3.11. The table below shows the predicted apex moments due to backfill and apex patch loading and the error relative to the 320 element model. For both load conditions, the 60 element model predicted moments within 0.5% of the 320 element model. When 40 elements were used the error increases slightly, resulted in an error within 1.5% when compared to the 320 element model. The default value used in *CBAS Design* was 40 elements to balance accuracy and runtime.

Table 3.1 Mesh Convergence

	Number of Elements					
	20	40	60	80	160	320
Backfill Moment (kN·m)	-13.898	-13.959	-13.880	-13.953	-13.917	-13.904
Backfill Error (%)	-0.041	0.400	-0.165	0.354	0.094	0
Patch Moment (kN·m)	14.626	12.701	12.539	12.544	12.544	12.536
Patch Error (%)	16.671	1.316	0.026	0.066	0.066	0

**Figure 3.11 Error for varying number of elements, Mesh Convergence**

3.4.5. Small vs. Large Deformation

The large deformation solver can take into account the P-delta effect produced by the high axial loads acting through the element displacements. Moments were studied using the test structure described above to analyze the difference between small deformation and the large deformation solver. The moments predicted by these analyses are shown in Figure 3.12 and Figure 3.13. A 7% difference in predicted moment occurred

at the apex during backfilling and a 5% difference at the shoulders with the large deformation solver predicting a higher moment. During an applied patch load, peak apex moment from the large deformation solver was higher than the small deformation solver by 6% and shoulder moment was higher by 14%. A large deformation solver is recommended, since it accounts for additional moment caused by the axial forces through the deformation of the arch elements.

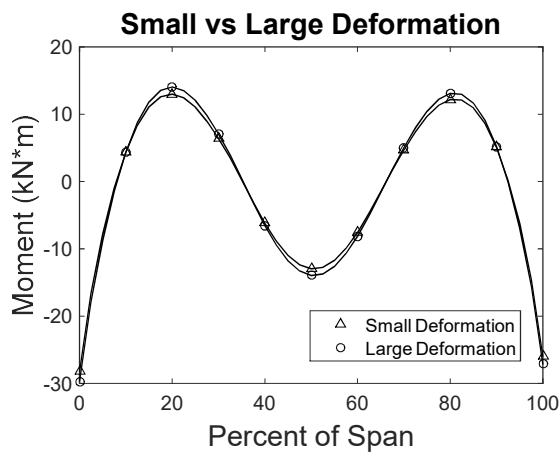


Figure 3.12 Small vs Large Deformation Backfill Moments

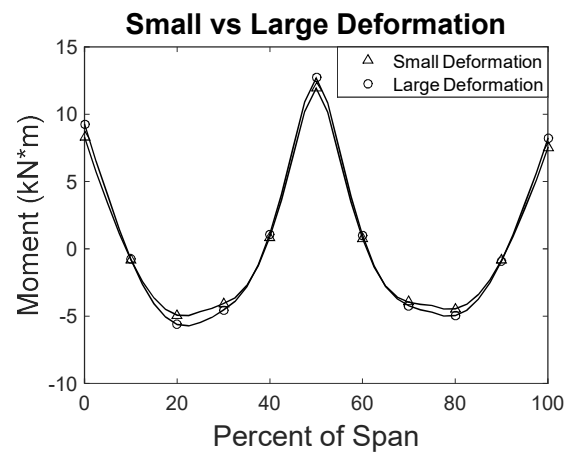


Figure 3.13 Small vs Large Deformation Apex Load Moments

3.4.6. Sensitivity to Soil Parameters

Different soil parameters were applied to the test structure in three different models, to study the effect of soil type on the moment. The first model contained soil with a friction angle of 44 degrees and a dense soil compaction level, the second model contained soil with a friction angle of 37 degrees and a medium soil compaction level while the third contained soil with a friction angle of 30 degrees and a loose soil compaction level. For each soil type, a soil density of 2.4 Mg/m^3 was used. Though

unrealistic, this ensured consistency between the three models. Moments predicted by each of the three models can be seen in Figure 3.14 and Figure 3.15.

Apex backfill moments due to the loose soil were 4% higher than medium soil and 14% higher than dense soil. Shoulder moments showed a higher sensitivity to soil type. Loose soil resulted in moments at the shoulder that were 20% higher than medium soil and 37% higher than dense soil. The increase in moment can be explained by the decrease in lateral restraint caused by the looser soils. This extra movement allowed the arch to deflect more than during the dense and medium case, causing an increase in the moment within the arch elements.

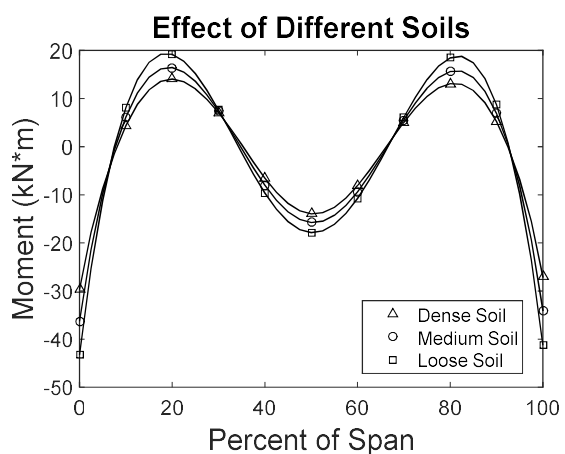


Figure 3.14 Effect of Different Soil Compaction, Backfill Moments

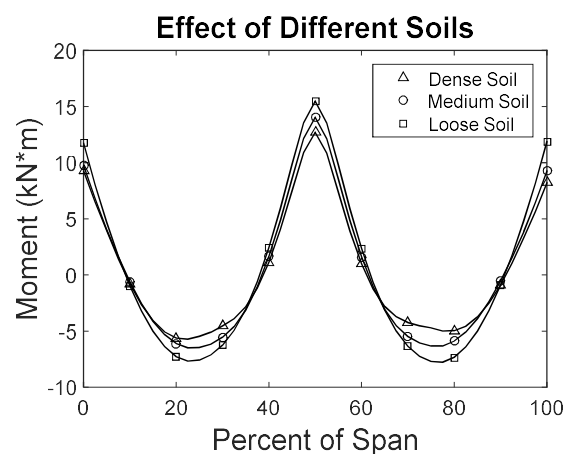


Figure 3.15 Effect of Different Soil Compaction, Apex Load Moments

The results indicate the response expected of soils with different compaction levels. A looser soil allows the arch to deflect into and away from the soil before higher soil reactions are achieved, this allows for more curvature within the beam element and therefore a higher internal moment.

3.4.7. Effect of Different Lift Heights

The test structure was analyzed using alternating lifts of 51 mm, 203 mm, and 610 mm and a model with lifts applied evenly to both sides in 51 mm lifts to find the effect of different lift heights on the final moments from backfilling. Moments predicted for the final step in backfilling are shown in Figure 3.16. A notable difference was that for a larger lift height, the moment at the end of backfilling became more asymmetric, and shoulder moments increased by almost 10% in both cases when compared to the symmetrically loaded 51 mm lift model. The alternating 51 mm lift model predicted a more symmetric response due to a more even loading. Lateral earth pressure coefficients for each of the models in Figure 3.17 show the increasingly asymmetric response for the taller lift heights. At about 30% offset from the apex, lateral earth pressures became uniform for all lift heights regardless of whether the lifts were alternating or symmetric.

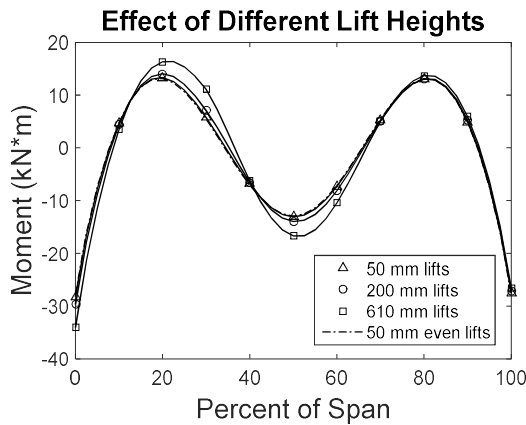


Figure 3.16 Effect of Different Lift Heights, Backfill Moments

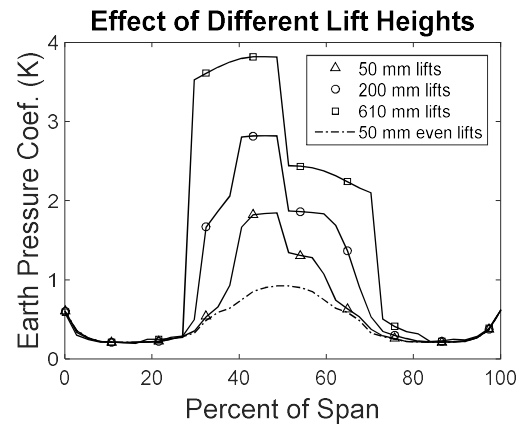


Figure 3.17 Effect of Different Lift Heights, Horizontal Earth Pressure Coefficient

3.5. Summary and Conclusions

As part of the continuing effort to make concrete filled composite buried arch technology more efficient and easier to design, prototype software was developed for the analysis of buried arch structures using a simplified version of the soil-spring research model developed by Walton et al. (2015 b). The software, called *CBAS Design*, is a 2-D finite element analysis solver that simulates the backfill sequence and the application of any additional loads at the top of backfill. Verification of the software was done by comparison with the experimental results of Walton et al. (2015 a) and previously developed models (Walton et al. 2015 b) to ensure the accuracy of the features provided in *CBAS Design*. Load distribution through the soil and mesh refinement has been considered, including the effects of large and small deformations. Parametric studies have examined the sensitivity of the model to changes in soil parameters and different lift heights. Appendix A contains the *CBAS Design* user manual and documentation.

CHAPTER 4

PROPOSED IMPROVEMENTS TO THE EXISTING MODEL

4.1. Introduction

This chapter describes the Existing Model to identify aspects that could be improved. Two components of the model, the live load distribution and the soil-spring orientation, were discussed. The live load distribution due to an applied load at different locations along the span was compared with the experimental pressures and a finite element model to identify weak points. Three soil-spring orientations were examined based on the improvements that each offers over the original Existing Model detailed in Chapter 2.

4.2. Assessment of Load Distribution Model

The Existing Model used a Boussinesq stress distribution (Holtz et al. 2011) to calculate the effects of loads acting on the soil surface. The Boussinesq model assumes that the soil is an infinite, isotropic, linear elastic material. These simplifications limit the accuracy of the Boussinesq model, but the method is reasonable and widely used to calculate the vertical stresses on buried structures. This section focuses on assessing the load distribution model by comparing it to experimental data and finite element model results.

Two 2-D finite element models for this analysis were created in ABAQUS (2011) to capture the stresses in the soil due to gravitational and service loading. The first model simulated the conditions of the Boussinesq stress distribution. Stresses in the soil due to applied load were calculated using influence factors that depend on the shape of the applied load and the relative location of the point of interest. This model simulated the

Boussinesq stress distribution by using the assumptions of Boussinesq theory that the soil is idealized as a linearly elastic, homogeneous continuum. Boussinesq theory assumes a semi-infinite half-space while the FE model is bounded, however, given the size of the modeled FE domain the effect of the boundaries was expected to be minimal. This model represented a soil mass the size of the soil box built for the experimental testing by Walton et al. (2015 a) using three-noded plane-strain elements with large deformations considered and unit plane strain thickness. Vertical stresses predicted by the model were virtually identical to stress calculated using Boussinesq influence factors, as expected.

The second model simulated soil-structure interaction using a simplification of the arch-soil system to capture the effect of a flexible arch in the soil. The soil was defined using three-noded plane-strain elements with large deformations considered and unit plane strain thickness. The rectangular steel arch sections were modeled using the same height, while the widths were divided by the spacing of the arch to keep the sections consistent with the unit soil thickness. Both the tall and short arches were modeled to get a notion of the vertical stresses calculated in each case. Both models used 25.4 mm three-noded triangular elements (classified as CPE3 elements) to represent the soil and, where applicable, 640 beam elements (classified as B21 elements) to represent the steel arch. The mesh for both models for the tall arch is illustrated in Figure 4.1 and Figure 4.2.

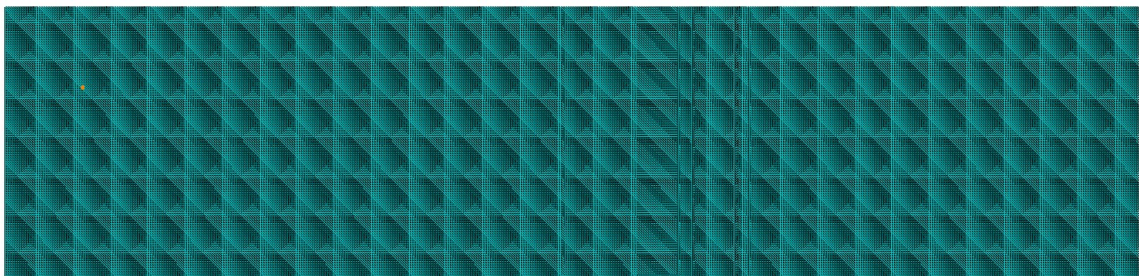


Figure 4.1 Simulated Boussinesq Model Mesh

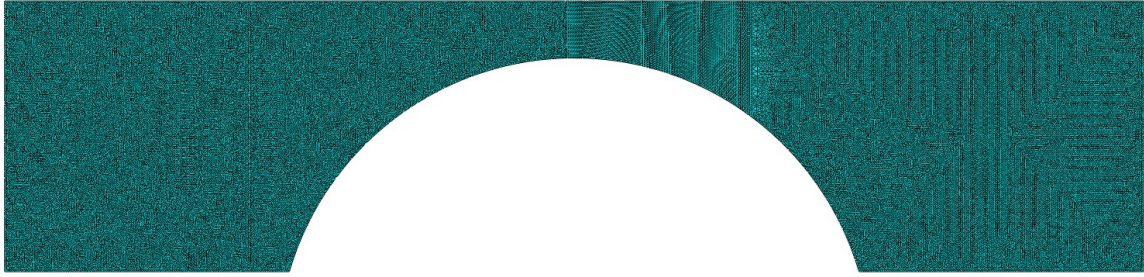


Figure 4.2 Soil Structure Interaction Mesh

4.2.1. Description of the Finite Element Models

For all models, the soil was modeled as linear elastic with an elastic modulus of 27.6 MPa, a Poisson's ratio of 0.3, and a density of 2.2 Mg/m³. An elastic modulus of 27.6 MPa was consistent with Petersen et al. (2010) for a granular soil at a depth of 0.3 to 1.5 m. Two models were created to calculate the vertical stresses due to a surficial load to a simulated infinite soil mass. Tall and short soil masses had a height equal to the height of backfilling above the arch-foundation interface, 2.9 m for the tall system and 1.8 m for the short system.

The SSI model included the contact effect of the linear elastic soil on the steel arch. Contact was defined as 'hard' contact in the direction normal to the soil surface and a frictional coefficient of 0.6 (NAVFAC 1986) was used in the direction tangent to the soil surface. In these models, the only parts in the assembly were the soil and the steel arch; foundations and ties were neglected. The steel was modeled as linear elastic with an elastic modulus of 200 MPa and a Poisson's ratio of 0.3. The beam sections were consistent with the experimental program for each arch. Fixed boundary conditions apply to the base of the arch to simulate a fixed restraint at the arch-foundation interface.

Though the Boussinesq distribution method was used to describe effect of surficial loads in soil only, the simulated Boussinesq model in this study includes the

effect of gravity for the backfill load case only. To get a more accurate measure of the soil structure interaction, gravity was applied to initially deform the steel arch before the service loads were applied. The effect of gravity was then subtracted from the total vertical stresses to determine vertical stress due to the live load. This was done for the SSI model and repeated for the simulated Boussinesq model for consistency.

The models were linear elastic and were not intended to exactly replicate the conditions present during the experiment. Backfilling the structure in asymmetric lifts introduced nonlinear aspects to the system and locked in arch displacements for subsequent lifts and loads. A more accurate model to determine load effects throughout the soil would include nonlinear materials for the soil, a lift sequence, and foundation elements with the same boundary conditions present in the model similar to the soil-continuum model developed by Walton et al. (2015 b).

4.2.2. Model Comparisons to Experimental Results

Vertical stress in the soil was compared between a simulated Boussinesq and SSI model as well as the experimental pressure data. The vertical stress distribution for the Boussinesq and the SSI model can be seen in Figure 4.3 and Figure 4.4. These figures show the combined effect of gravity of the soil mass and the applied service load.

Vertical stresses were taken from the approximate location of the pressure cells in the soil (Walton et al. 2015 a) near the arch to ensure an accurate comparison.

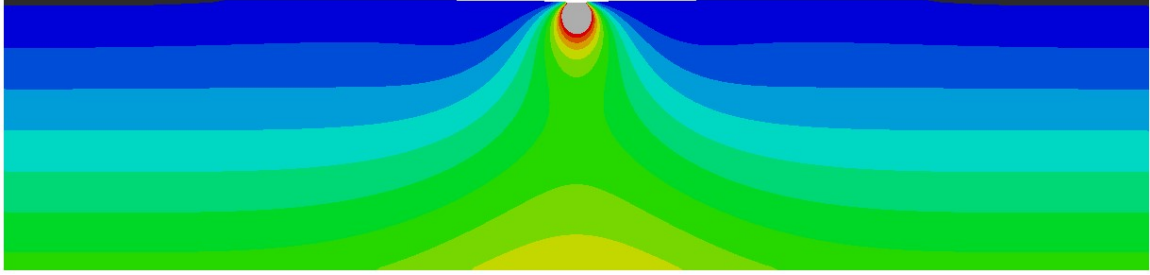


Figure 4.3 Simulated Boussinesq Soil Stress Due to an Apex Load

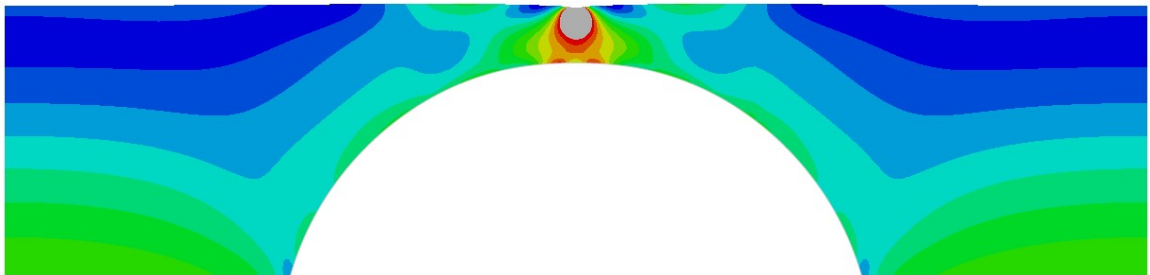


Figure 4.4 SSI Soil Stress Due to an Apex Load

Vertical soil stresses for the short and tall arches were compared in the following sections for the end of backfill, apex service load, 20% south offset load, 40% south offset load, and 60% south offset load.

4.2.2.1. Backfill Results

Backfill pressures for the short arch can be seen in Figure 4.5. Apex pressure was under-predicted when calculated using the Boussinesq model by 2.2% and over-predicted by the SSI model by 14%. Both models calculated approximately double the pressure immediately to the side of the apex. Footing pressure was over-predicted by both models, at 0% of the arch span, the models calculated similar values of 139% and 142% above the measured value.

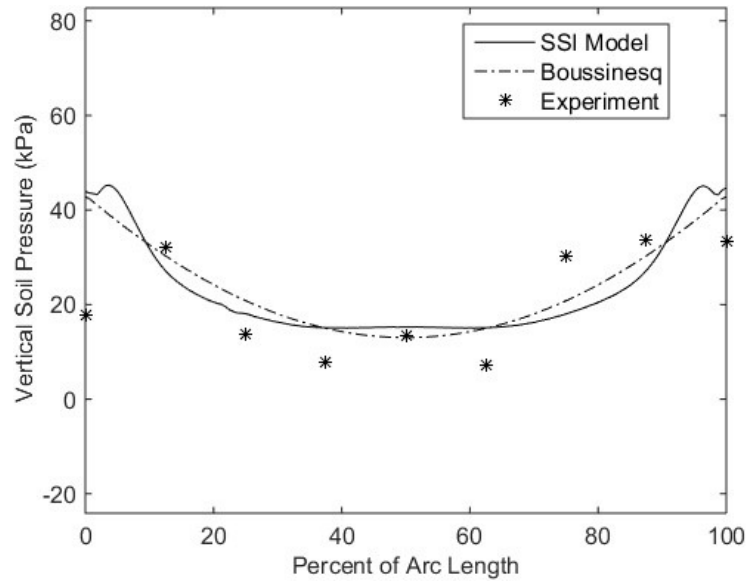


Figure 4.5 Short Arch Backfill Vertical Pressure

Vertical soil pressures for the tall arch were measured only for half of the arch seen in Figure 4.6. The vertical pressures in the tall arch were poorly represented by both models, under-predicted at the quarter point and over-predicted at the apex. The apex pressure was the opposite in magnitude of the calculated pressure from both models.

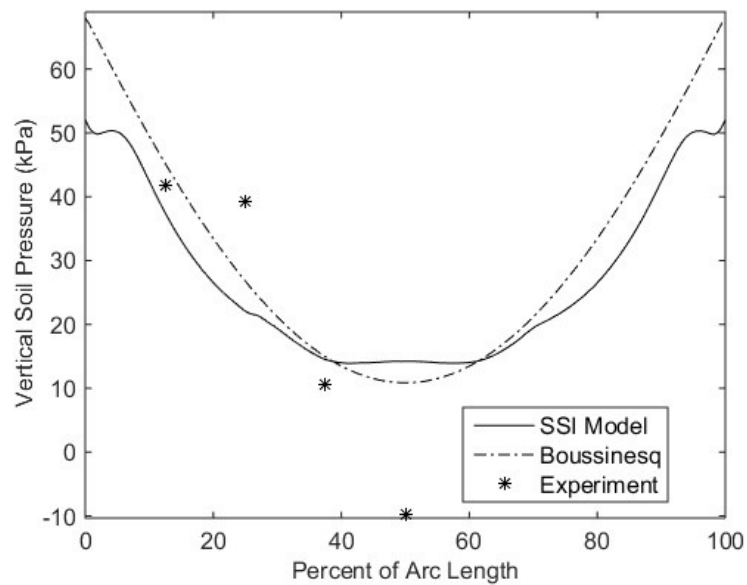


Figure 4.6 Tall Arch Backfill Vertical Pressure

4.2.2.2. Apex Service Load Results

Vertical pressures in the soil due to an apex load for the short arch can be seen in Figure 4.7. The apex pressure was under-predicted by approximately 50% using the Boussinesq model and 37% using the SSI model. The pressures immediately to the side match the values predicted by the Boussinesq model but the pressures at and below the shoulders of the arch were higher than the Boussinesq model. The offset pressures were closer to what was predicted in the SSI model.

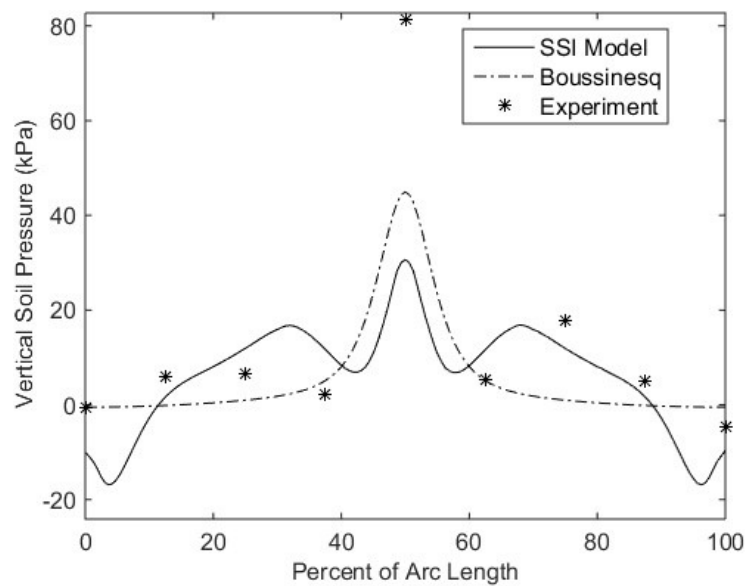


Figure 4.7 Short Arch Apex Service Load Vertical Pressure

Figure 4.8 shows the vertical pressures for the tall arch. The data showed a trend that looks similar to the Boussinesq distribution, but the pressure measured just offset from the apex was roughly triple the Boussinesq value. The jumps in pressure immediately offset from the apex seen in the SSI model were not seen in the experimental data due to the high spacing of the pressure sensors and the absence of pressure cells in the vertical direction on half of the arch.

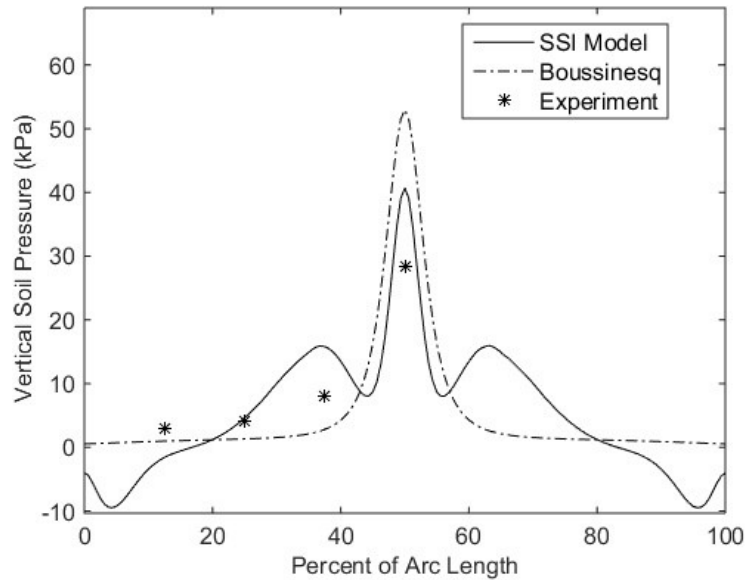


Figure 4.8 Tall Arch Apex Service Load Vertical Pressure

4.2.2.3. Offset Service Load Results

Vertical pressures in the soil for the short arch during the offset service load cases can be seen in Figure 4.9 through Figure 4.11. In the 20% offset load case the experimental data suggested a distribution of stresses similar to the SSI model. The magnitude of the maximum pressure seen experimentally was closely predicted by the SSI model but was offset, whereas the Boussinesq model calculated the pressure at the location of the pressure cell within 3%. The measured vertical stress at the footing on the side of the load falls between the Boussinesq pressure and the SSI model. On the opposite footing the vertical stress seen experimentally was under-predicted by both models, however the Boussinesq model predicted a negligible pressure while the SSI model predicted a pressure 63% of the measured value.

At 40% offset loading the experimental data followed a trend shown in the SSI model. The shoulder pressures measured were within 2% of the SSI model but were over-predicted by the Boussinesq model by 30%. The maximum pressure calculated from the

Boussinesq model was not seen in the experimental data or the SSI model. This could be attributed to soil arching. The footing moment measured in this case was better predicted by the SSI model, though it was still under-predicted by 20%.

The 60% offset loading case showed a trend closer to the Boussinesq model rather than the SSI model. The SSI model sheds the stress away from the point of the load and towards the base of the arch. The maximum measured pressure was under-predicted by both models. The SSI and Boussinesq model predicted a pressure magnitude 33% and 72% respectively, of the measured value at the point of the load. The footing pressure on the opposite side of the load was better represented by the SSI model with a predicted pressure 88% of the measured value.

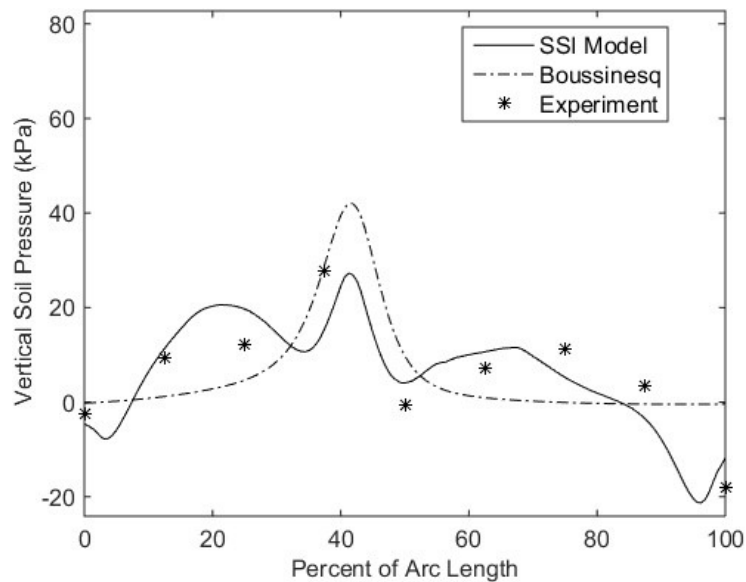


Figure 4.9 Short Arch 20% Offset Service Load Vertical Pressure

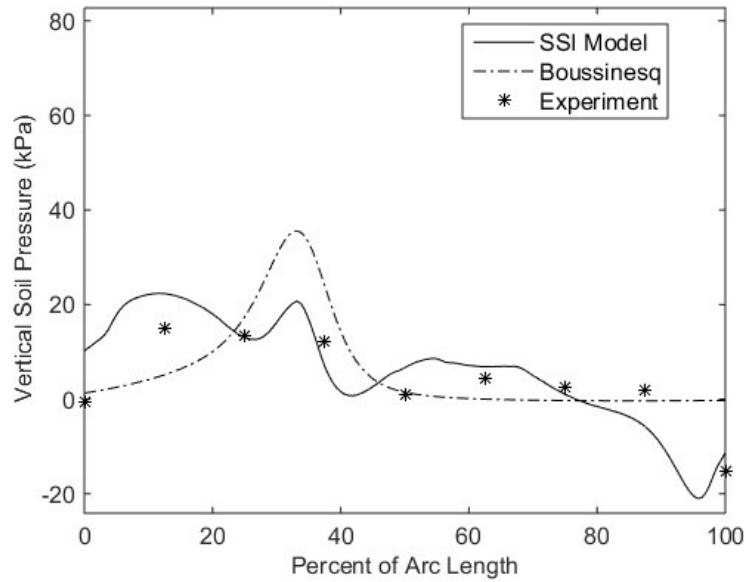


Figure 4.10 Short Arch 40% Offset Service Load Vertical Pressure

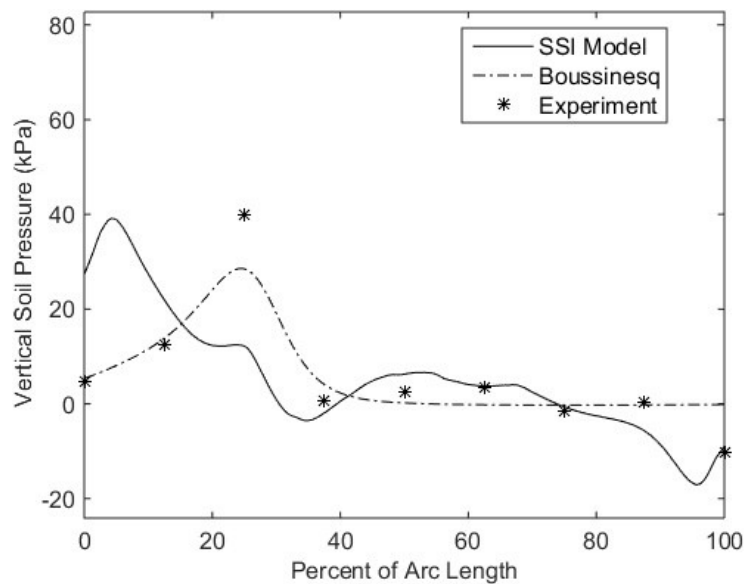


Figure 4.11 Short Arch 60% Offset Service Load Vertical Pressure

Vertical soil stresses for the tall arch due to offset loads can be seen in Figure 4.12 through Figure 4.14. In the 20% offset case the peak pressure seen in both models was not seen in the experimental data. The measured values for the apex and immediately next to the apex were over-predicted by both models, while the other locations were

under-predicted. The shoulder gauges suggest that the real stress distribution was similar to the one seen in the SSI model.

In the 40% offset load case, the stress at the point of the load was predicted within 4% in the SSI model and over-predicted by the Boussinesq model by 35%. As in the 20% load case, the stress due to the load could have been shifted toward the foundation, consistent with the SSI model.

Experimentally measured pressure values during the 60% offset load case followed the SSI model more closely than the Boussinesq mode. The apex and off-apex pressures were low, but the shoulder pressures were substantial. The quarter span pressure was under-predicted by both models, where the SSI and Boussinesq models calculated a pressure 62% and 81% of the measured values respectively.

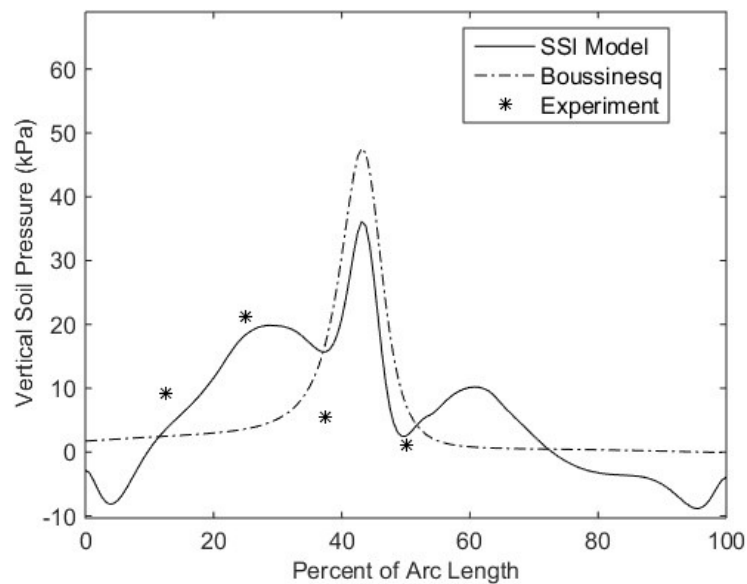


Figure 4.12 Tall Arch 20% Offset Service Load Vertical Pressure

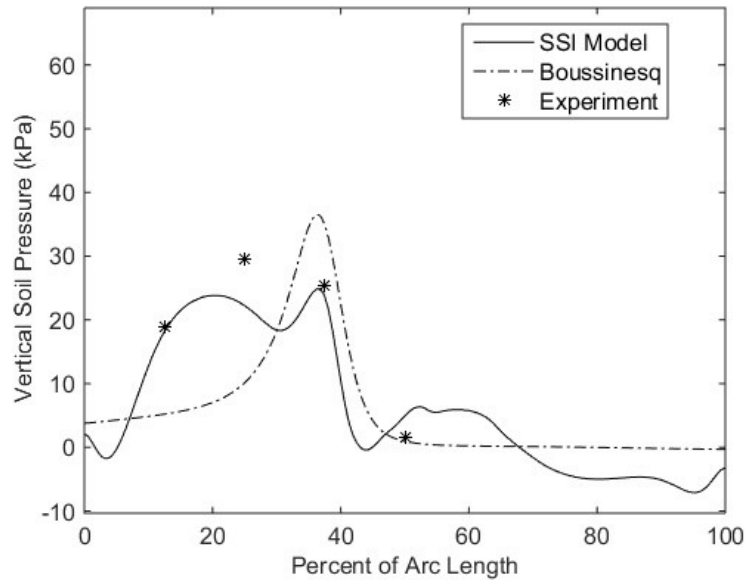


Figure 4.13 Tall Arch 40% Offset Service Load Vertical Pressure

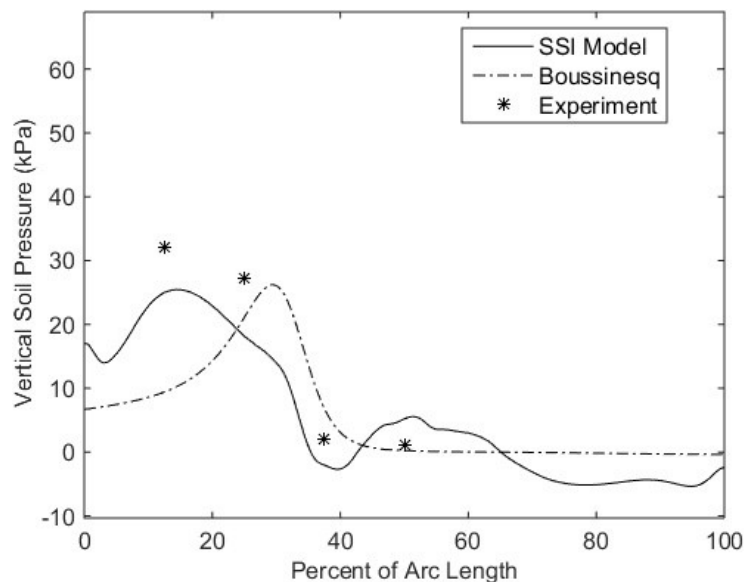


Figure 4.14 Tall Arch 60% Offset Service Load Vertical Pressure

4.2.3. Load Distribution Conclusions

The Boussinesq method is an accepted stress distribution model used by engineers to determine the vertical stresses at different depths in soil. In general, the experimentally gathered pressures tend to follow the trend shown in the SSI model more closely than the Boussinesq model. To improve the SSI model, a more realistic soil material could be

used as well as the addition of a backfilling lift sequence. It may be worth investigating other soil distribution models for implementation in the soil-spring model to get a more accurate response. If a similar experiment were to be conducted, more pressure cells should be used to capture the vertical stresses due to the load throughout the span of the arch.

4.3. Existing Soil-Spring Model

The Existing Model simulated the soil reaction force using horizontal soil-springs. Arch elements were modeled as beam elements with a bending stiffness calculated using the method detailed by Burgueño (2001). The elastic soil-springs used a nonlinear load deflection relationship, detailed in NCHRP Report 343 (Barker et al. 1991), to calculate the force exerted by each spring. The Existing Model can be seen in Figure 4.15, where a coarse mesh is shown for clarity.

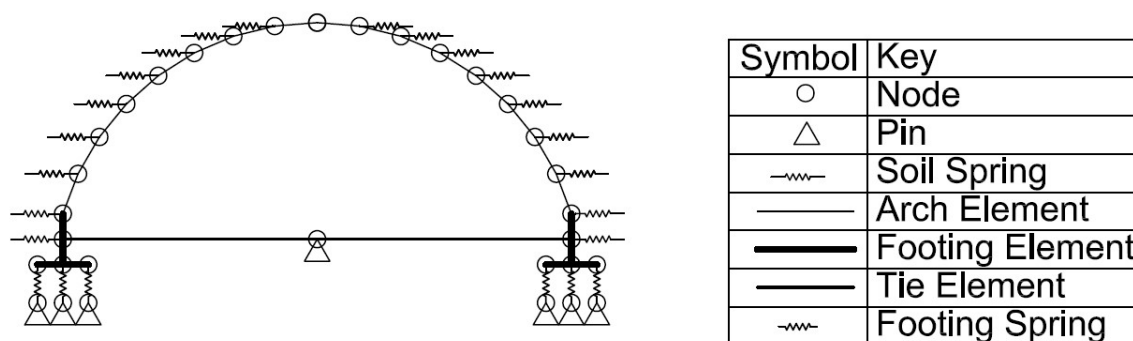


Figure 4.15 Existing Model (Walton 2015 c)

The Existing Model used Rankine theory for retaining wall design, assuming a frictionless contact between the soil and a vertical wall to calculate a horizontal reaction from the soil. For each analysis step, the model calculated the soil-spring force and stiffness by first taking the deflection (Δ_{spring}) of the horizontal soil-spring attached to the arch node and calculating an effective lateral earth pressure coefficient (K_{soil}) based on

the NCHRP load deflection relationship. Soil friction angle affects the load deflection relationship and was considered. The lateral earth pressure response due to horizontal movement of soils with 44, 37, and 30 degree friction angles are shown in Figure 4.16. As a surface moves away from the soil mass, the soil enters an active soil state, shown as a negative deflection. A passive soil state is the movement of a surface towards the soil mass, shown as a positive deflection. A higher friction angle soil that is compacted requires less movement to activate fully passive and active soil states, than a lower friction angle soil that has not been compacted during backfilling. The NCHRP relationship was shifted across the horizontal axis so that the at rest coefficient of lateral earth pressure is equal to 1, a typical value used for compacted soil (Clough et.al 1990). This was consistent to the experimental conditions used during Walton's (2015 a) experimental regime and theoretically improved model accuracy.

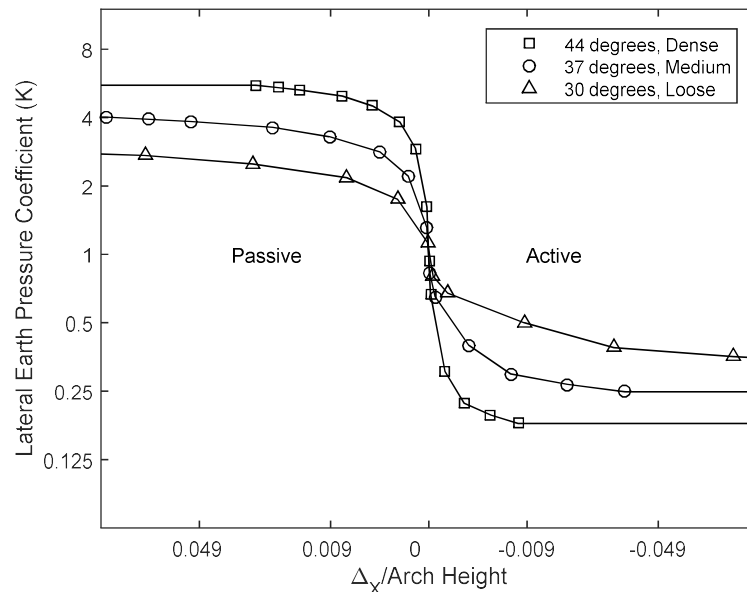


Figure 4.16 Soil Response Predicted Using NCHRP (Barker et al. 1991)

Force and stiffness were calculated using the lateral earth pressure for each spring. The force in the spring was calculated as the product of the vertical soil pressure, the lateral earth pressure coefficient, and the tributary area of the soil-spring. The tributary area (dA) for a current two dimensional analysis was the transverse spacing of the arches multiplied by the vertical projection of the arch element attached to the soil-spring. The vertical projected area of an arch element at any angle of orientation (α) for a horizontal soil-spring can be seen in Figure 4.17. Note that in Figure 4.15, the apex node does not have a soil-spring attached to it because the vertical projected area of an arch node at the apex was essentially zero leading to a small or zero soil force. Due to the element sizes in the model being relatively small ($1/80^{\text{th}}$ of the arc length), the absence of one spring does not affect the results noticeably.

$$F_{spring} = \sigma_{vertical} * K_{soil} * dA$$

Equation 1

Tangent stiffness (S) of the soil-spring was calculated as the slope of the force-displacement relationship at the current horizontal displacement (Δ_{spring}) and at a small distance ($d\Delta$) away from Δ_{spring} , which was approximated using a numerical derivative. Each soil-spring contributed only axial stiffness.

$$S_{Axial} = \frac{F_{Spring}(\Delta_{spring} + d\Delta) - F_{Spring}(\Delta_{spring})}{d\Delta}$$

Equation 2

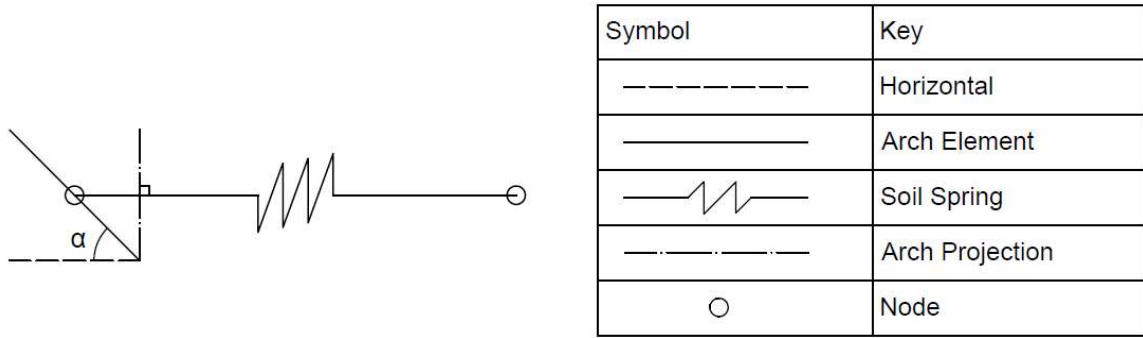


Figure 4.17 Horizontal Spring and Projected Arch Area

4.4. Proposed Modifications to the Existing Model

While the Existing Model adequately predicted the response of the arch system during backfilling and apex loadings (Walton et al. 2015 a), model accuracy decreased when the arch was subject to loads offset from the arch apex. It was clear that changes to the model were required to achieve a more accurate response during all load cases. Walton et al. (2015 a,b,c) also recommended including the effect of friction between the soil-springs and the arch as a method to better capture the soil response. This will result in angled soil-springs, the inclusion of which will add vertical confinement as well as simulate arch-soil friction, two additions to the model that Walton et al. (2015 b,c) expects will increase accuracy of the soil-spring model.

Three options were considered in this study: a Three Spring Model, Radial Spring Model, and a Friction Angle Spring Model.

The Three Spring Model was an adaptive model that accounts for the friction between the soil and the arch using a Coulomb soil force model and changes the direction of the soil reaction depending on the movement of the arch at each node. Each arch node was connected to three soil-spring elements to represent at-rest soil conditions as well as active and passive soil states. The at-rest soil-spring was horizontal and the active and

passive soil-springs were angled at the soil-wall friction angle ($\pm\delta$). As the arch moves into or away from the soil, the corresponding soil-spring will activate and provide the soil reaction at the angle of that soil state.

The Radial Spring Model oriented each soil-spring radially away from the arch to capture the normal pressure of the soil against the arch decking. It was predicted that aligning the springs in this direction will better simulate the reaction of the soil against a low friction decking material.

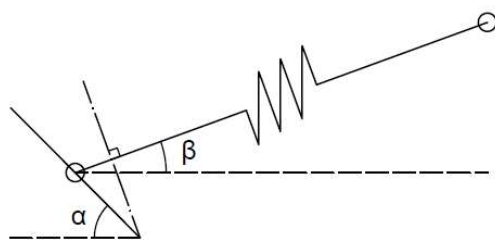
The Friction Angle Spring Model oriented each soil-spring in the same direction, the characteristic soil friction angle. Each of these three modeling approaches is explained in greater detail in the following sections.

4.4.1. Implementation of Angled Soil-springs

The addition of angled soil-springs allowed the soil-spring model to capture vertical constraining effects of the soil. The lack of vertical constraint in the system was mentioned as a possible cause for the inaccuracy of the model by Walton (2015 c). In the case of offset live loads, the Existing Model over-predicted both the vertical displacement of the arch into the soil as well the lateral earth pressure coefficient (K_{soil}) of the soil near the apex. Walton (2015 c) stated that this was likely linked to the absence of vertical soil confinement and frictional force between the arch and the soil. Movement of the arch at the shoulders due to applied service loads was primarily perpendicular to the arch. Near the shoulders and apex, this means that the arch displacements contain a vertical component that was unrestrained by the existing horizontal soil-springs.

Angled soil-springs used the same NCHRP load displacement relationship that was used for horizontal soil-springs. The lateral earth pressure coefficient depends on the

relative displacement of the arch in the direction of the soil-spring. The angled spring models incorporated the Rankine model used by the Existing Model, calculating the soil reaction assuming it acts on a projection of the arch element perpendicular to the soil-spring. To implement angled soil-springs in the model, two major changes were made to correctly calculate the reactive force of the soil-spring: the projected area of the arch element that was perpendicular to the soil-spring was used, and the arch node's deflection in the direction of the soil-spring was used to determine K . These changes allowed the model to accurately determine the reactive force and stiffness of a soil-spring at any orientation. The projected area for an angled soil-spring can be seen in Figure 4.18. Radial soil-springs act normal to the arch element, therefore in Figure 4.18 angles α and β were equal and the arch projection was equal to the arch element.



Symbol	Key
-----	Horizontal
—————	Arch Element
—⚡—	Soil Spring
-----	Arch Projection
○	Node

Figure 4.18 Angled Spring and Projected Arch Area

4.4.1.1. Radial Springs

One instance of angled soil-springs that was considered to improve the soil-spring model was the reorientation of each of the horizontal springs to the radial direction.

Bannon (2009) used radial soil-springs to model a CFFT buried arch bridge. The Radial Spring Model, shown in Figure 4.19, applied a force normal to the arch at each element and considered the spring as acting on the total tributary area of an arch element, as

opposed to the vertical projection of the arch element used in the existing horizontal spring model. Radial soil-springs added mostly horizontal restraint at the supports and vertical restraint at the apex, possibly addressing the issue of the Existing Model deflecting more at the shoulders and apex than the experiment. The tributary area for a radial spring was the spacing of the arches by the length of the arch element. This may give the model the confinement required to simulate more realistic soil pressures at the shoulders and apex of the arch.

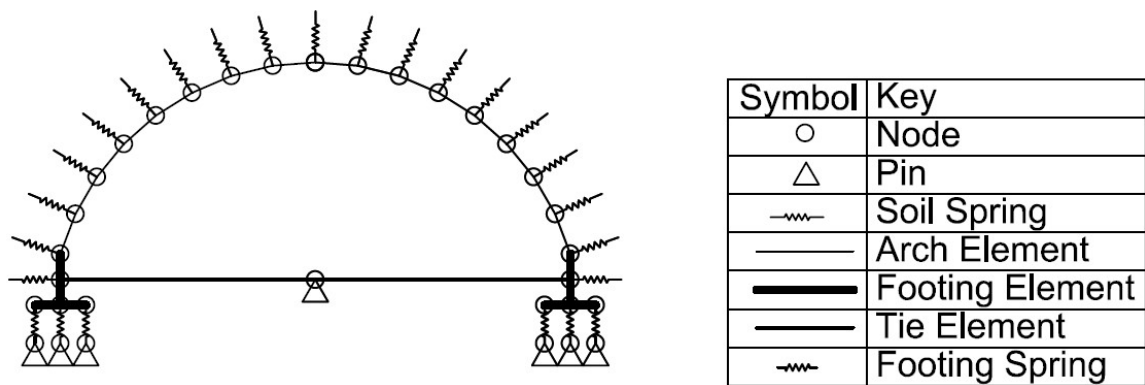


Figure 4.19 Radial Spring Model

4.4.1.2. Friction Angle Springs

Another option to implement angled soil-springs was to angle each soil-spring in the same direction. The Friction Angle Spring Model oriented each spring at the soil friction angle, which Walton (2015 a) experimentally determined to be 44° for the backfill soil used in the laboratory buried arch tests, shown in Figure 4.20. The springs oriented in this direction were intended to simulate the reactive force of the soil in the direction of the friction angle of the soil used in the experiment.

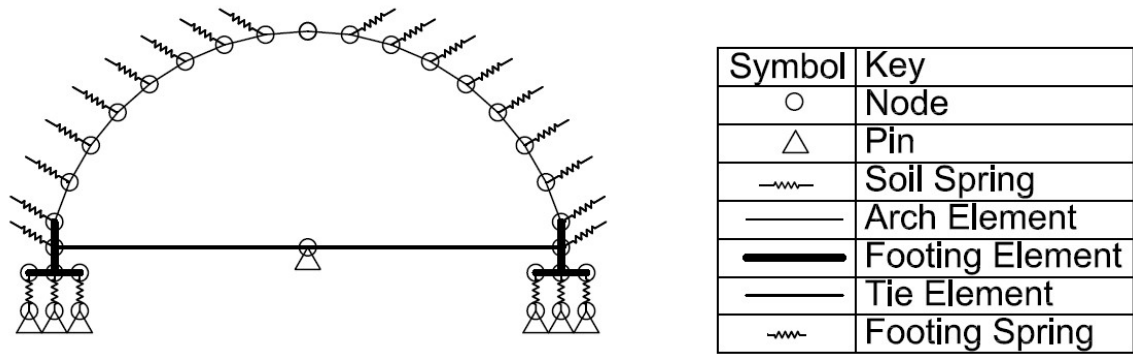


Figure 4.20 Friction Angle Spring Model

4.4.2. Three Spring Model

The Three Spring Model, drawn with a coarse mesh in Figure 4.21 and at the nodal level in Figure 4.22, calculated a reactive force for three springs and aligns the resultant of the soil reaction by multiplying each spring by a ratio that depends on the relative horizontal displacement (Δ_x) of the arch at the node. In vertical retaining wall design using a Coulomb soil model, the soil reaction force orientation and magnitude depend on the relative horizontal displacement of the wall. The soil reaction was oriented at $+\delta$, the soil-wall friction angle, when the wall moves away from the soil in an active soil state, and the reaction was oriented at $-\delta$ when the wall moves into the soil in a passive soil state. To model this, active and passive soil-springs were oriented at $+\delta$ and $-\delta$ from horizontal. Typically values of δ range from around a one-third to two-thirds of the soil friction angle (Das, 2011).

The Existing Model calculated the reaction force of the soil based on a vertical projection of the arch element moving horizontally relative to the soil. The Three Spring Model calculated the soil reaction using the same vertical projection of the arch area seen in Figure 4.17, and the horizontal movement of the adjoining arch node for all three springs for each node. This was consistent with the retaining wall design methods used in

the Existing Model and adapted to fit with the Coulomb model. Horizontal wall movement dictates the lateral earth coefficient for all springs. Fully-active and fully-passive values of deflection are defined as the solid vertical lines in Figure 4.23, Δ_p is shown as the passive soil state deflection limit. Using these limits, the ratio of the relative displacement to the limit of the active or passive soil state was calculated in Equation 3 through Equation 5.

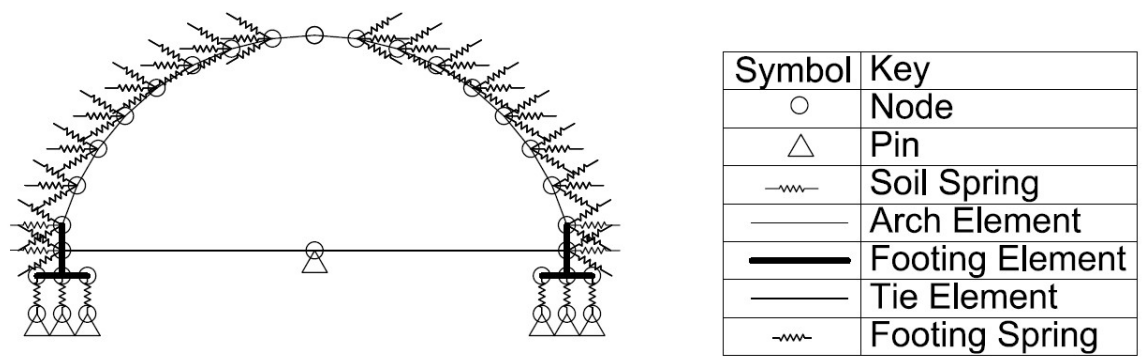


Figure 4.21 Three Spring Model

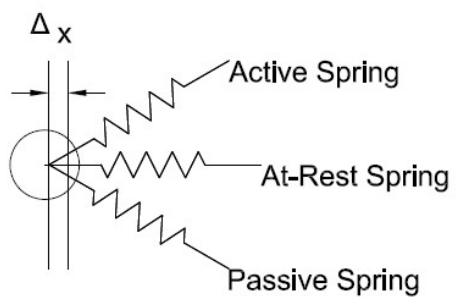


Figure 4.22 Three-Spring Model Arch Node, Soil-springs, and Deflection

The ratio (γ) was calculated for each of the springs in the three spring system and multiplied by the spring's axial force. Therefore if the arch was moving into the soil, then only the at-rest and passive soil-springs were restraining the node and the active soil-

spring did not contribute to the system. An active soil state was defined here as the arch moves away from the soil (-) and passive was defined as the arch moves into the soil (+).

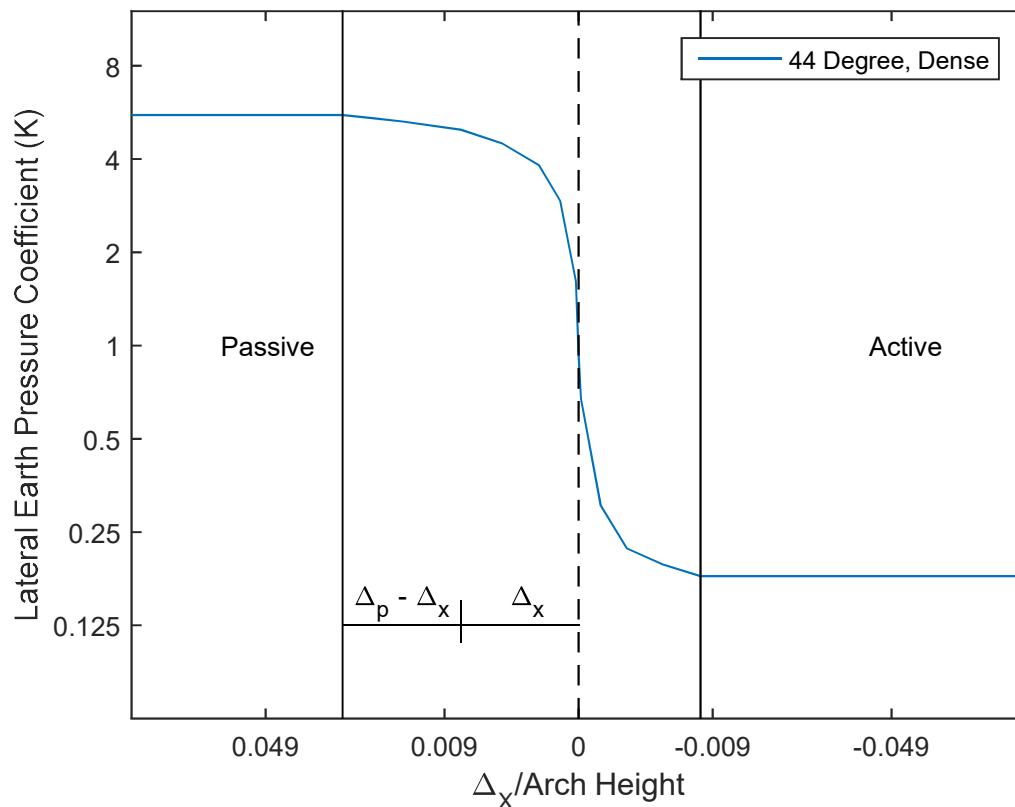


Figure 4.23 Soil-spring Deflection Limits

Values for γ in active and passive springs were calculated as the relative horizontal soil-spring movement divided by the soil limit state associated with the movement direction. For each spring group there were two cases, the arch moving into the soil and the arch moving out of the soil. The ratios for the two cases were calculated differently and are shown in Equation 3 and Equation 4.

If:

$\Delta_{passive\ deflection\ limit} \geq \Delta_x \geq 0$, the soil is entering a passive soil state.

$$\gamma_{Passive} = \frac{\Delta_x}{\Delta_{passive\ deflection\ limit}}, \gamma_{Active} = 0$$

Equation 3

If:

$\Delta_{active\ deflection\ limit} \leq \Delta_x \leq 0$, the soil is entering an active soil state.

$$\gamma_{Passive} = 0, \gamma_{Active} = \Delta_x / \Delta_{active\ deflection\ limit}$$

Equation 4

At-rest springs ratio are the difference between one and the above ratio.

$$\gamma_{At-rest} = 1 - \gamma_{Passive} \text{ or } 1 - \gamma_{Active}$$

Equation 5

Figure 4.24 illustrates the percentage of spring engagement as the node moves from a zero deflection to the deflection limit. These ratios were multiplied by the calculated applied force for each of the respective springs. Since the spring stiffness was calculated using the forces of the springs, the stiffness was scaled by γ for each spring in the three spring system (see Equation 2). This allowed the soil reaction magnitude to be nearly the same as the horizontal soil-spring model's soil reaction while also including the effects of friction between the arch and soil.

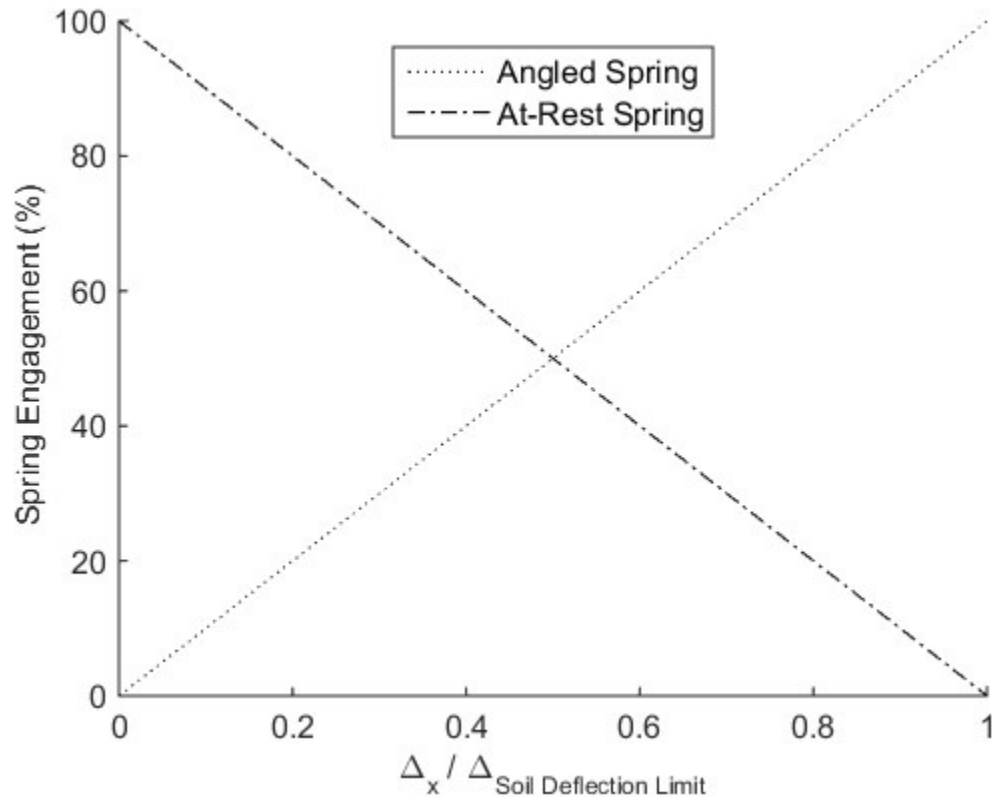


Figure 4.24 Spring Interpolation for Three Spring Model

4.4.2.1. Modification to the Three Spring Model

The Three Spring Model as originally implemented with linear interpolation between soil regimes (described in 4.4.2 of this thesis) was unable to find a solution for the entire analysis for either arch geometry. Soil-spring interpolation was suspected to be the reason. To explore this further, a different routine was implemented into the Three Spring Model to calculate the percent of engagement for each soil-spring at the node using a quadratic interpolation rather than the previously used linear method. The new method of calculating the ratio γ is defined in Equation 6 through Equation 8 **Error! Reference source not found.** **Error! Reference source not found.** This soil-spring interpolation method rapidly changed the distribution of the force applied by the soil-springs from the at-rest spring to the angled soil-spring when displacements were small

and as the displacement neared the soil deflection limit the majority of the soil reaction force was coming from the angled soil-spring.

If:

$\Delta_{passive\ deflection\ limit} \geq \Delta_x \geq 0$, the soil is entering a passive soil state.

$$\gamma_{Passive} = -\left(\frac{\Delta_x}{\Delta_{passive\ deflection\ limit}}\right)^2 + 2\left(\frac{\Delta_x}{\Delta_{passive\ deflection\ limit}}\right), \gamma_{Active} = 0$$

Equation 6

If:

$\Delta_{active\ deflection\ limit} \leq \Delta_x \leq 0$, the soil is entering an active soil state.

$$\gamma_{Passive} = 0, \gamma_{Act} = -\left(\frac{\Delta_x}{\Delta_{active\ deflection\ limit}}\right)^2 + 2\left(\frac{\Delta_x}{\Delta_{active\ deflection\ limit}}\right)$$

Equation 7

The at-rest spring ratio was calculated from the movement and that associated deflection limit.

$$\gamma_{At-re} = \left(\frac{\Delta_x}{\Delta_{state\ deflection\ limit}}\right)^2 - 2\left(\frac{\Delta_x}{\Delta_{state\ deflection\ limit}}\right) + 1$$

Equation 8

Equation 6 **Error! Reference source not found.** through Equation 8 **Error! Reference source not found.** are illustrated in Figure 4.25 where the spring engagement was dependent on the normalized deflection at the arch node over the soil deflection limit. The angled spring in the figure refers to the angled soil spring being activated by the movement. For example, if the arch moves into the soil the passive spring is being activated and the deflection limit refers to the passive deflection limit described in 4.4.2.

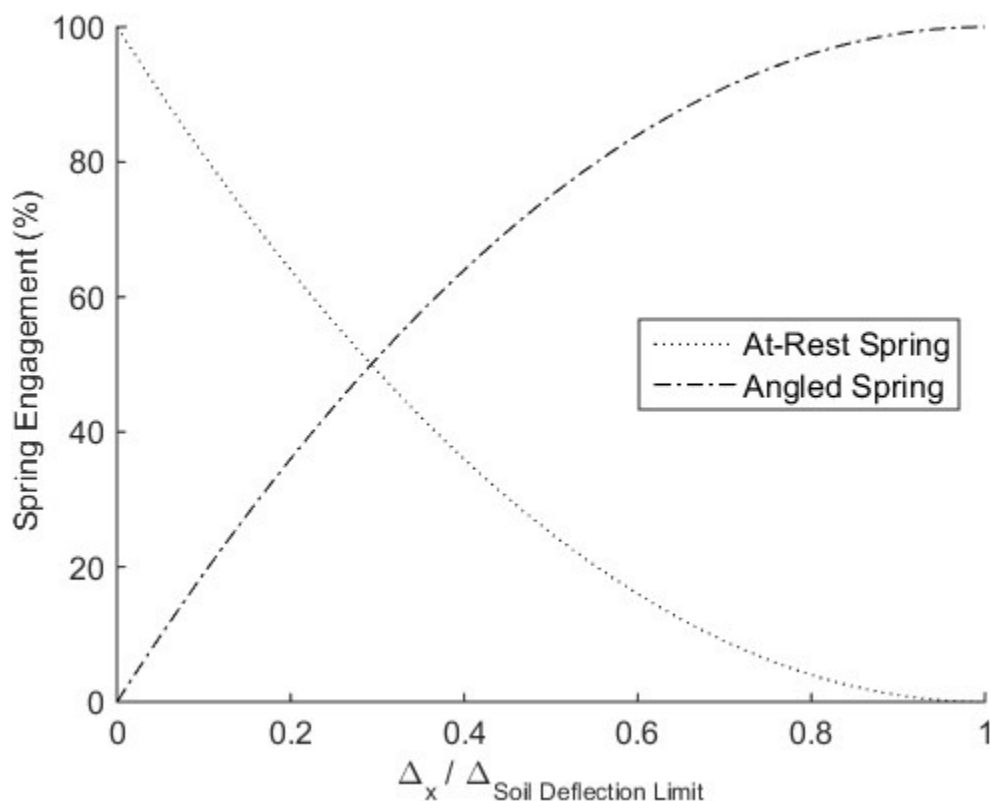


Figure 4.25 Quadratic Spring Interpolation in the Three Spring Model

4.4.2.2. Error in Three Spring Method

It was important that the three soil-springs do not apply a resultant force significantly different from the force applied by a single spring in the existing horizontal spring model. A study was conducted to assess the error due to the added springs in the Three Spring System. The case of the arch moving into the soil was investigated at one arch node as the deflection moved from fully at-rest to fully passive.

The nodal soil-springs seen in Figure 4.22 go through a horizontal displacement (Δ_x). Based on the load deflection curve in Figure 4.23, a lateral earth pressure coefficient and force were calculated as detailed above for the at-rest soil-spring at the deflection (Δ_x). Each soil-spring for the node was set equal to the force (F_{spring}) calculated and multiplied by the respective γ value based on the relative deflection. In this case where

the arch is moving into the soil, the active soil-spring contributed nothing and the at-rest and passive soil-springs were multiplied by non-zero γ values. The applied force was then calculated as the magnitude of the resultant for all three springs, seen in Equation 9 through Equation 11.

The horizontal and vertical resultants due to the two activated springs, at-rest and passive, were calculated as shown in Equation 9 and Equation 10. The resultant of the horizontal and vertical forces applied by the two soil-springs to get the resulting soil reaction force was calculated in Equation 11.

$$F_H = \gamma_{at-rest} F_{spring} + \gamma_{passive} F_{spring} \cos(\delta)$$

Equation 9

$$F_V = \gamma_{passive} F \sin(\delta)$$

Equation 10

$$F_{spring\ group} = \sqrt{F_H^2 + F_V^2}$$

Equation 11

Figure 4.26 shows the force due to the group of springs versus one horizontal spring normalized over the force applied by the horizontal spring in the one spring system. Two different soil-wall friction angles (δ) were considered, 20° and 30°, as a typical range of values for soil on wood (Barker et al. 1991). As the deflection moved from fully at-rest to fully passive, the error started at zero and was at a maximum at a

deflection halfway between the two soil state limits. This error was 3.1% for $\delta = 20^\circ$, and 6.7% for $\delta = 30^\circ$.

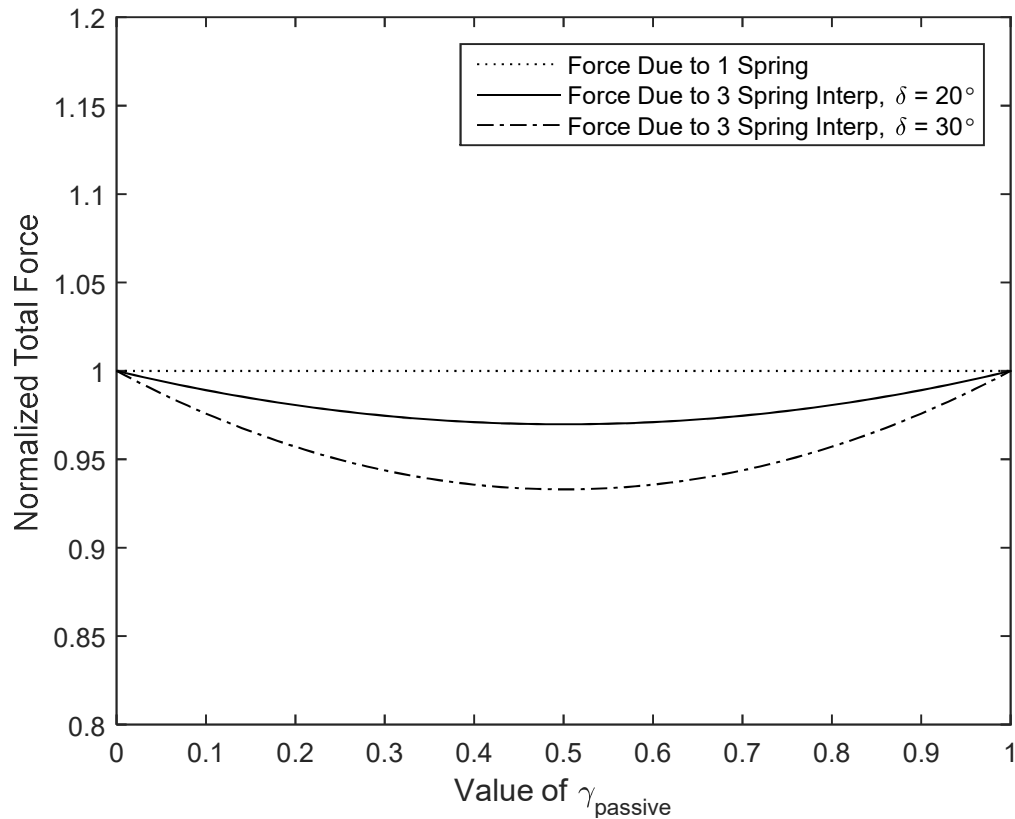


Figure 4.26 Normalized Spring Force vs Relative Deflection

4.4.3. Implemented Modifications to the Model

The Radial Spring Model, Friction Angle Spring Model, and the Three Spring Model were implemented in the soil-spring model. The Radial Spring Model and Friction Angle Spring Model were added due to the vertical restraint provided by each model's angled soil-springs. It was anticipated that the angled soil-springs would better predict the vertical soil pressures and arch displacement as the model nears the top of the arch. The Three Spring Model was a unique solution that considers movement of the arch

throughout loading cases when orienting the soil-springs and realistically applies the reactive soil force in the direction calculated when using a Coulomb model for soil.

4.5. Conclusions

This chapter discusses an analysis of the Existing Model's live load distribution as well as methods used to modify the Existing Model to improve model performance. The Existing Model used a Boussinesq load distribution model to predict the force on the arch due to live loads. Vertical pressures gathered from the tested scale arches show that the Boussinesq model poorly calculated the effect of the load away from the location of the load. Other soil distribution methods should be investigated to improve the accuracy of the model.

Three alternatives to the soil-spring orientation were discussed: the Three Spring Model, Radial Spring Model, and the Friction Angle Spring Model. The Existing Model was not able to capture any vertical soil restraint using horizontal soil-springs. These alternatives to the soil-spring model orient the soil-springs so that the resulting spring force simulated vertical and horizontal soil restraint. By using a Coulomb soil model, the Three Spring Model included the effect of friction between the soil and the arch. This alternative interpolated between three soil-springs depending on the relative movement of the arch at that node to simulate the soil in active and passive states.

CHAPTER 5

MODEL PREDICTIONS AND COMPARISONS WITH EXPERIMENTAL RESULTS

5.1. Introduction

This chapter focuses on the comparison between the alternative soil-spring models detailed in the previous chapter. Short and tall arch models were compared with the scaled experimental test moments and displacements for each phase of the analysis: backfilling, service live loading, and ultimate loading.

5.2. Model Description

The base model in this research simulated response of the half scale experimental steel arch built and tested by Walton et al. (2015 a). The steel arches were chosen due to the ease and accuracy of computing internal arch stress resultants from the experimentally measured strains. The arch cross section was selected to best replicate the horizontal pressure of a full scale arch; this was explained in more detail by Walton (2015 c). The main structural member of the short arch was a 50 mm by 50 mm curved steel bar and the tall arch was a 38 mm by 100 mm steel bar oriented so that the arch will be in weak axis bending. Under service loading these arches were designed to remain linear elastic.

Soil in the soil-spring model mimicked the backfill soil used in the lab experiments, which was tested by Walton et al. (2015 a,c) and the parameters were entered into the model. The soil used in the lab had a bulk density of 2.2 Mg/m^3 and an internal soil friction angle (ϕ) of 44° assuming a dense compaction level. The reaction

force of the soil-springs in the model was defined by the NCHRP (Barker et al. 1991) load deflection relationship explained earlier in this report.

The models analyzed in this report will be compared to the Existing Model as well as the data gathered from experiments conducted and designed by Walton et al. (2015 a,c). The models used for comparisons were the Radial Spring, Friction Angle Spring, and the Three Spring Models. The soil-wall friction angle (δ) used for the Three Spring Model was 25° as an average for the typical values of the soil-wall friction angle for soil on wood for both the short and tall arches. Moments along the span control the design in the arches as they are efficient axial members and are subject to small shear forces. According to Walton et al. (2015 b) the controlling load cases were apex and shoulder moment during backfilling, apex moment due to apex live load, and shoulder and footing moment due to a 60% offset service load. Arch response under these load cases and others were examined in the following sections. Three Spring Model results using the modified quadratic interpolation routine were presented. The Three Spring Model using the linear spring interpolation method was only able to calculate results for two load cases: short arch backfilling and short arch apex service loading. The results for these two load cases were presented as a comparison between the two interpolation routines, the Existing Model, and the experimental moments.

5.3. Backfilling Response for the Short Arch

The buried arch structure underwent a significant locked-in moment due to backfilling that can control design in some cases. For all models, a consistent lift height of 200 mm was applied to alternating sides of the arch to analyze the replicate the un-symmetric construction backfill sequence seen in the field. Backfilling continued to a

final an apex soil cover of 610 mm for a total height of soil above the arch-foundation interface of 1.83 m. The Existing Model did an adequate job at capturing the apex and shoulder moments at the end of backfilling while over-predicting the moments at the arch foundation interface.

All model variations predicted a peak or plateau in moment at the apex when the backfill lifts were around shoulder height, when backfilling was roughly 85% complete, consistent with experimental results showing the maximum moment occurring several lifts before the end of backfilling. Moments at the apex, foundation, and shoulder during backfill can be seen in Figure 5.1 through Figure 5.3, respectively. The angled spring models also predicted a drop in moment at the apex after the maximum was reached, similar to the drop seen experimentally. The Existing and Three Spring Models show a moment plateau after the backfill reaches the shoulders. Results taken at the shoulders were located halfway between the arch apex and the foundation. Moments due to the final lifts were seen in the Existing and Three Spring Model to have an almost negligible effect on the apex moment, where both angled spring models saw a reduction in the negative moment.

The maximum moment was seen experimentally as 2.1 kN·m, higher than the maximum moment seen in any of the models. The maximum moment predicted by the Radial Spring Model was closest to experimental results at 1.8 kN·m, approximately 8% below the measured value at lift 19. The final backfilling moment varied for each model. The Three Spring Model resulted in a moment that varied less than 5% from the Existing Model throughout backfilling. Moments throughout backfilling predicted by the Radial Spring Model and the Friction Angle Spring Model were greater than those computed by

the Existing Model until lift 20, then the moment for those models at the apex dropped while the Existing and Three Spring Models continue to build moment. Apex moment at the end of backfill was approximately 30% less than the experimental for the Friction Angle Spring Model, 38% less than the experiment for the Radial Spring Model, and 10% less than the experiment for both the Existing and Three Spring Models.

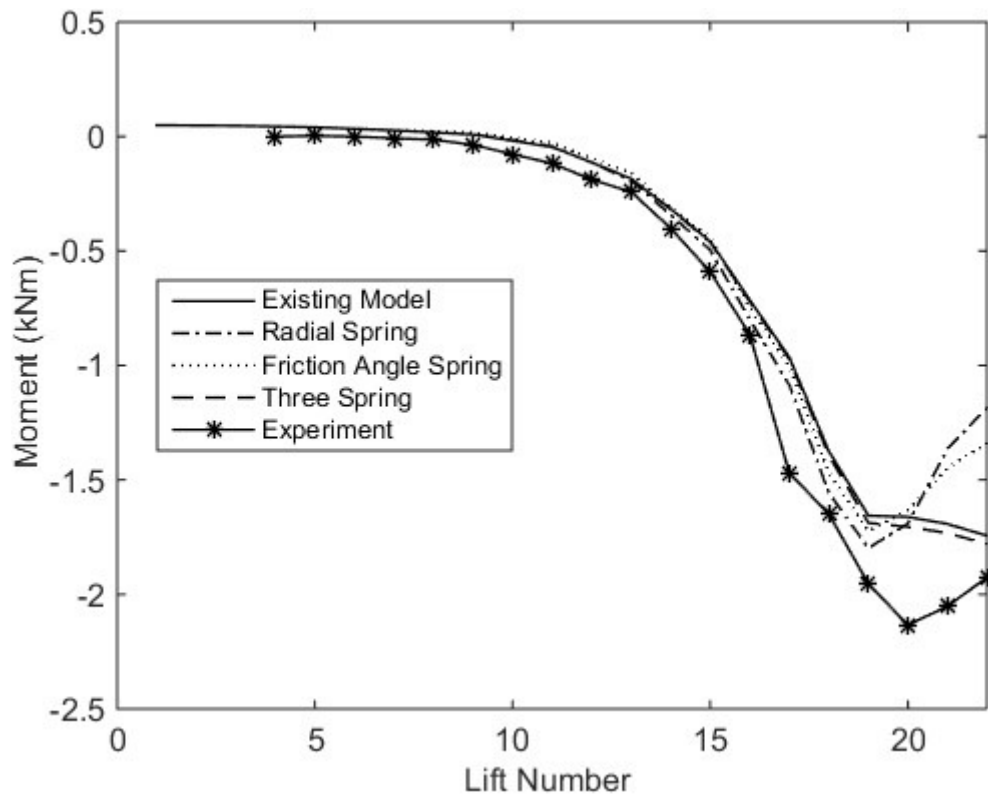


Figure 5.1 Short Arch Backfilling Moments at Apex

Foundation moments during backfilling, shown in Figure 5.2, were over-predicted by each model for the majority of backfilling. The models predicted almost triple the measured response during backfill when the backfill soil height was at the shoulders of the arch near lift 18. The Friction Angle Spring Model predicted the smallest maximum moment of 140% higher than the experiment and the Radial Spring Model predicted the largest maximum moment of 190% higher at lift number 18. The Existing and Three

Spring Model both ended backfilling with roughly a 60% higher moment than found experimentally. The angled spring models predicted a drop in negative moment at the foundation after peaking at lift 18. The Radial Spring Model predicted the final backfill moment seen experimentally within 0.1% and the Friction Angle Spring Model under-predicted the final backfill moment within 10%.

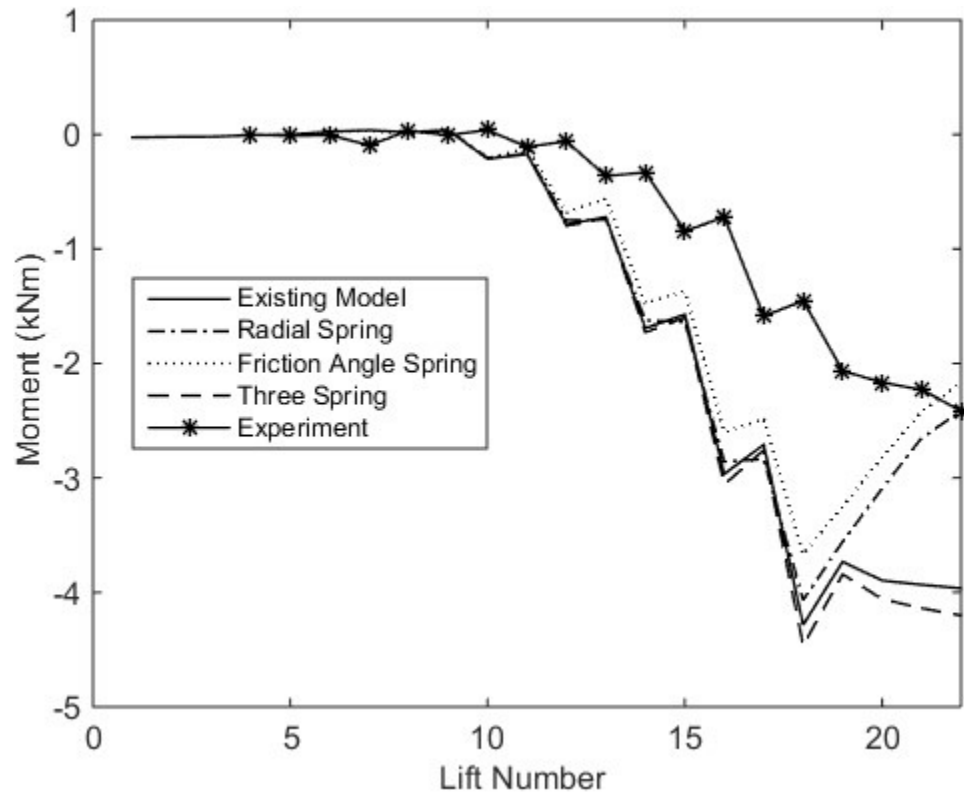


Figure 5.2 Short Arch Backfilling Moments at Foundation

Moments at the shoulder (Figure 5.3), located halfway between the arch apex and foundation, were much closer to experimental values when compared to the foundation moments during backfill. The maximum moment was predicted by the Three Spring Model during backfilling at 30% higher than the experimental moment. The Existing and Three Spring Models both predicted a small drop in shoulder moment after peaking at lift 18, also seen experimentally at lift 20 while the Radial and Friction Angle Spring Models

predicted a drop in moment equal to 25% and 42% of the maximum moment. The Three Spring Model and the Existing Model over-predicted the final moment by 10% and 6% respectively, while the Radial Spring and Friction Angle Spring Model under-predicted the final moment by about 25% each.

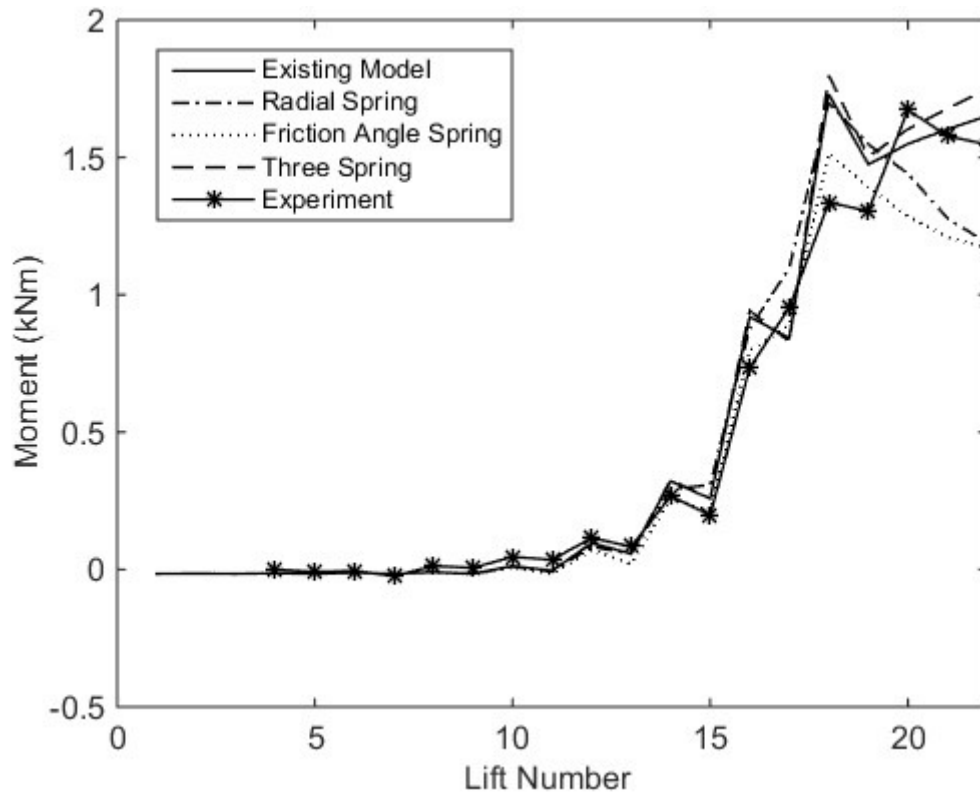


Figure 5.3 Short Arch Backfilling Moments at Shoulder

Moments along the span at the end of backfilling can be seen in Figure 5.4. The models followed the same trend, showing a negative moment at the footings and apex, and a positive moment at the shoulders. The moments at the shoulder, footings, and apex of the arch control design during backfilling. The Existing and Three Spring Model better predicted the controlling moments while the Radial and Friction Angle Spring Models predicted lower moments at almost all locations along the arch span. The Existing and Three Spring Models also predicted a more symmetric response compared to the Friction

Angle and Radial Spring Models, which could signify that the angled soil-springs are more susceptible to the un-symmetric backfilling. The highest experimentally determined moment post backfill was located at the arch-foundation interface at $2.9 \text{ kN}\cdot\text{m}$, the Existing and Three Spring Models over-predicted the moment by 38% while the Radial and Friction Angle Spring Models under-predicted the moment by 14% and 25% respectively. Apex moments were under-predicted by all models: 11% by the Existing Model, 10% by the Three Spring Model, 32% by the Friction Angle Spring Model, and 40% by the Radial Spring Model.

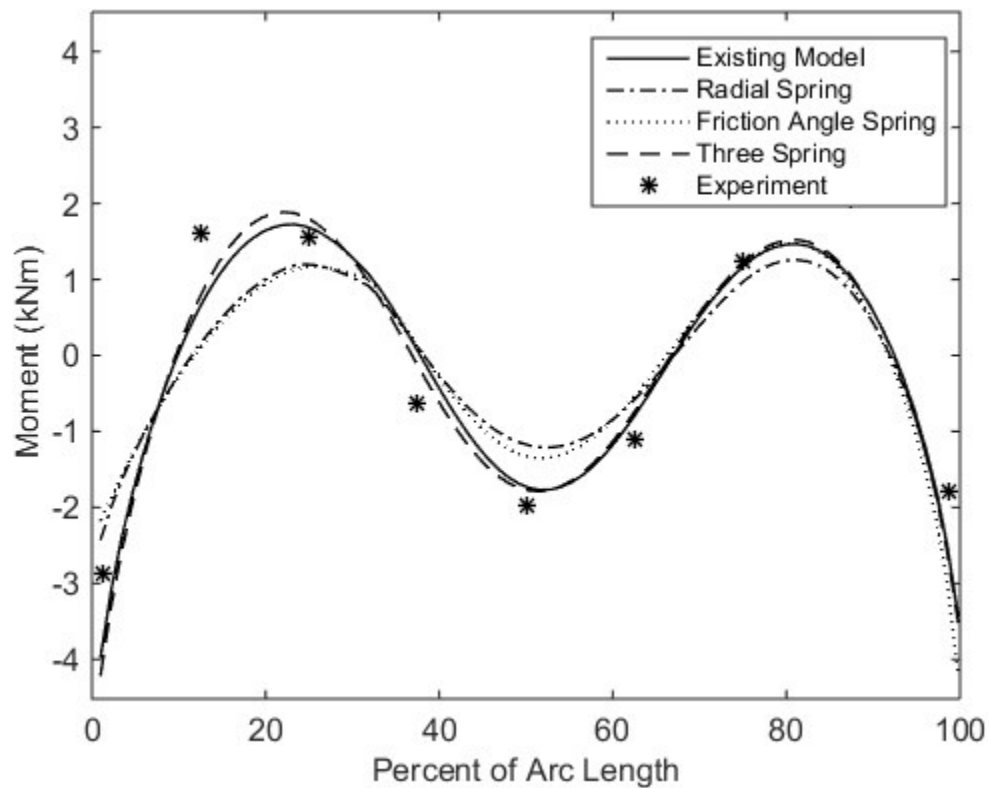


Figure 5.4 Short Arch End of Backfill Moment

Figure 5.5 illustrates the moment distribution along the span due to backfilling calculated from the Existing and both iterations of the Three Spring Model. The original soil-spring model employing the linear interpolation routine is marked as the 'Linear

Interp' while the modified Three Spring Model employing the quadratic interpolation routine is marked 'Quadratic Interp.' Moments along the span varied little between the Existing and Three Spring Models, differing less than 1% from the apex moment predicted by the Existing Model. The apex moment was under-predicted by less than 10% from the experimental value by each model. The shoulder moment near 25% of the arch length showed the most variation from the Existing Model, 5% for the original Three Spring Model and 9% for the modified Three Spring Model.

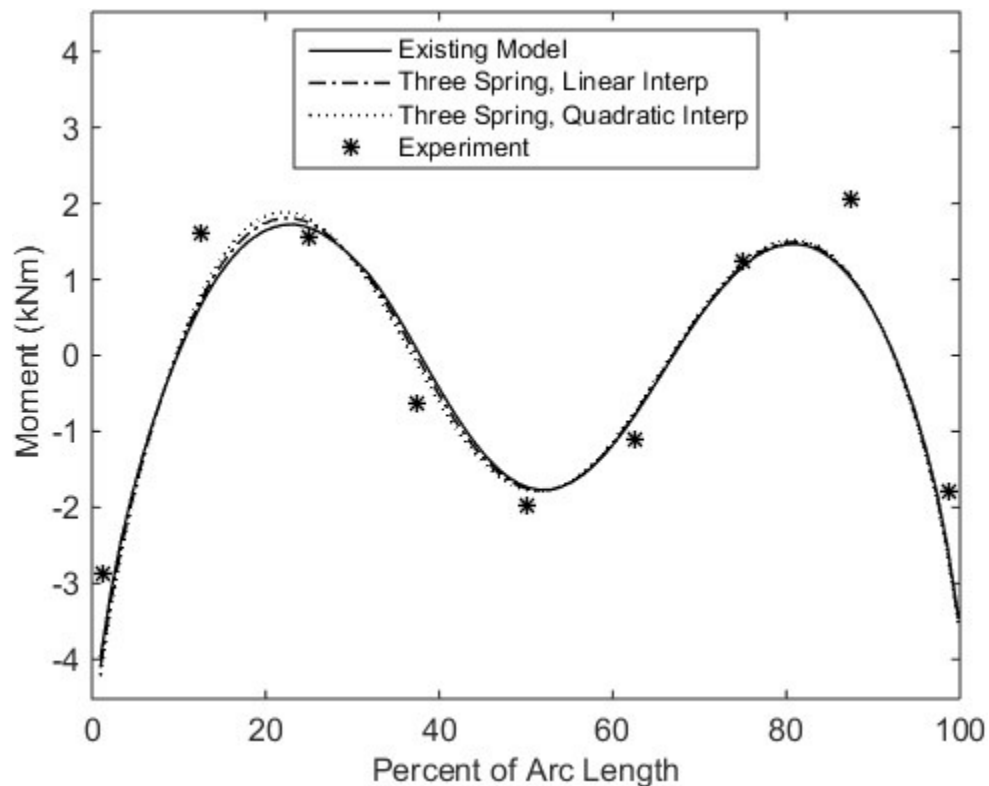


Figure 5.5 Short Arch End of Backfill Moment, Three Spring Model Comparison

The vertical component of the deflection at each node in the arch can be seen in Figure 5.6. Multiple data points at the same location indicate the movement in each of the three arches in the experiment. Each model generally followed the same deflected shape, the apex moving upward and the shoulders moving downward due to the stepped

backfilling. Apex displacement was well predicted by the Existing and Three Spring Models. Experimentally, the shoulder experienced the highest displacement but was under-predicted by all models: 55% by the Existing Model, 56% by the Three Spring Model, 70% by the Radial Spring Model, and 72% by the Friction angle Spring Model.

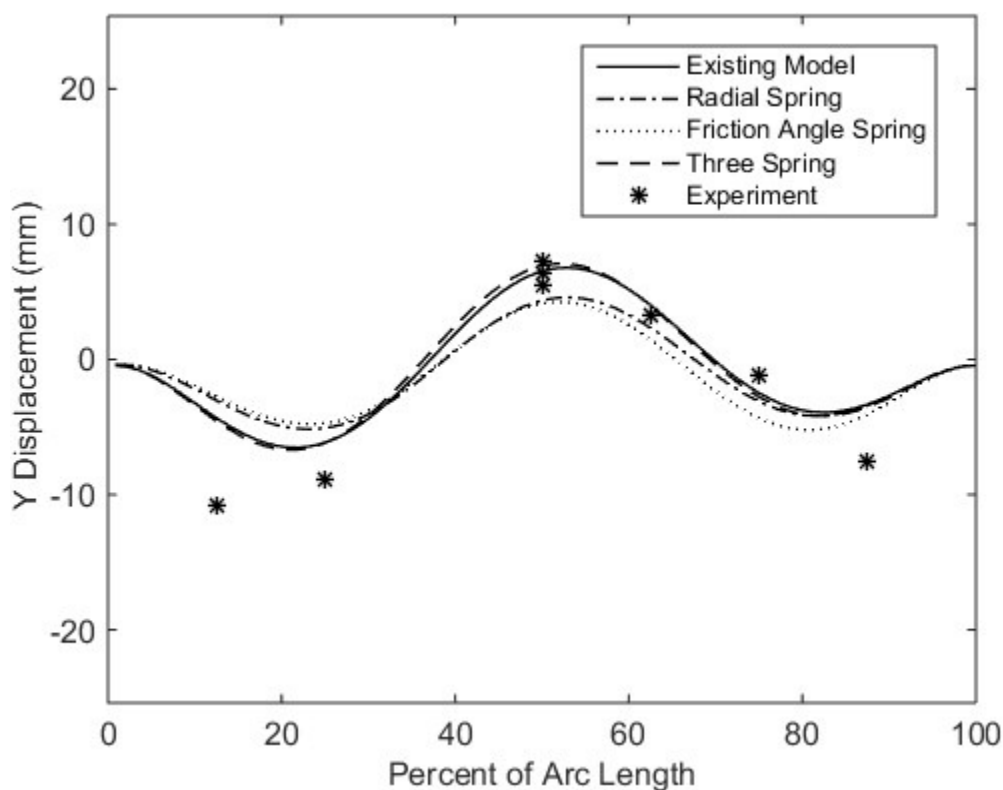


Figure 5.6 Short Arch End of Backfill Vertical Displacement

5.4. Backfilling Response for the Tall Arch

Backfilling lifts were placed for an apex soil cover of 610 mm for a total height of soil above the arch-foundation interface of 2.9 m. Moments throughout the backfill analysis for the completed tall arch models can be seen in Figure 5.7 through Figure 5.9.

The tall arch moment response during backfilling at the apex is shown in Figure 5.7. Each model other than the Existing and Three Spring Model predicted a peak moment during backfilling and then a drop in the negative moment. The Existing Model

disagreed and continued to build moment to the end of backfilling. Maximum moment predicted by the Radial and Friction Angle Springs were within 1% of the measured moment. The drop in negative moment measured was 19% while the Radial Spring Model predicted a 40% drop and the Friction Angle Spring Model predicted a 30% drop at the apex.

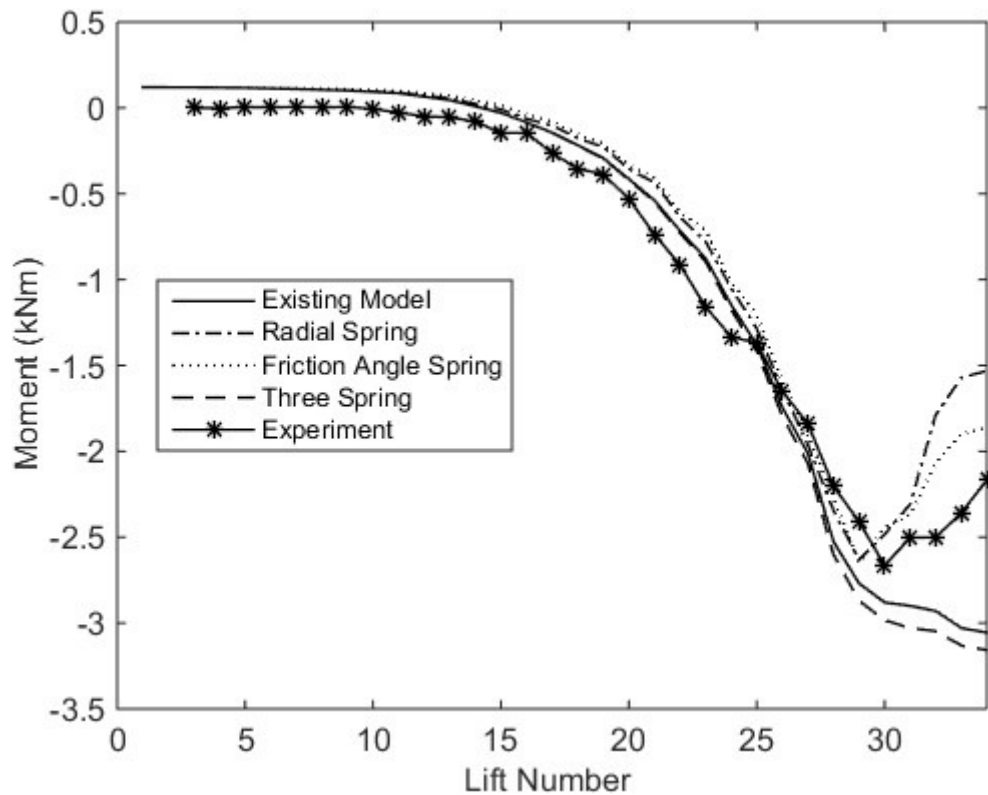


Figure 5.7 Tall Arch Backfilling Moments at Apex

Measured foundation moments, shown in Figure 5.8, generally fell between the Existing and the two angled spring models until lift 25 then again from lift 30 to the end of backfilling. The Existing Model predicted a peak moment during backfill 70% higher than the measured moment, then the moment was reduced to within 7% at the end of backfill. The four models predicted a similar drop in negative moment after hitting a peak during backfill of approximately 2.7 kN·m.

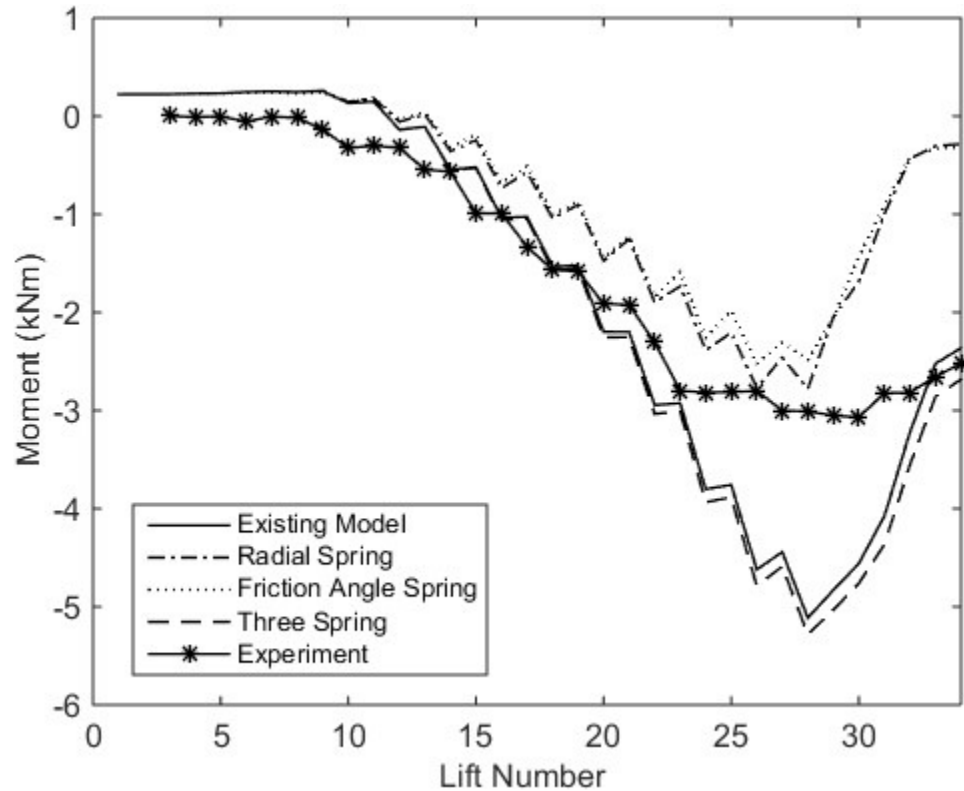


Figure 5.8 Tall Arch Backfilling Moments at Foundation

Experimental tall arch shoulder moments, shown in Figure 5.9, are generally between the responses predicted by the Existing and angled spring models past lift 23. The experimental moments followed the trend of the Radial Spring Model until the moment peaked at the shoulders then while the Radial Spring Model lost moment, the moment in the experiment continued upward then plateaued. The final moment at the end of backfill matched better with the Existing Model, only over-predicting by 6%, while the Radial Spring and Friction Angle Spring Models under-predicted the final moment by 33% and 39% respectively.

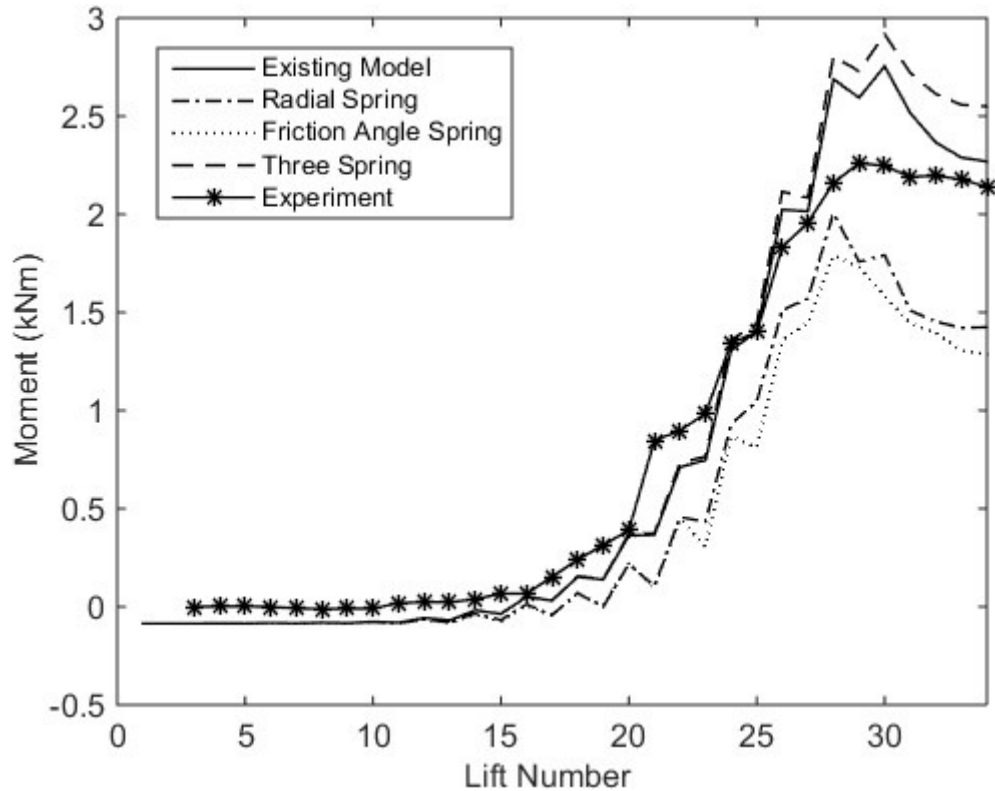


Figure 5.9 Tall Arch Backfilling Moments at Shoulder

Tall arch moments at the end of backfilling, shown in Figure 5.10, follow a similar trend to what was seen in the short arch moments, negative at the apex and footing and positive at the shoulders. All models predicted an un-symmetric response but the peak shoulder moment appeared on opposite sides when comparing the Existing and angled spring models. The Friction Angle Spring Model predicted the apex moment within 2%, while the Radial Spring Model under-predicted the moment by 20% and the Existing Model over-predicted by 62%. Apex moment was over-predicted 66% by the Three Spring Model. At the shoulder near 25% of the span the Three Spring Model predicted an 8% higher moment due to backfilling. The Three Spring Model predicted a left footing moment 14% higher than the Existing Model.

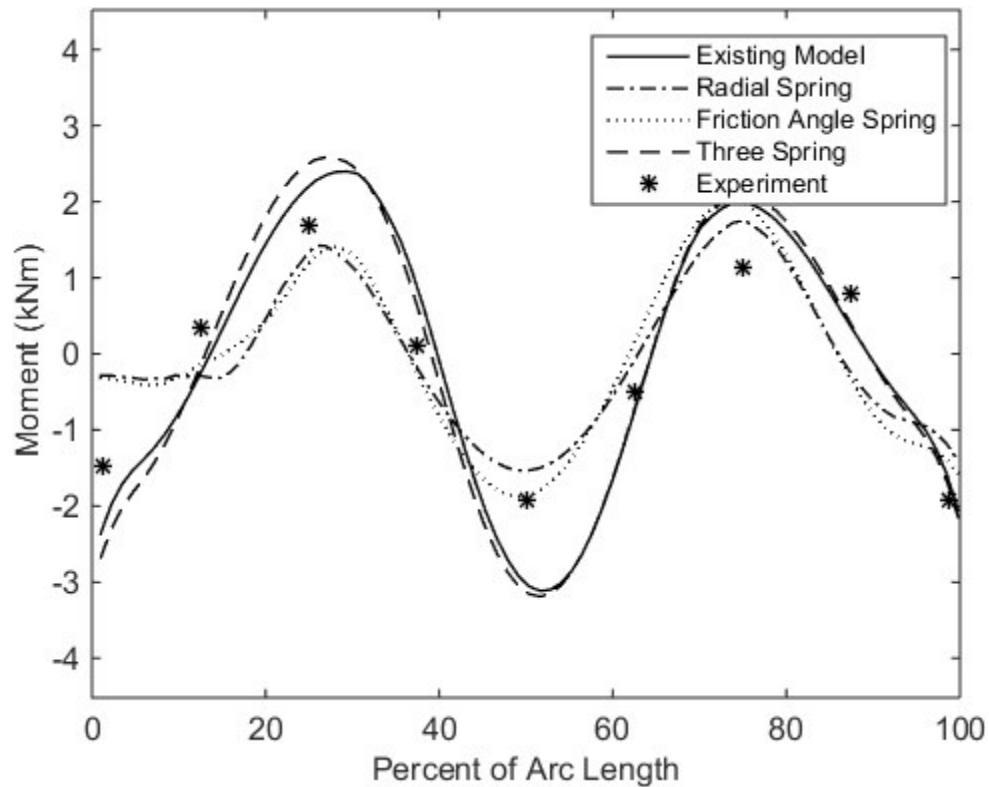


Figure 5.10 Tall Arch End of Backfill Moment

Tall arch vertical displacement at the end of backfill is shown in Figure 5.11. The Existing Model over-predicted the displacement at the apex by 50% and under-predicted the displacement at the shoulders by 25%. The Radial and Friction Angle Spring Models better predicted the apex displacement, within 6% and 8.5% respectively. The angled springs restrained the tall arch from moving vertically more than the Existing Model due to the orientation of the soil-springs, leading to an apex displacement similar to what was seen experimentally.

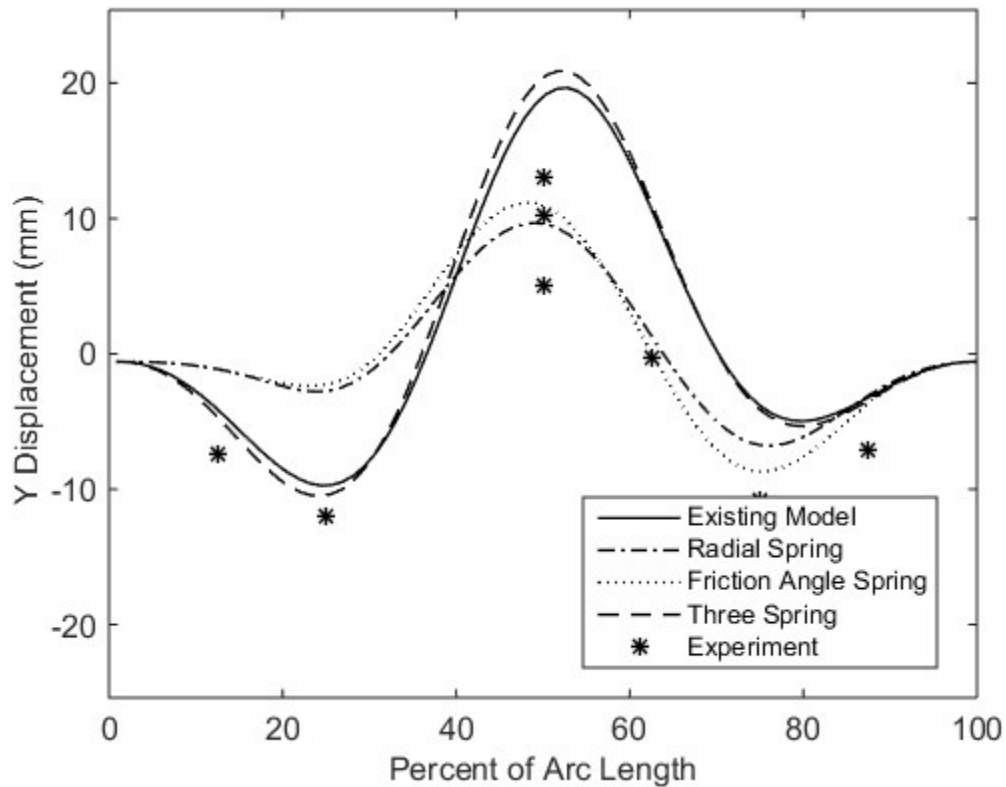


Figure 5.11 Tall Arch End of Backfill Vertical Displacement

5.5. Live Load Response of Short Arch

The service live load analysis mimicked the load applied to the experimental arches. After backfilling, the arches were subject to a point load of 84 kN applied at multiple locations within the center 60% of the span starting with the apex then alternating the load position in 10% of the span increments. In the following sections, the moment and vertical displacement response due to live load only from each model were examined, where live loading at the apex, 10% of the span from the apex, 20% of the span from the apex, and 30% of the span from the apex were considered.

5.5.1. Apex Service Live Load

Figure 5.12 illustrates the moment distribution along the arc length of the span in response to an apex service load for the short arch. The apex moment was predicted by

the Three Spring Model to within 1% of the experimentally derived moment. All models predicted the apex moment to within 11% of the experimental value. The Radial Spring Model best predicted the shoulder moments on both sides of the arch where the other models over-predicted the experimental moment at the shoulder at 25% of the span by approximately double. At the right footing, all models generally predicted the moment well, however on the left side, the Existing and Three Spring Model over-predicted the footing moment where the measured value was small.

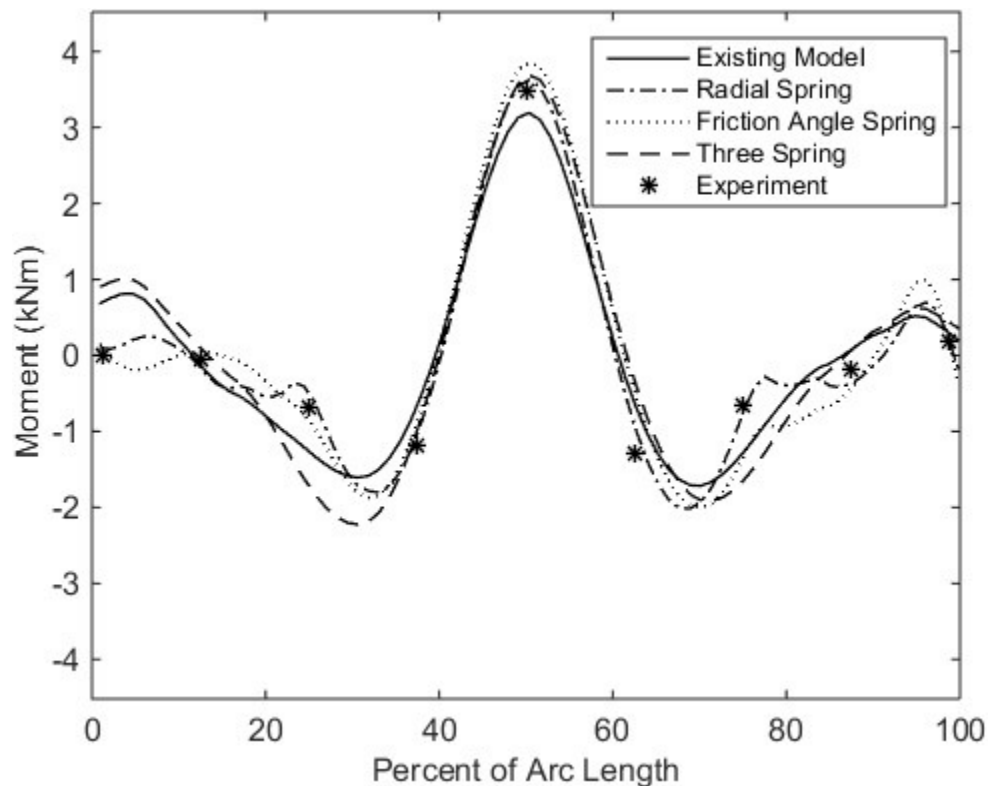


Figure 5.12 Short Arch Apex Service Load Moments

Apex service load moments for the short arch calculated from the two iterations of the Three Spring Model are illustrated in Figure 5.13. Apex moment was captured by the original Three Spring Model to within 1% of the experimentally seen moment. The modified Three Spring Model over-predicted the experimental apex moment by 6% and

the Existing Model under-predicted the apex moment by 8%. The Existing Model calculates the smallest negative peak shoulder moment at 30% of the arc length, the original Three Spring Model predicted a negative moment 17% higher moment than the Existing Model, and the modified Three Spring Model predicted a moment 40% higher than the Existing Model at that point.

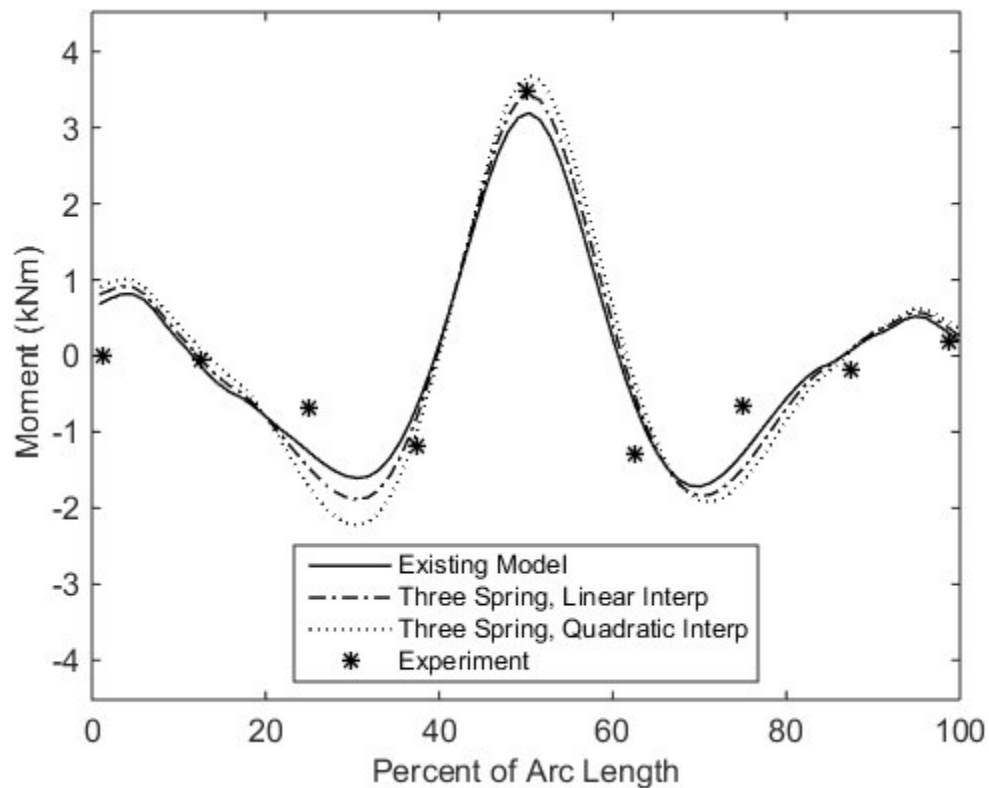


Figure 5.13 Short Arch Apex Service Load Moment, Three Spring Model Comparison

Figure 5.14 illustrates the vertical displacement for the short arch due to apex service loading. For the short arch the Three Spring Model predicted the apex displacement within 2%, and the Existing Model was within 5%. The angled spring models over-predicted the displacement at the apex by 6% for the Radial Spring Model and 37% for the Friction Angle Spring Model.

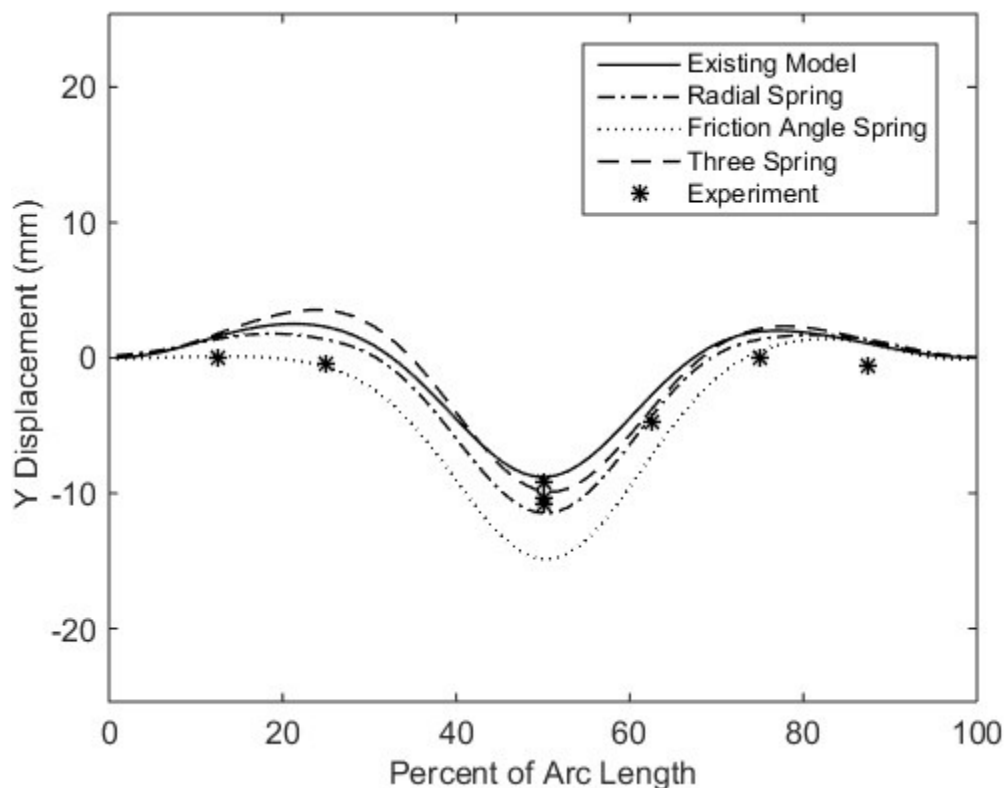


Figure 5.14 Short Arch Apex Service Load Vertical Displacement

5.5.2. 20% Offset Service Live Load

Moments along the span due to an offset service load 20% of the distance between the apex and the left footing are shown in Figure 5.15. The Three Spring Model was unable to converge to a solution for this and the following offset load cases and were omitted from these discussions. For the short arch, the peak moment was predicted within 2.5% by each model. Shoulder moments at 25% of the span were well predicted by each model within 9% of experimental results. The right footing moment was captured by each model within 0.3 kN·m. Since the moment was small, a percentage difference would inadequately demonstrate the comparison. On the left side, the footing moment was over-predicted by all models, but best captured by the Radial Spring Model within 0.2 kN·m.

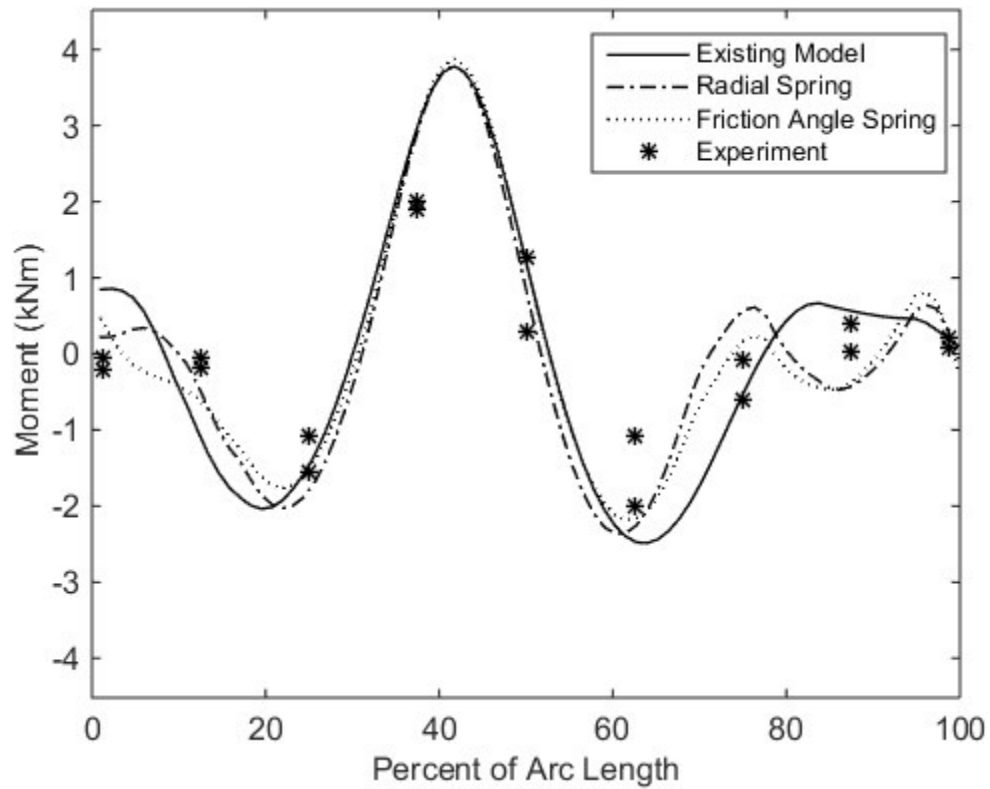


Figure 5.15 Short Arch 20% Offset Service Load Moments

Vertical displacement for each model due to a 20% offset service load can be seen in Figure 5.16. The maximum short arch displacements predicted by the Existing and Radial Spring Model agreed with each other well and was predicted to be 28% higher by the Friction Angle Spring Model.

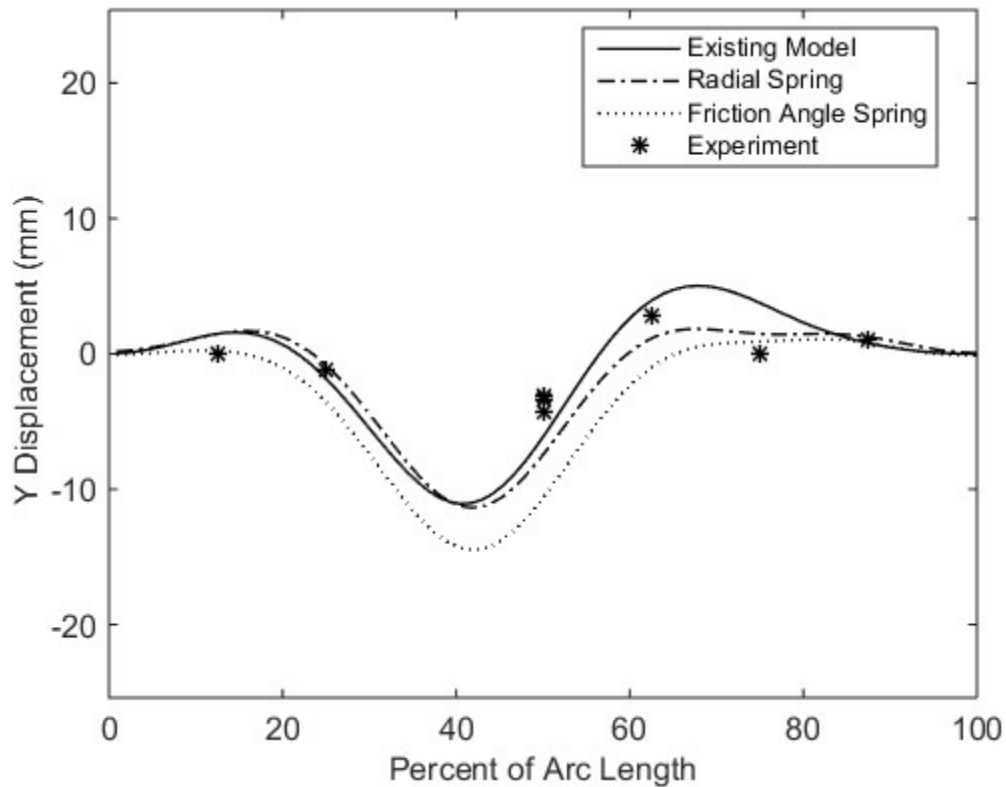


Figure 5.16 Short Arch 20% Offset Service Load Vertical Displacement

5.5.3. 40% Offset Service Live Load

Figure 5.17 illustrates the moment distribution due an offset service load 40% of the distance between the apex and the foundation. The angled spring models predicted an overall lower moment along the span of the short arch and matches with more of the critical experimental values than the Existing Model. The peak moment to the left of the apex was captured within 2.5% of the measured moment while the Existing Model over-predicted the moment by 27%. The negative moment peak to the right of the apex was over-predicted by the Existing Model by double while both angled spring models were within 1% of the moment at that point. Both footing moments were better predicted by the angled spring models while the Existing Model predicted more negative moment than seen experimentally.

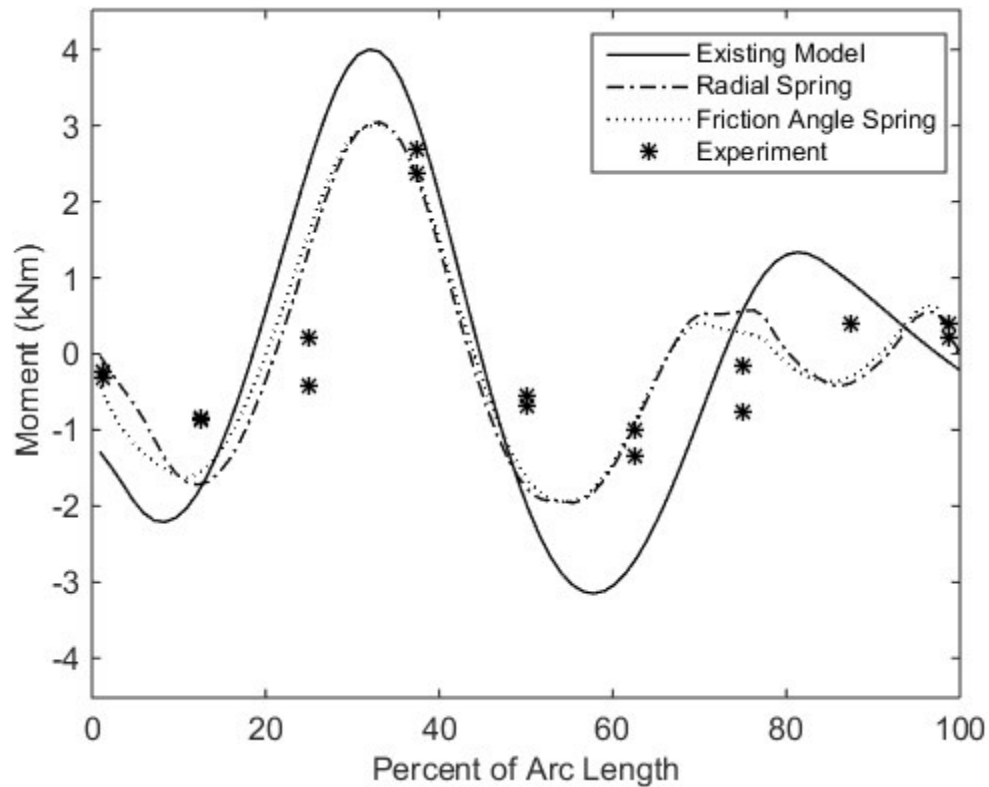


Figure 5.17 Short Arch 40% Offset Service Load Moments

Vertical displacement response for the 40% offset service load is illustrated in Figure 5.18. The Existing Model predicted 23% more movement at the left shoulder than the Radial Spring Model and 46% movement than the Friction Angle Spring Model. The Existing Model predicted more than double the vertical displacement into the soil on the opposite shoulder than the other models and experimental value. The angled spring models predicted less displacement into the soil on the side of the arch opposite the load application, at about 60% of the arc length, than seen experimentally, 36% for the Radial Spring Model and 67% less for the Friction Angle Spring Model.

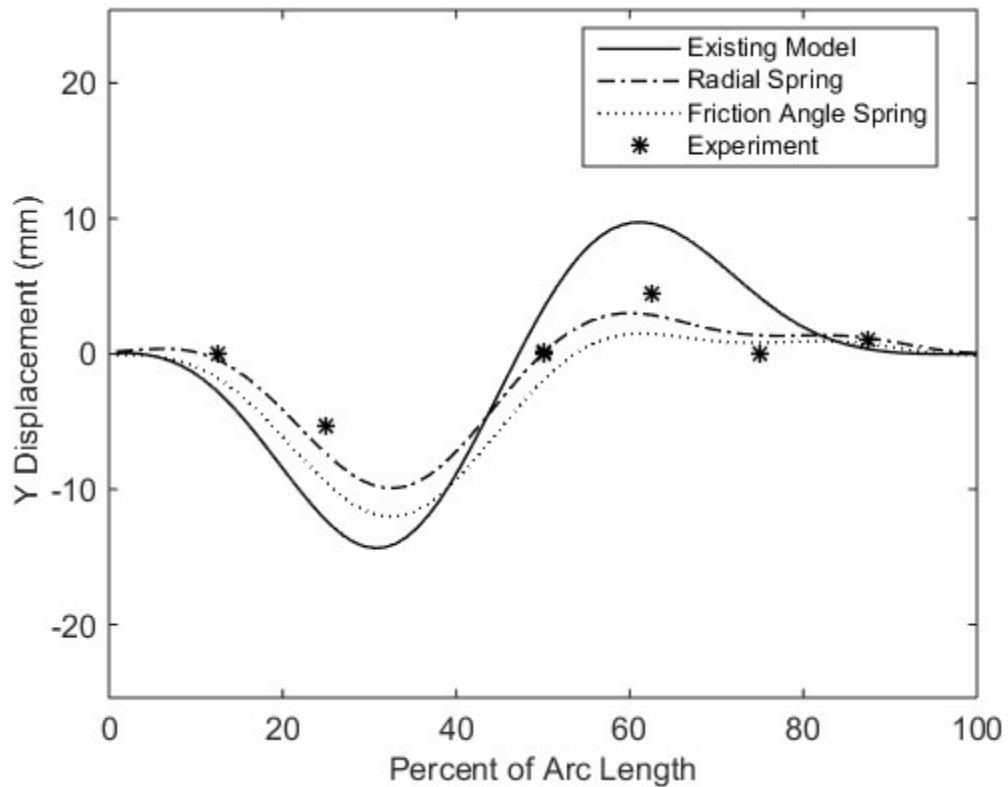


Figure 5.18 Short Arch 40% Offset Service Load Vertical Displacement

5.5.4. 60% Offset Service Live Load

Figure 5.19 illustrates the moment distribution along the span for a 60% offset service load. The peak positive experimental moment was over-predicted by the Existing Model by 25% while the angled spring model predictions were enveloped by the moments seen experimentally. Apex moments for the angled spring models also matched well with experimentally seen moments, while being over-predicted by the Existing Model by 1-1.5 kN·m. Footing moments were generally better predicted by the angled spring models. The left footing moment seen experimentally was over-predicted by all models, 120% greater by the Radial Spring Model, 160% greater by the Friction Angle Spring Model, and 300% greater by the Existing Model. The angled spring models

predicted lower moments at the apex and the shoulder on the side of the arch opposite the load compared to the Existing Model.

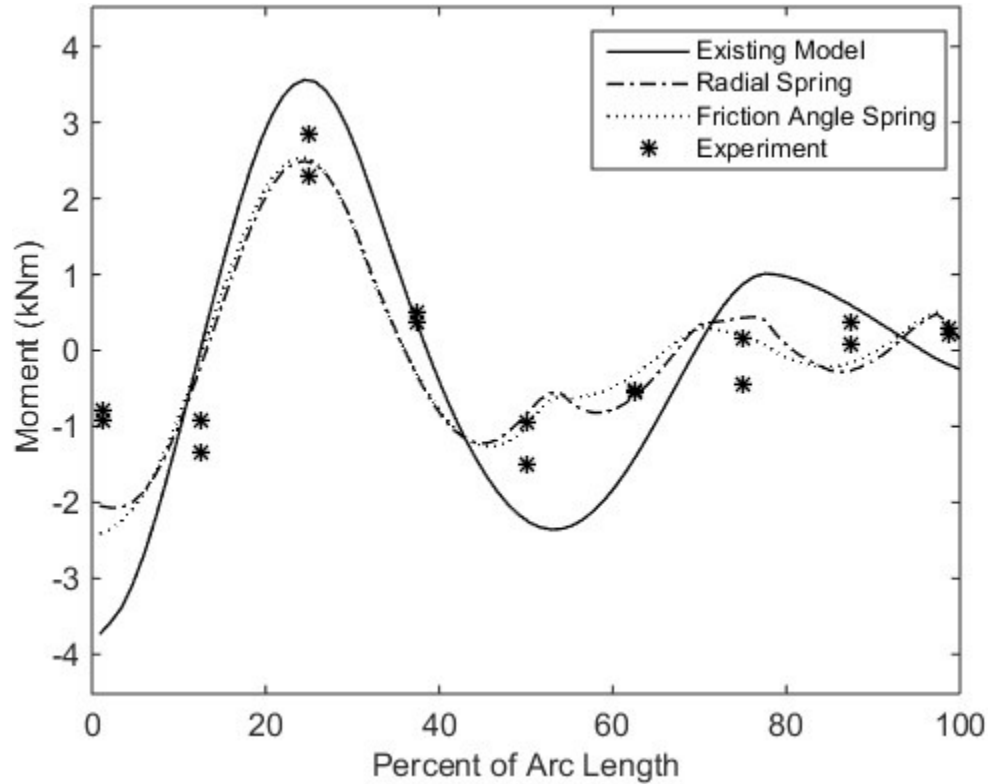


Figure 5.19 Short Arch 60% Offset Service Load Moments

Vertical displacements, seen in Figure 5.20, for the short and tall arches show the arch displacement due to the 60% offset load. Short arch displacements matched with the angled spring models better at most points. The Existing Model significantly over-predicted the downward displacement at the point of the load and the upward displacement into the soil to the right of the apex.

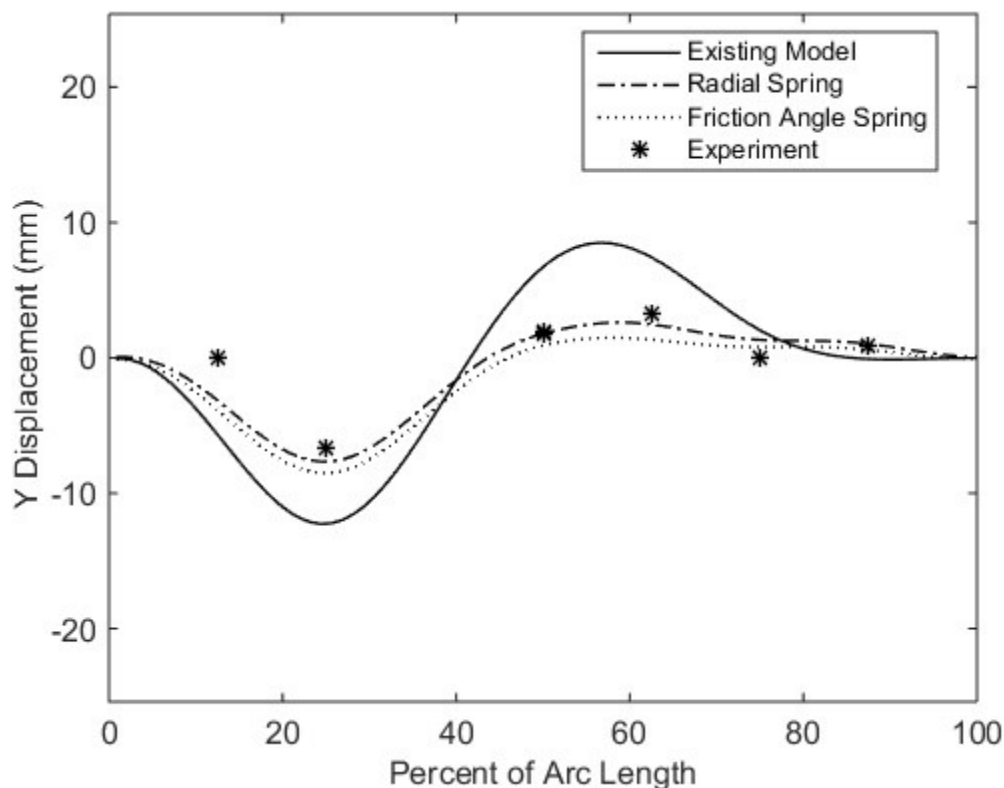


Figure 5.20 Short Arch 60% Offset Service Load Vertical Displacement

Error for each model was calculated as the ratio of the two-norm of the difference in moment seen experimentally and the model results over the two-norm of the vector of experimental moments at the locations of the gauges along the span. The ratios are presented as percentages in Table 5.1 for each model and each load case. ‘NA’ marks the load cases for which the model did not find a solution. The error was used to evaluate each model’s relative performance.

At the end of backfilling the Existing Model performed the best with the smallest error of 46.6%, both Three Spring Model iterations followed closely with less than 2% additional error. The Radial Spring Model predicted the smallest error during the apex service load case, less than half the error calculated by the second best performing model, the Friction Angle Spring Model. The Radial Spring Model also predicted the smallest

error during the 60% offset service load case with an error of 64.2% followed by the Friction Angle Spring Model with 70.9%. For the remaining offset service load locations of 20% and 40% the Friction Angle Spring Model resulted in the lowest error followed within 3% by the Radial Spring Model.

Table 5.1 Error of Each Model Moment Results, Short Arch

	Existing	Radial	Friction	Three Spring (linear)	Three Spring (quadratic)
Backfilling	46.6%	52.6%	62.3%	47.4%	48.4%
Service Apex	37.9%	17.1%	34.4%	43.4%	51.1%
Service 60% Offset	117.4%	64.2%	70.9%	NA	NA
Service 40% Offset	129.4%	86.7%	83.8%	NA	NA
Service 20% Offset	75.0%	65.8%	62.8%	NA	NA

While the model alternatives showed improvement over the Existing Model during service load cases, a single model did not stand out clearly as the best option. For the short arch configuration, the Radial Spring Model had the lowest average error for each load case, with an average error of 57.3%. The Friction Angle Spring Model followed with an average error of 62.8%. The average error shown here tends to illustrate how the models performed for the service load cases since the service load cases outnumber backfilling in this analysis. Since the error was shown as a magnitude, over- and under-prediction appears the same.

5.6. Live Load Response of the Tall Arch

The following sections compared the moment and vertical displacement response due to just the live service load at the apex and offset load locations similarly to the previous section.

5.6.1. Apex Service Live Load

Apex service live load results are shown in Figure 5.21. The apex moment was well predicted by the Existing Model within 5% of the experimental value and was over-predicted by 15% by the modified Three Spring Model. The maximum measured shoulder moment due to apex loading was over-predicted by the Radial Spring Model by 28% and under-predicted by the Existing and Friction Angle Spring Model by 42% and 60% when compared to the experiment. As with the short arch, the footing moments on the right side due to an apex load were generally captured well by each model. The footing moment on the left side was over-predicted again by the Existing Model and captured within 2% by the Radial Spring Model. The experimentally seen moment to the left of the apex was better predicted by the Three Spring Model, under-predicting the moment by 10%.

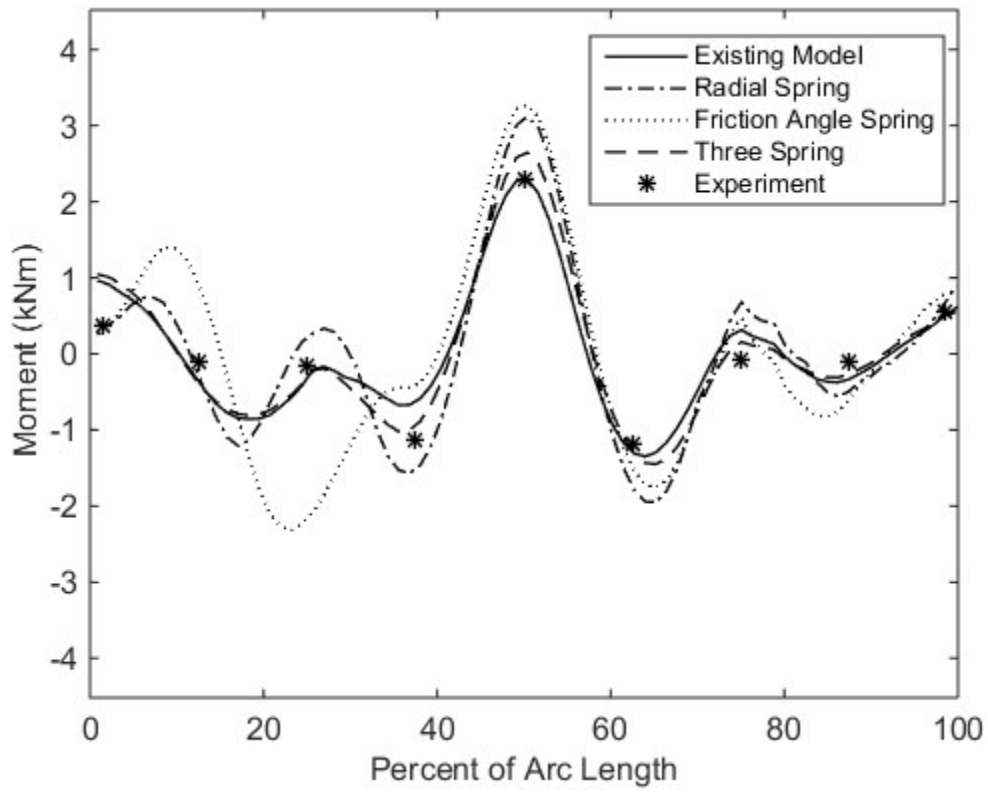


Figure 5.21 Tall Arch Apex Service Load Moments

Figure 5.22 illustrates the vertical displacement for the tall arch due to apex service loading. The models followed a similar trend in the deformed shape. Each model over-predicted the apex displacement compared to the measured value. The Friction Angle Spring Model predicted a negative peak at 25% of the span not seen in the other models.

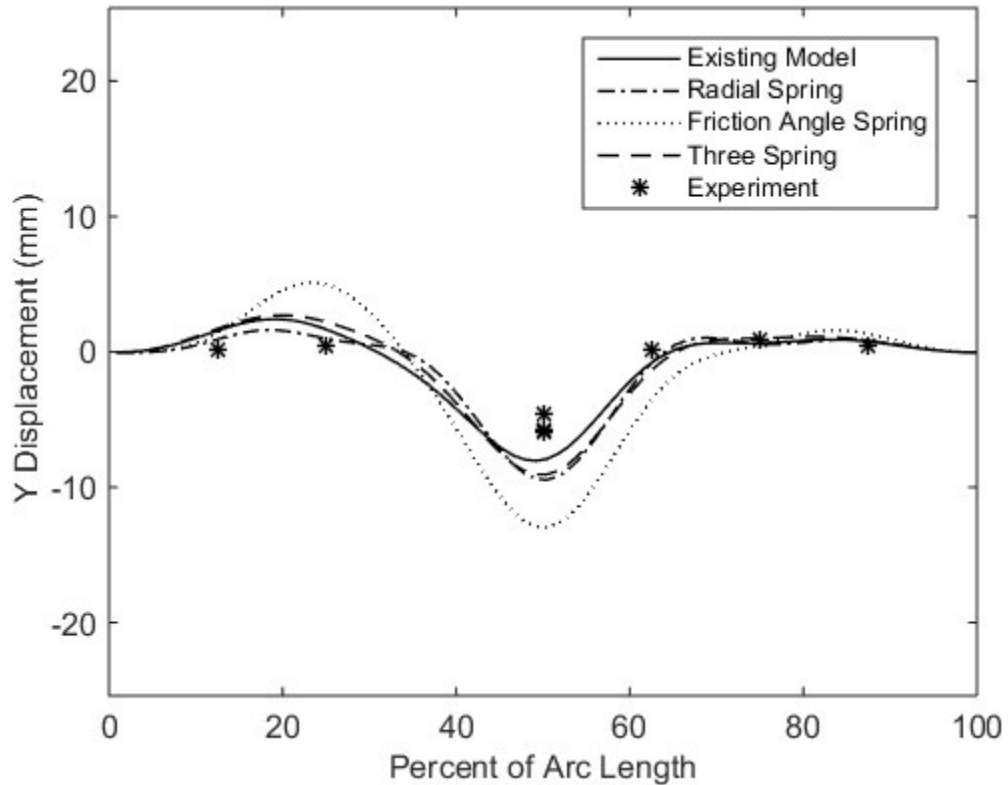


Figure 5.22 Tall Arch Apex Service Load Vertical Displacement

5.6.2. 20% Service Offset Live Load

Moments along the span due to an offset service load 20% of the distance between the apex and the left footing are shown in Figure 5.23. Predicted moment distributions by each model indicate a peak to the left of the apex that was not captured by the gauge configuration. However, model predictions of peak moment vary by nearly 20%. Peaks in moment near the right shoulder was over-predicted by each model but due to the peaks not lining up with the experimental data, it was unknown which model better predicted the maximum negative moment. The Three Spring Model calculated the highest peak in moment to the left of the apex 32% higher than the Existing Model.

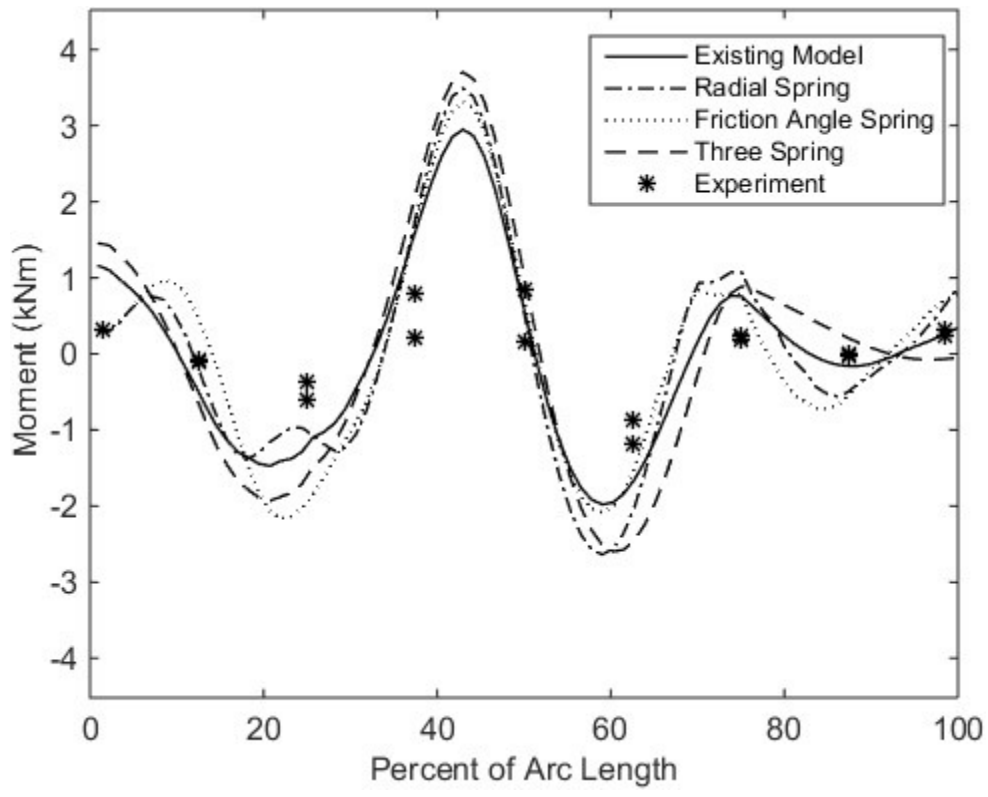


Figure 5.23 Tall Arch 20% Offset Service Load Moments

Vertical displacement for each model due to a 20% offset service load can be seen in Figure 5.24. The tall arch maximum predicted displacements by each model within 4% of each other near 40% of the arch span. The models did not agree with the magnitude of the displacement between the apex and the shoulder opposite the load.

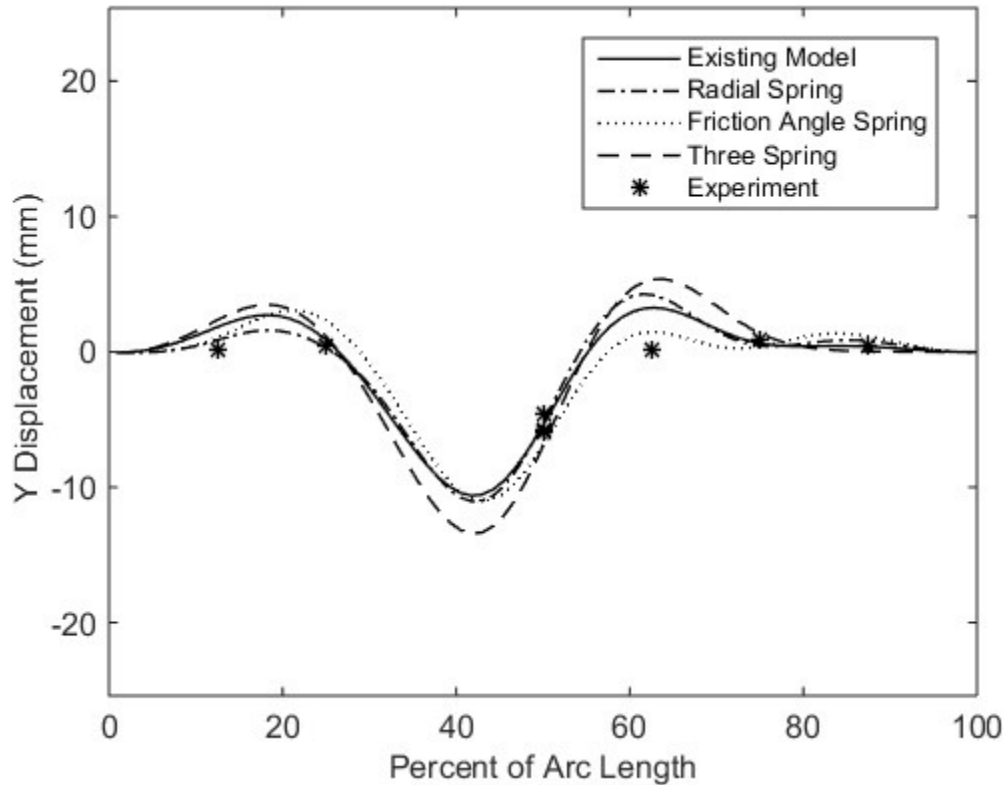


Figure 5.24 Tall Arch 20% Offset Service Load Vertical Displacements

5.6.3. 40% Service Offset Live Load

Figure 5.25 illustrates the moment distribution due a 40% offset service load. The tall arch response shows that the Existing and Friction Angle Spring Models predictions fell between the two peak positive moments derived from the experiment while the Radial Spring and Three Spring Model over-predicted this peak moment by 24% and 13%, respectively. The Radial Spring Model predicted a higher moment at the apex than was measured. The left footing moments were better predicted by the angled spring models and over-predicted by the Existing Model while the opposite was true for the right footing moment.

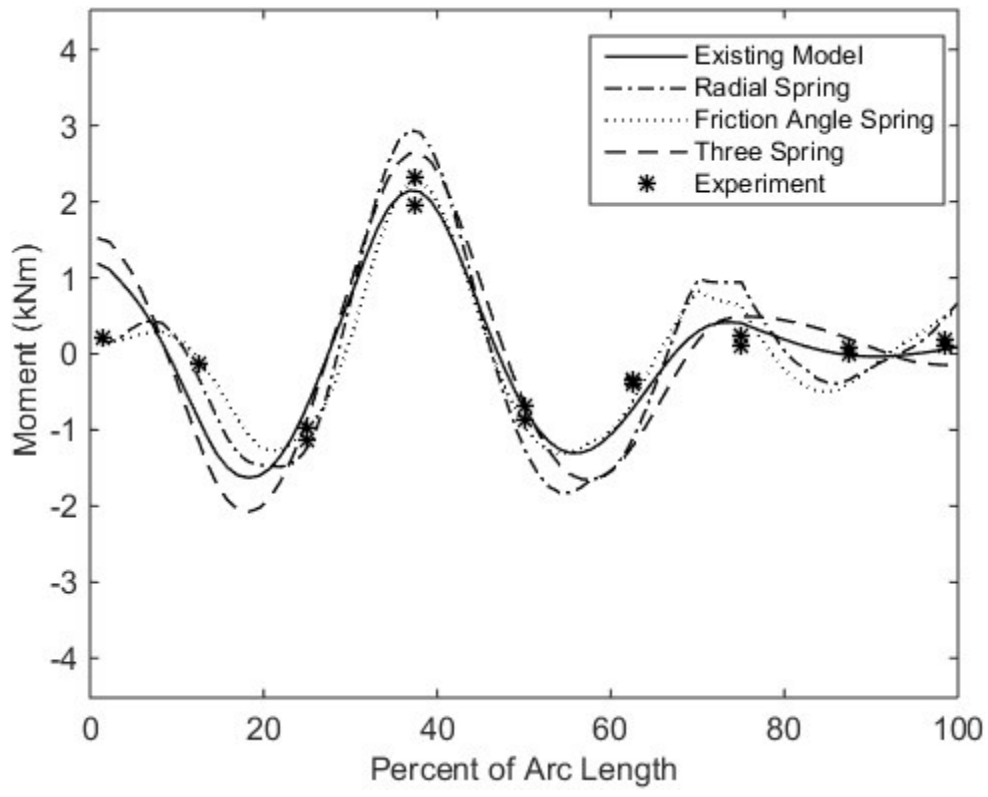


Figure 5.25 Tall Arch 40% Offset Service Load Moments

Vertical displacement response for the 40% offset service load is illustrated in Figure 5.26. The tall arch was generally predicted to have less vertical displacement than the short arch. Experimental values were small and gauges were not present at the peaks so an adequate analysis of the performance of the spring models was difficult.

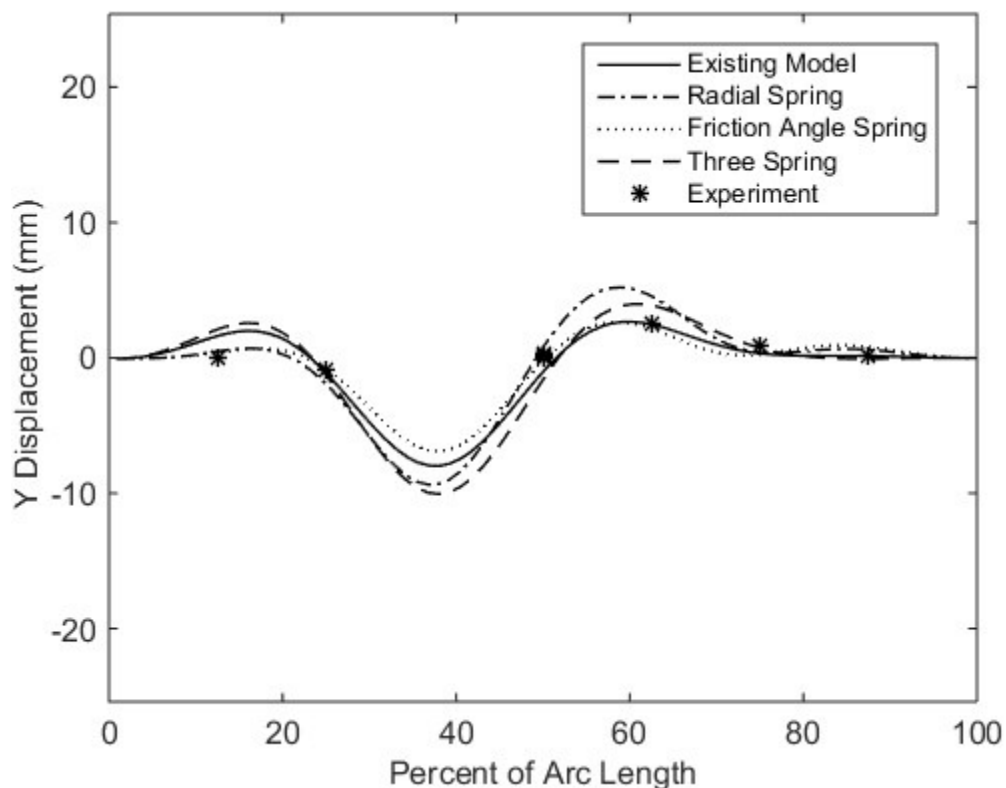


Figure 5.26 Tall Arch 40% Offset Service Load Vertical Displacements

5.6.4. 60% Service Offset Live Load

Figure 5.27 illustrates the moment distribution along the span for a 60% offset service load. For the tall arch, the peak moments appear in different locations along the span for each model. The angled spring models predicted a peak close to 35% of the span from the left support while the Existing Model predicted the peak to be closer to 25% of the span from the left support. The left footing experimentally had a small moment which was captured by the angled spring models, and the Existing and Three Spring Model over-predicted the left footing experimental moment by approximately 0.5-1 kN·m.

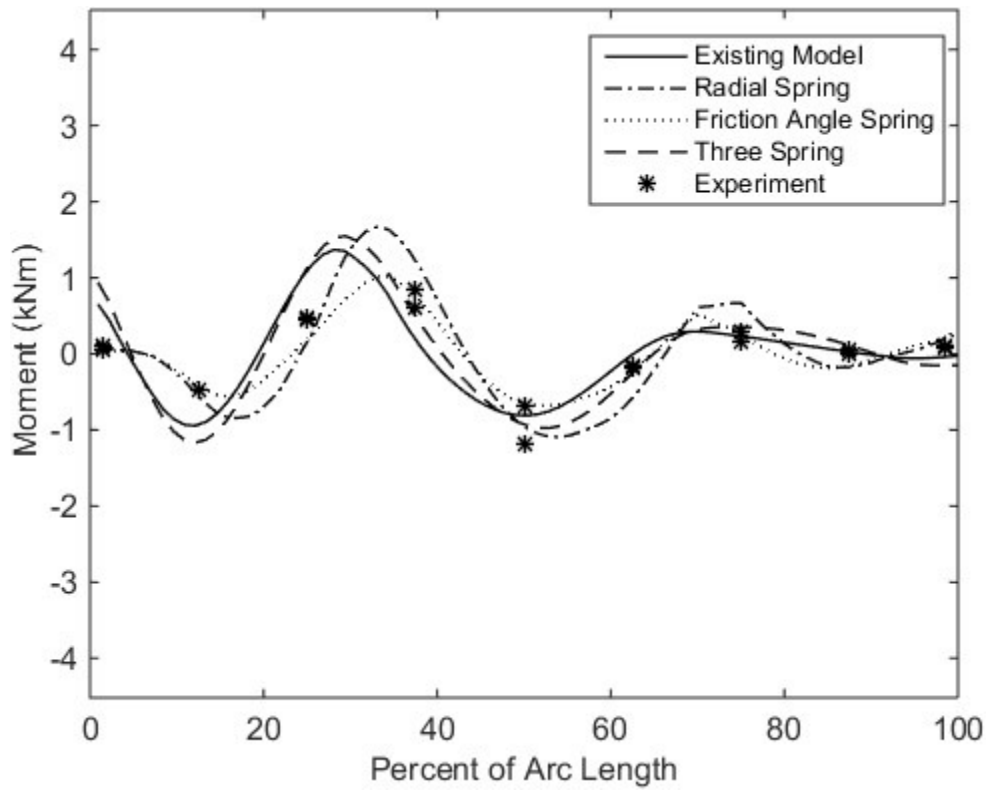


Figure 5.27 Tall Arch 60% Offset Service Load Moments

Tall arch displacements were smaller than the short arch, seen in Figure 5.28. The Friction Angle Spring Model predicted a peak less than 5% smaller than the measured maximum displacement. The Radial Spring and Existing Models over-predicted the vertical displacement by 110% and 56%, respectively.

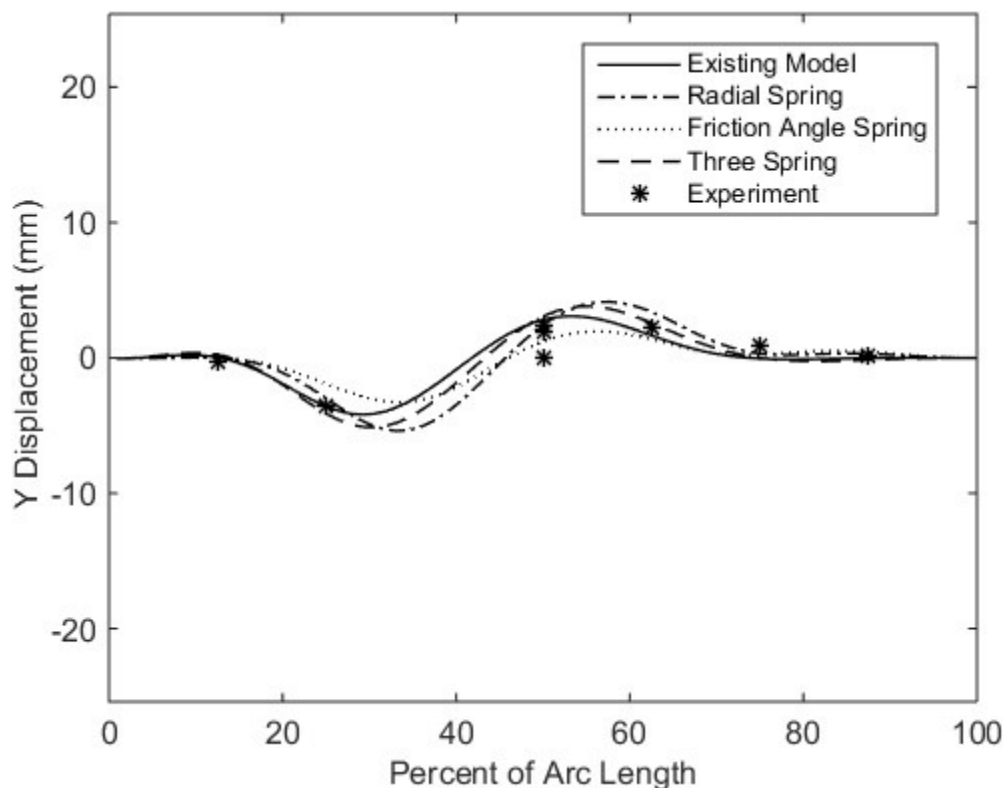


Figure 5.28 Tall Arch 60% Offset Service Load Vertical Displacements

Error for each model was calculated as the ratio of the two-norm of the difference in moment seen experimentally and the model results over the two-norm of the vector of experimental moments at the locations of the gauges along the span. The percent error is presented in Table 5.2 for each model and each load case. The error is used to quantify each model's relative performance. At the end of backfilling, all models calculated a similar error within 7% of each other; the best performing model was the Existing Model with a calculated error of 51.3%. The Three Spring Model calculated the lowest error during an apex service load of 32%, close to the Existing Model's 34.2%. Offset service load response at 60% and 40% was best predicted by the Friction Angle Spring Model at over 30% error, nearly half of the next best model for either load case. All models during

a 20% offset service load calculated an error higher than that of the Existing Model (138%).

Table 5.2 Error of Each Model Moment Results, Tall Arch

	Existing	Radial	Friction	Three Spring (linear)	Three Spring (quadratic)
Backfilling	51.3%	53.3%	55.9%	NA	58.5%
Service Apex	34.6%	52.2%	87.7%	NA	32.0%
Service 60% Offset	87.3%	58.2%	30.1%	NA	100.7%
Service 40% Offset	58.9%	62.8%	33.3%	NA	84.2%
Service 20% Offset	138.0%	159.4%	157.9%	NA	211.1%

As with the short arch models, there was no clear model that best predicts the response of the experiment for all load cases. This error was shown as a magnitude and does not discriminate between over- and under-prediction along the span. The Friction Angle Spring Model calculated the lowest average error for all load cases with an average error of 73%. However, the Existing Model and Radial Spring Models followed close behind with errors of 74% and 77%, respectively. The alternative models for the tall arch did not show much improvement over if any for the analysis as a whole. The Existing Model still predicted backfilling and apex service load response better than the angled spring models and fell behind the Radial and Friction Angle Spring Models for the controlling service load applied at a 60% offset from the apex.

5.7. Ultimate Load Response

The short and tall arch apex moment during ultimate load analysis is shown in Figure 5.29 and Figure 5.30. The total apex moment was presented, which included the effect of backfilling and applied live load. It should be noted that in a real arch the soil stresses can be expected to redistribute when the arch experiences excessive deformations

such as during an ultimate load test; however, the simulations here assume a Boussinesq distribution model and do not redistribute the effect of the live load due to arch deformations. A continuum model Walton et al. (2015 b,c) was able to capture the redistribution in soil stress, however the results from that analysis are not presented here.

The short arch experimentally was able to resist an apex load of 218.8 kN. The Existing Model predicted a maximum load of 215.2 kN, the Radial Spring Model predicted 213.5 kN, the Friction Spring Model predicted 145.1 kN, and the Three Spring Model predicted 187.7 kN. The Existing Model tracks the experimental data starting at about 84 kN, the magnitude of the last service level test. The Existing and Radial Spring Models predicted the ultimate load capacity within 1.6% and 2.5%, respectively. The Three Spring Model under-predicted the capacity by 14% and the Friction Angle Spring Model under-predicted the capacity by 34%. All models predicted a lower moment at the apex at failure than measure experimentally.

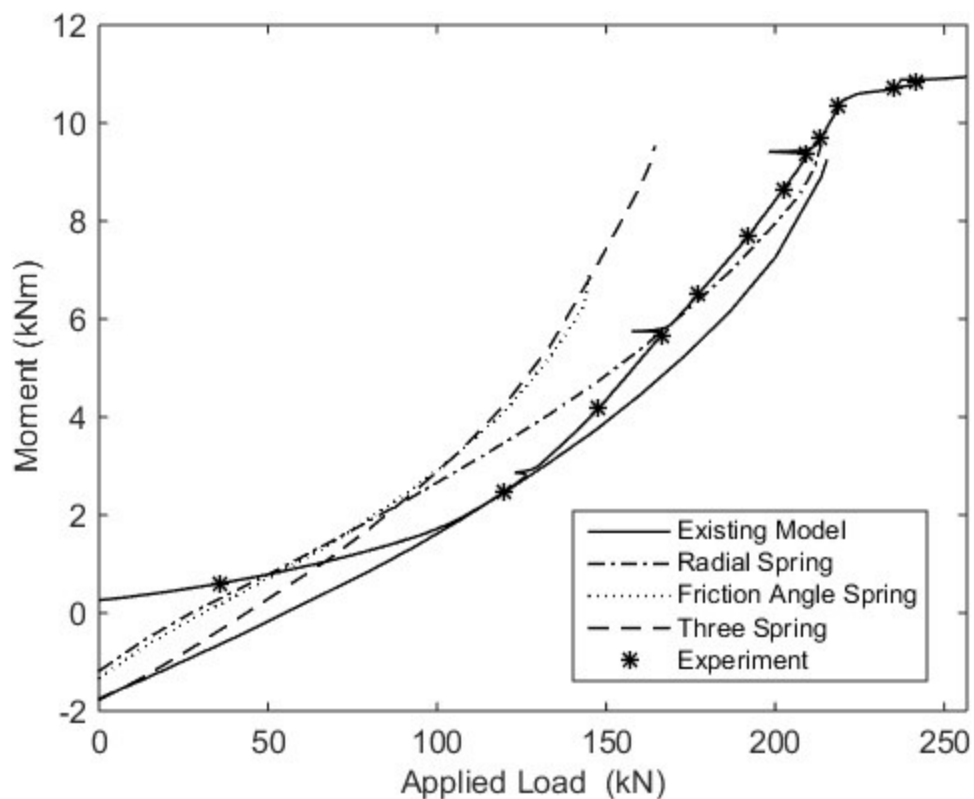


Figure 5.29 Short Arch Ultimate Load Moments

The tall arch model was experimentally seen to withstand 225 kN before failure. The Existing Model followed the experimental response well after an applied load of around 84 kN, similar to the short arch results. This was the point where the load on the soil is exceeding the previous applied service loads and was entering virgin compression. The Existing Model continued to predict the experimental results until about 205 kN then loses capacity until a predicted failure at 202.5 kN, 10% less than that observed experimentally. The Radial Spring Model predicted smaller moments in the apex during ultimate load analysis and experiences failure at 203.5 kN, just under 10% less than the experiment. The Friction Angle Spring Model, similarly to the Radial Spring Model, predicted a lower moment at the apex, and starts to experience a failure earlier at 177 kN,

22% less than seen experimentally. The Three Spring Model over-predicted the capacity of the arch system and predicted failure at 251 kN.

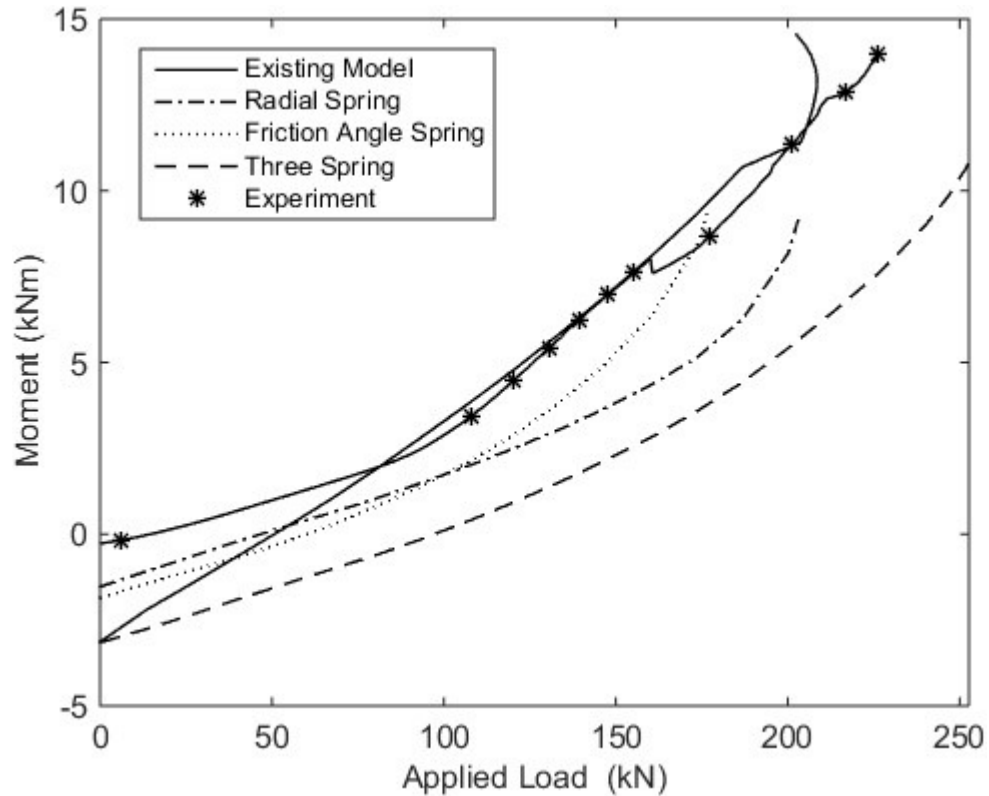


Figure 5.30 Tall Arch Ultimate load Moments

For both arch geometries at the beginning of the ultimate load analysis, the Existing Model predicted a negative moment at the apex of the short arch compared to the experimentally seen moment. As the applied load increases to the magnitude of the previously applied apex service load of roughly 84 kN, the Existing Model and experimental arch responses converge and track well together until failure. This point signifies the change of the experimental soil experiencing pre-consolidation loading to virgin compression.

5.8. Conclusions

This chapter contains a detailed comparison between the Existing Model and the different variations of soil-spring models discussed in the previous chapter for an arch subjected to backfill, service, and ultimate loadings. The structural material used in the arch models was steel taking into account experimentally-determined stress-strain behavior. The models incorporated large deformation, nonlinear soil-spring elements, a Boussinesq live load distribution, and improved foundation elements. Notable conclusions are summarized below:

- The angled spring models show promise as they better capture moments and displacements caused by offset loads.
- The Existing Model better predicted the ultimate load analysis than other models.
- The Existing Model best predicted the end of backfill moments at the apex and shoulder, followed by the Three Spring Model
- The angled spring models generally predicted the footing moments better than the Existing model.
- The Three Spring Model was unable to converge for offset load cases and backfill in the tall arch.
- While angled spring models were able to capture the vertical restraint offered by the soil, they do not incorporate a failure criterion, i.e. the soil-springs do not have a limit to the amount of force they can apply to the arch. This could be an issue near the shoulders and apex of the models as the soil cover above the nodes is small.

CHAPTER 6

CONCLUSIONS

6.1. Summary and Conclusions

The objectives of this research were to develop user-friendly prototype analysis software to analyze buried arch structures and to improve the model predictions of internal arch moments with respect to experimentally gathered results during backfill, service, and ultimate loading. The Existing Model used for analysis incorporated nonlinear, overburden-dependent springs to represent the soil restraint of the arch. The Existing Model was intended as a research tool and was not user-friendly, relying on text based input and generating text output files. *CBAS Design* was developed as prototype software to generate and analyze buried arch structures under backfilling and surface loading within an intuitive user interface. Prior simulation results compared well with experimental testing for dead load and apex live load cases but need improvement for offset load cases which can control design in certain geometries. This research investigated two aspects of the soil-spring model that warrant improvement: live load distribution through the soil and the soil-spring orientation.

Chapter 2 described the typical soil modeling methods, live load distribution, and prior research on buried arch bridges. Different aspects of the experimental program and the model simulation developed by Walton et al. (2015 a,b) were addressed in detail. Walton et al. (2015 a) constructed scale models using two arch geometries, where the structure was placed in a self-reacting soil box, and subjected to staged backfilling, service live load, and ultimate apex load. Walton et al. (2015 b) improved a model

initially developed by Clapp and Davids (2011) to simulate the arch response using beam elements for the arch and nonlinear springs to represent the soil.

Chapter 3 described the prototype software entitled *CBAS Design* that models the buried arch structures as a 2-D finite element model. *CBAS Design* incorporated an intuitive environment that can be used to generate different arch models with a variety of material and soil parameters as well as review the results of the analysis. The effect of small versus large deformation was treated and a mesh refinement study was conducted. Parametric studies examined the sensitivity of the model to different soil parameters and lift heights. *CBAS Design* is a tool that can be used to efficiently analyze a variety of buried arch bridges in a user-friendly interface using a simplification of the Existing Model.

Chapter 4 addressed two areas of the Existing Model that warrant improvement, the live load distribution and the orientation of the soil-springs. Currently, a Boussinesq load distribution is used to calculate the effect of live loads on the arch. The Boussinesq distribution model was compared to a SSI continuum FE model and the experimental data on soil pressure near the arch for both the short and tall arches tested by Walton et al. (2015 b). The comparisons show that the experimental pressures along the span are poorly captured by the Boussinesq model away from the point of the load for all load cases. The SSI model results showed a different pressure distribution along the arch, distributing pressures away from the point of load application for offset load cases. The vertical load distribution along the span seen experimentally gives insight on the actual vertical pressures the arch system experienced during testing. More pressure gauges

would have improved resolution of the load distribution and allowed better assessment the effectiveness of the Boussinesq model for calculating soil stresses.

Three soil-spring orientation alternatives were implemented with the intent of improving the soil-spring model's ability to predict experimental data. The Radial Spring Model, Friction Angle Spring Model, and Three Spring Model were examined with respect to ease of implementation and advantages over the Existing Model. Each alternative soil-spring model incorporated vertical soil restraint to the arch during the different load cases. In addition, the Three Spring Model also added friction to the model by adopting the Coulomb soil model for active and passive soils.

Chapter 5 examined comparisons between the alternative soil-spring models, the Existing Model, and experimental results throughout backfilling and due to service live and ultimate loadings. The Existing and Three Spring Model predicted the backfilling and apex service load response more accurately than the angled spring models. The angled spring models showed improvement in calculating the offset load response measured experimentally than the Existing Model. The Three Spring Model was only able to converge to a solution during backfill and apex loading for the short arch, and only converged through partial backfilling of the tall arch. Modifications were made to the soil-spring interpolation routine and improved the Three Spring Model convergence only for the tall arch geometry.

While the alternative models showed some improvement over the Existing Model for some load cases, no one model is clearly the best option for all load cases. For the short arch geometry the angled spring models were able to capture the response of the arch as measured by the magnitude of the error of model-predicted arch moments

relative to the experimentally determined moments. By the same measure, the Existing Model and Friction Angle Spring Model performed similarly for the tall arch analyses.

6.2. Future Work

While the changes to the model show some improvement in certain load cases, further improvements in modeling strategies are warranted to better simulate response of buried arch structures under all load cases. The following is a summary of recommendations for future work:

- *Improve the implementation of the Three Spring Model.* The three spring model showed promising results for the short arch under backfilling, but its inability to converge for other load cases and geometries limited its application. Modifications improved model convergence for the tall arch but the Three Spring Model was still unable to find a solution for the short arch geometry. Future research should focus on modifying the implementation of this model to improve its convergence so it can be more thoroughly assessed.
- *Inclusion of failure criteria in the angled soil-springs.* The angled soil-springs are allowed to apply a force on the arch that is dependent on the arch displacement and the weight of soil above the arch. However, this force can potentially exceed the shear strength of the soil and be unrealistically large. A failure criterion that limits the stiffness and capacity of the equivalent soil-springs to account for the strength of the soil at that location should be considered.
- *Optimization of the soil-spring orientation.* The angled soil-springs were oriented radially and at the soil friction angle. Incorporating horizontal soil-springs near the base of the arch and radial or friction angle springs near the shoulder to

account for the arch movement into and out of the soil may improve model predictions.

- *Improve live load distribution models.* The current live load distribution assumes an infinite soil with uniform soil properties. The ideal load distribution method will incorporate changes in soil properties with depth, the arch itself, and the movement of the arch due to the current and previous loadings. Suggested improvements include a better analytical solution or a coupled soil-continuum - beam model where a soil-continuum model is initially run to give pressures that are then applied to a simplified beam-spring model. Alternatively, Westergaard theory for calculating vertical soil pressures could be investigated. The Westergaard method assumes alternating layers of soft and stiff soils. This allows more lateral spreading of vertical stresses than predicted using Boussinesq theory, which may agree better experimentally measured pressures.
- *Optimizing a constitutive model to solve for ideal soil-parameters.* To create a model that best predicts the response of the experimental arches due to all load cases, an optimization study should be conducted to find the best material and geometric properties as well as soil-spring properties. Optimal soil-spring orientation could be investigated using an inverse problem, where error between the using experimental results and model predictions are used to define error to be minimized.

REFERENCES

- ABAQUS, (2011) 'ABAQUS Documentation', Dassault Systèmes, Providence, RI, USA.
- Barker, R.M., Duncan, J.M., Rojiani, K.B., Ooi, P.S.K., Tan, C.K., Kim, S.G. (1991). "NCHRP 343: *Manuals for the design of bridge foundations*." Transportation Research Board, Washington D.C.
- Bannon, D. (2009). Characterization of concrete-filled fiber reinforced polymer arch members. (Masters thesis, University of Maine, 2009).
- Burgueño, R., Davol, A. (2001) "Flexural Behavior of Circular Concrete Filled FRP Shells." *Journal of Structural Engineering*, 810-817.
- Chen, J. T., Farouz, E., Landers, P. (2010) "Development of project specific p-y curves for drilled shaft retaining wall design." *Earth Retention Conference 3*. 162-169.
- Clapp, J.D. and Davids, W.G. (2011). "Simplified Modeling to Assess Soil-Structure Interaction." AEWG Report No. 11-30.
- Clough, G.W., Duncan, J.M. (1990). "Earth pressures." *Foundation Engineering Handbook*, 2nd ed., editor: Fang H.S., Van Nostrand Reinhold, Norwell MA, 224-235.
- Dagher, H.J., Bannon D.J., Davids, W.G., Lopez-Anido, R.A., Nagy, E., Goslin, K. (2012). "Bending behavior of concrete-filled tubular FRP arches for bridge structures." *Construction and Building Materials*, 37, 432-439.
- Das, B.M. (2011) *Principles of Foundation Engineering*, Cengage Learning, Stamford, Connecticut.
- Faraji, S., Ting, J.M., Crovo, D.S. (2001) "Nonlinear Analysis of Integral Bridges: Finite-Element Model." *Journal of Geotechnical and Geoenvironmental Engineering*, 454-461
- Holtz, R.D., Kovacs, W.D., Sheahan, T.C. (2011) *An Introduction to Geotechnical Engineering*, Prentice Hall, Upper Saddle River, New Jersey.
- MATLAB (2014), MATLAB R2014b 8.4.0.150421, The MathWorks Inc., Natick, Massachusetts.
- NAVFAC (1986), DM 7.02 Foundations and Earth Structures, Naval Facilities Engineering Command, Alexandria, Virginia.
- Petersen, D.L., Nelson, C.R., Li, G., McGrath, T.J., Kitane, Y. (2010). "NCHRP 647: *Recommended design specifications for live load distribution of buried structures*." Transportation Research Board, Washington DC.

- Rani, S., Prashant, A. (2015) "Estimation of the Linear Spring Constant for a Laterally Loaded Monopile Embedded in Nonlinear Soil." *International Journal of Geomechanics*.
- Reese L. C. and Wang S.T. (2006). "Verification of computer program *LPILE* as a valid tool for design of a single pile under lateral loading." www.ensoftinc.com.
- Walton, H.J, Davids, D.G., Landon, M.E., Clapp, J.D. (2015a) "Experimental Evaluation of Buried Arch Bridge Response." Submitted to *ASCE Journal of Bridge Engineering*.
- Walton, H.J, Davids, D.G., Landon, M.E., Clapp, J.D. (2015b) "Simulation of Buried Arch Bridge Response." Submitted to *ASCE Journal of Bridge Engineering*.
- Walton, H.J. (2015c). Behavior of Buried Composite Arch Bridges. (PhD Dissertation, University of Maine, 2015)
- Wang, S., Vasquez, L., Xu, D. (2013) "Application of Soil-Structure Interaction (SSI) in The Analysis of Flexible Retaining Walls." *International Association of Chinese Geotechnical Engineers*

APPENDIX A

USERS MANUAL

UNIVERSITY OF MAINE
Advanced Structures and Composites Center

**SOIL-STRUCTURE INTERACTION
FINITE ELEMENT ANALYSIS OF
COMPOSITE BURIED ARCH
STRUCTURES**

User's Manual and Documentation

Leo Helderman, EI, BS

May 2016

Table of Contents

Introduction and Program Overview	112
Installation and Running CBAS Design	112
Creating and Opening Existing Models	113
Structure Properties.....	115
Load Configuration.....	117
Analysis.....	119
Results.....	120
Comparison to Experimental Results.....	120
Step by Step Example	124
Output Database Description	129
Input File Description	130
References.....	133

Introduction and Program Overview

CBAS Design is a finite element program written in MATLAB (2014) that allows the user to analyze a variety of Composite Buried Arch Structures. The user can analyze the buried arch structures during construction and apply multiple loads at the top of the backfilled soil. *CBAS Design* automatically creates soil-springs for each arch element to capture the confining effect of the soil mass due to self-weight and service loads. After the analysis is complete, *CBAS Design* stores the results and displays the behavior of the composite arch for each step of the analysis. This user's manual outlines the basic functionality of the software and an example.

Installation and Running CBAS Design

CBAS Design is installed by copying the entire CBAS Design folder to any location on the computer hard drive. This folder contains all the files required to run *CBAS Design* including the MATLAB Runtime Installer for different operating systems seen in Figure A.1. The main program is the *CBAS Design.exe* executable file located within this folder. Also in this directory is a folder that includes the moment curvature relationships for the FRP arch members used in this software.

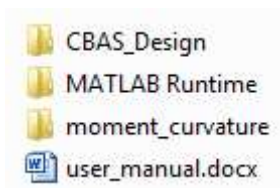


Figure A.1 CBAS Design Directory

After the files have successfully been copied, the first step in installation is to run the MATLAB Runtime Installer for the computer's operating system. As an example, if the computer is running 64-bit Windows the user must install the file labeled *MCR_R2014b_win64_installer.exe* before continuing. This file allows the computer to run the compiled MATLAB program without purchasing a full version of

MATLAB 2014b. If the computer runs a Mac or Linux OS, the zip files labeled `MCR_R2014b_maci64_installer.zip` or `MCR_R2014b_glnxa64_installer.zip` must be extracted and installed, respectively.

Creating and Opening Existing Models

Running `CBAS Design.exe` starts in the structural properties tab with initial default values for each variable in the analysis, shown below in Figure A.2. These should be modified to model the chosen arch configuration. To save a model, click on file in the menu bar and select save as. Enter a name for the model after a prompt is shown. This will save the inputs for the current model in a text input file in the folder labeled `models` in the `CBAS Design` directory. This is the default folder that input files will be automatically stored in for every model. If the model already has been saved in the past, pressing the save button will overwrite the existing model with the updated values.

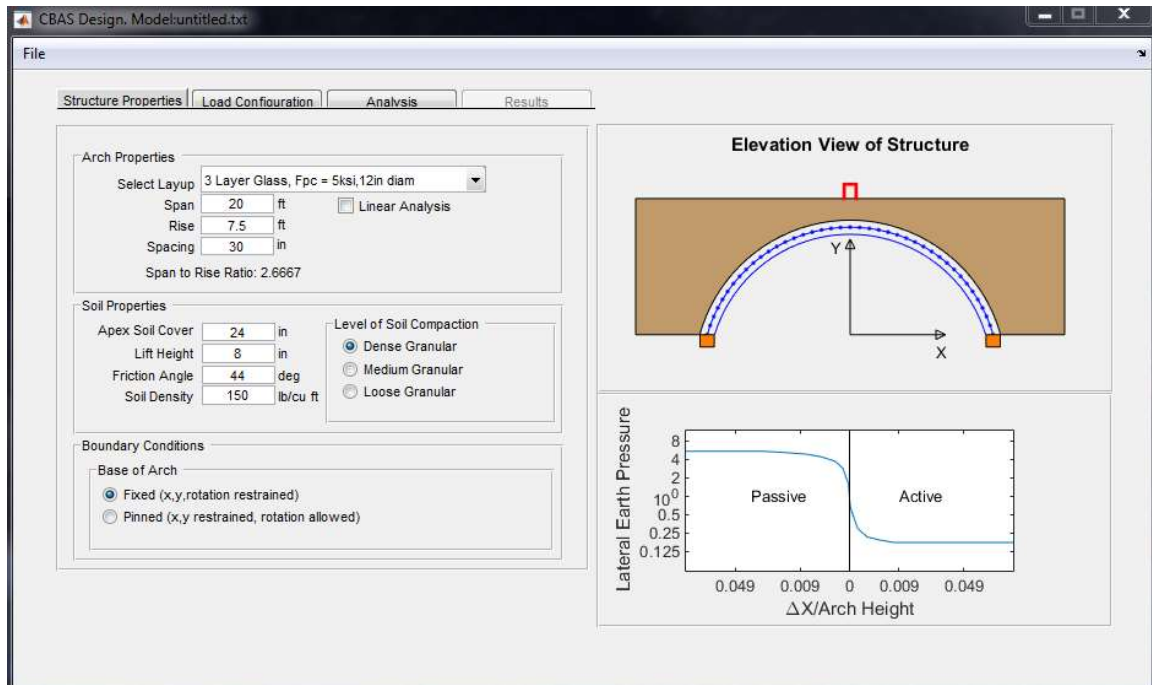


Figure A.2 Initial View of CBAS Design, Structure Properties Tab

To open a model, click on file in the menu bar then select open. The open window will display all models in the models directory mentioned above. Open the desired model and the inputs for that model will be loaded to the software user's interface. The results tab will be accessible if results exist for the model. Otherwise the analysis still needs to be run in the analysis tab first. If results exist and a change is made to any analysis parameter, *CBAS Design* will issue a warning and delete the results for the model to ensure that the results correspond to the correct model.

When an analysis is initialized, an input file for the model is automatically created and saved regardless of when the model was last saved. This guarantees the input file corresponds to the correct output database.

Structure Properties

The first tab in the software is the *Structure Properties* window seen in Figure A.2. Here the type and geometry of the arch, the different soil properties and compaction level, and the boundary conditions are specified.

The *Arch Properties* panel contains all variables that relate to the geometry and material properties of the arch. In the dropdown menu, there are predefined FRP layups with concrete strengths and diameters which are typically used for buried arch structures. The option is also available to conduct a linear analysis, allowing the user to specify an elastic modulus, cross sectional area, and moment of inertia for the arch. The *Soil Properties* panel defines geometry of the soil mass and characteristics of the soil. The *Boundary Conditions* panel defines the behavior of the base of the arch during loading.

Select layup: Using the dropdown menu, select the appropriate layup for the arch to be analyzed. There are two pre-defined layups: 3 layers of longitudinal glass, or 2 layers of longitudinal carbon. For each layup a 5, 6, or 7 ksi concrete compressive strength may be selected. Each layup has the option for a 12 or 15 inch diameter tube. Note that the 12 and 15 inch diameters are nominal values used to describe the size rather than a measure of the true tube diameter. The analysis uses the true diameter for all calculations, which is 11.98 in or 14.98 in for the glass tubes and 11.79 in and 14.83 in for the carbon tubes.

Linear Analysis: If instead of selecting a predefined, nonlinear layup the user wants to conduct a linear analysis of the system, the Linear Analysis checkbox is selected. The analysis will run using an isotropic elastic material with the following parameters.

- *Elastic Modulus*: Elastic modulus of the main members in the arch in ksi.
- *Area*: Cross sectional area of the arch in square inches.
- *Moment of Inertia*: The moment of inertia in the plane of the arch span, in inches⁴.

Span: The span between the centerlines of the two bases of the arch, in feet. The span-to-rise ratio is displayed under this entry, and if the span-to-rise ratio is greater than 6 the text will be in red. Typical arch structures of this type do not exceed a span-to-rise ratio of 6, however the analysis can be performed with such a value. The span is not allowed to exceed 65 feet or be less than 10 feet.

Rise: The height of the arch from the bottom of the arch to the centerline of the apex in feet. A warning will be given if the span-to-rise ratio is greater than 6, however the analysis will be allowed to continue even though this is not a typical configuration currently used in buried FRP arch structures. Due to the span limitation, the rise cannot exceed 32.5 feet.

Spacing: Centerline distance between adjacent arches in inches. The spacing can range from 24 to 120 inches.

Friction Angle: Backfill soil friction angle, in degrees. The friction angle can range from 30° to 55°.

Lift Height: Height of each lift to be applied to alternative sides of the arch, in inches. Lift Height can range from 1 inch to 24 inches.

Apex Soil Cover: Height of soil above the centerline of the arch at the top of the apex, in inches. The sum of Apex Soil Cover and Rise will be total backfill height. Apex Soil Cover can range from 12 inches to 240 inches.

Soil Density: Backfill soil density in pounds per cubic foot. Soil density can range from 75 pounds per cubic foot to 160 pounds per cubic foot.

Level of Soil Compaction: An approximate level of the backfill soil's compaction level, relative to dense, medium, or loose compaction. The accompanying figure shows the coefficient of horizontal pressure versus the lateral movement.

Fixed: Boundary condition at the base of the arch restraining X and Y translation as well as rotation.

Pinned: Boundary condition at the base of the arch restraining X and Y translation, rotation is allowed.

Load Configuration

In the *Load Configuration* tab, the user is able to specify up to 8 rectangular patch loads of varying sizes to simultaneously apply to the structure seen in Figure A.3. This tab can be seen below with the default values. The option to analyze the structure only during backfilling is available, stopping the analysis after backfilling process is complete. Using the dropdown menu select the number of patches to be applied to the structure. To define the patches, the user must specify the magnitude of the force, the location of the center of the rectangular patch, and the dimensions of the patch. The location is needed with respect to the coordinate system used in defining the arch nodes. The default location of the first patch is at (0,0) any additional patches are offset to prevent initial overlap. The first value is the x-location of the patch parallel to the span with zero at the apex seen in the "Elevation View of Structure" image in Figure A.3. The second value is the out of plane z-position of the patch transverse to the arch span with zero directly above the centerline of the arch seen in "Plan View of Applied Loads" in Figure A.3.

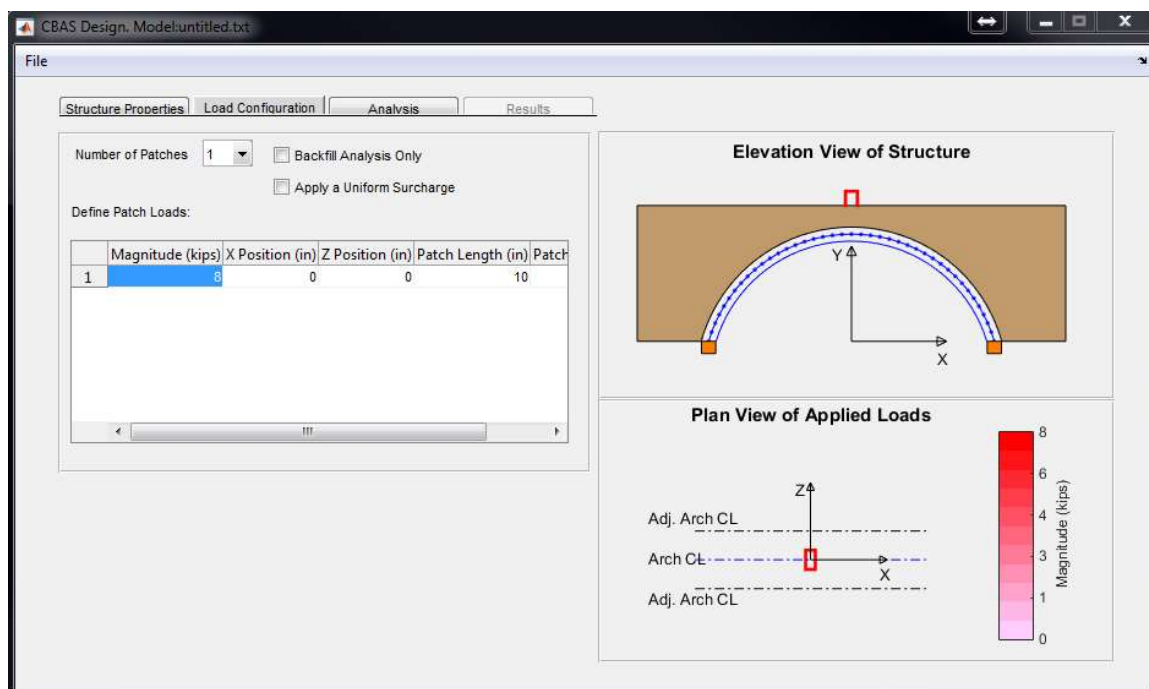


Figure A.3 Load Configuration Tab

Patch length and width are defined by the dimension of the patch parallel to the arch span and transversely, respectively. All dimensions are in inches.

Number of Patches: Up to 8 patches can be applied at once to the arch.

Backfill Analysis Only: To simulate just the backfilling process, select this checkbox. The model will halt after the backfill analysis is complete without applying any additional loads defined in this tab.

Apply a Uniform Surcharge: In addition to applying patch loads, it is possible to apply a uniform surcharge pressure over the entire structure. Enter a value in units of pounds per square foot greater than zero. Any patch loads will still be applied at the elevation of soil specified as the apex soil cover. This requires the user to specify a patch to be applied simultaneously with the surcharge.

Define Patch Loads: Eight loads can be simultaneously applied to the structure with varying magnitudes, locations, and sizes. The magnitude is in kips, locations and

dimensions in inches. The x position is the distance from the center of the span. The z position is the out of plane distance from the centerline of the arch. The length is the patch dimension parallel to the length of the arch. The width is the patch dimension transverse to the length.

Analysis

In the *Analysis* tab, shown in Figure A.4, the user can select the *Large Deformation Analysis* option, change the number of elements in the arch, and run the analysis. When running the analysis, a status bar will pop up and the figure will update with the backfilling sequence showing the model's progress.

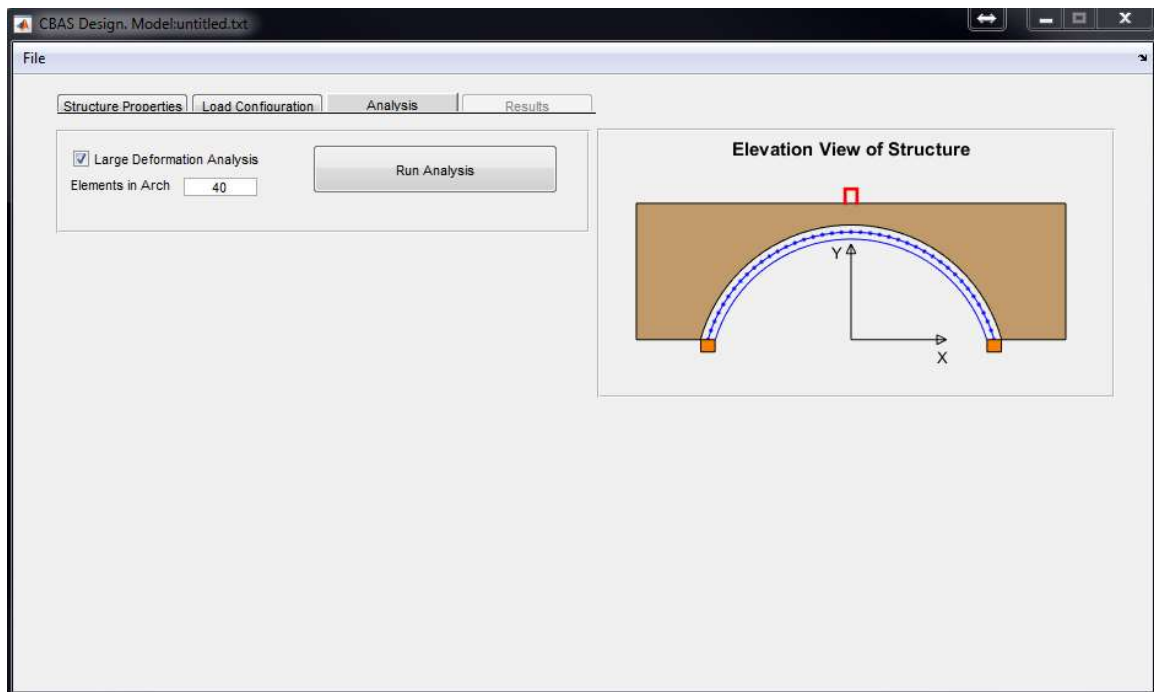


Figure A.4 Analysis Tab

Large Deformation Analysis: The analysis will update nodal positions and allow the arch to deform past the limits of a small deformation analysis, allowing the model to capture the truer arch displacement.

Elements in Arch: Number of equal-length elements in the arch, limited to even numbers greater than 20. An upper limit is 1000 elements, however based on previous studies by Walton et al. (2015 b) there is a 2% change in ultimate load between 40 and 80 elements and a 0.2% change between 80 and 160 elements. Generally, the more elements are used the more accurate the result; however this affects the runtime of the model.

Run Analysis: Once all input parameters are finalized, press this button to start the analysis. If the model has not been saved yet, the user will be prompted to do so.

Results

The *Results* tab allows the user to view the response of the arch for each step in the analysis. Arch moments, shear, and axial member forces can be seen numerically along the span or visually using a color map. The arch deflection can be seen throughout the analysis with a scale magnification factor to fine tune the plot for different displacement levels.

If any properties are changed after a model has run and results exist, *CBAS Design* will erase the output database for the model to ensure that no inconsistencies exist between the defined model and the relevant results.

Comparison to Experimental Results

The following is a comparison of arch moments and vertical deflections between experimental results, previous models, and *CBAS Design*. The experiment was designed and executed at the University of Maine Advanced Structures and Composites Center. The steel arches were set in concrete foundations that were supported by a low-friction surface. The foundations were allowed to rotate during the test. Soil was placed in 8 inch lifts on alternating sides of the arch until a crown depth of 24 inches was achieved. The

previous models are research models developed by Walton et al. (2015 b). The research model and *CBAS Design* share many of the same traits as both are finite element analyses using beam elements for the arch and axial springs for the soil pressure. However the research model accounts for the foundation rotation and decking elements. In both models, an at rest lateral earth coefficient (K_o) is 1, which is consistent with compacted soil.

From work from Walton et al. (2015 a,b), the critical design depends on bending moments since Composite Buried Arch Structures are efficient in axial compression and shears are assumed small due to the small span to depth ratio. The critical locations are at the footings, apex, and the shoulders. At these locations, the critical design load cases are found to be positive moment at the shoulders and negative footing moment during backfilling.

In this example, a model will be created with identical parameters to an experiment run by Walton et al. (2015 a). A tall steel bridge was the basis for an experiment to determine buried arch structure's response to loading due to construction and applied patches. The parameters given in Table A.1 will be used in the model.

Table A.1 - Structural Properties of Model Buried Arch

Material	2 Layer Carbon
Elastic Modulus	29000 ksi
Cross Sectional Area	6 in
Moment of Inertia	1.125 in ⁴
Span Length	20 ft
Span Rise	7.5 ft
Arch Spacing	30 in
Apex Soil Cover	24 in
Soil Lift Height	8 in
Soil Friction Angle	44°
Soil Density	140 pcf
Soil Compaction Level	Dense
Arch Boundary Conditions	Fixed

A line load was simulated by loading a box beam with a length equal to the width of the soil box at the top of soil. This will be applied to *CBAS Design* using the load configuration given in Table A.2. For the analysis, 80 arch elements were used.

Table A.2 - Load Configuration of Model Buried Arch

Number of Patch Loads	1
Load Magnitude	18.75 kips
Load X Position	0 in
Load Z Position	0 in
Load Length	6 in
Load Width	84 in

Arch moments and vertical displacements are compared between *CBAS Design*, the research model, and the experiment. Figure A.5 through Figure A.8 compare the moments and displacements versus the percent of arch length. Figure A.5 and Figure A.6 are taken at the end of backfilling, while Figure A.7 and Figure A.8 are effects due to just

the applied patch load. The research model and *CBAS Design* follow the same trend in each comparison. The backfill moments at the apex is predicted by the models are enveloped by the experimental data. Shoulder moments at the end of backfill are over-predicted by 17% using *CBAS Design* and by 13% using the research model. The controlling load case due to an applied load is the apex moment, varying 2% in both models from the experimental results. The deflections calculated in both models trend in the same direction as the experimental value but fall short in accurately predicting the vertical displacements.

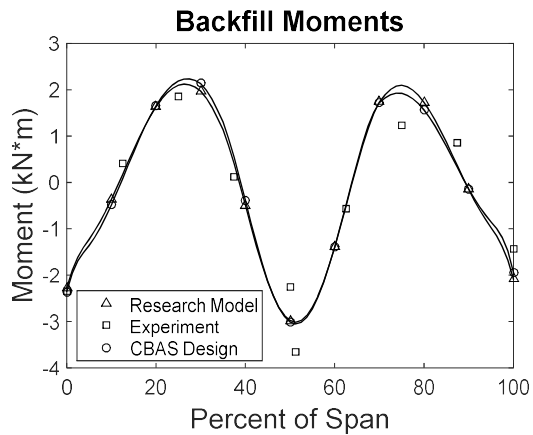


Figure A.5 Tall Arch Backfill Moments

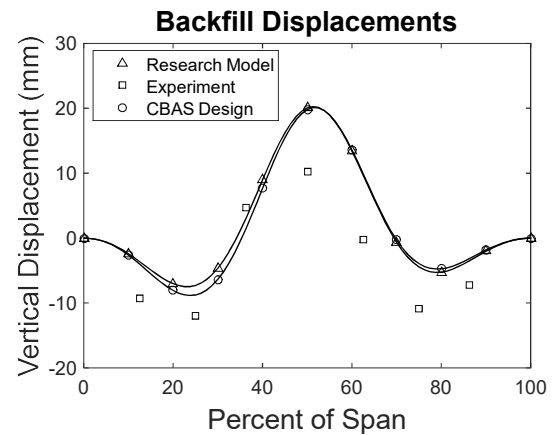


Figure A.6 Tall Arch Backfill Displacements

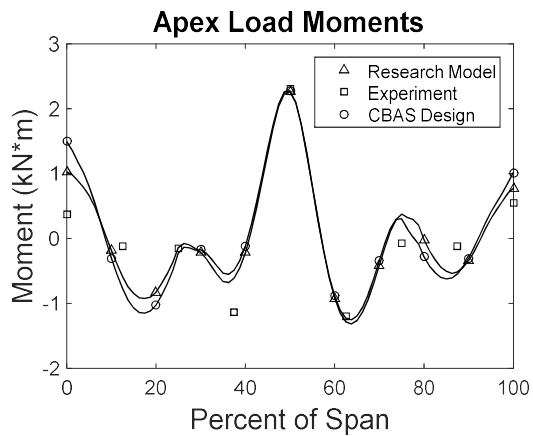


Figure A.7 Tall Arch Apex Load Moments

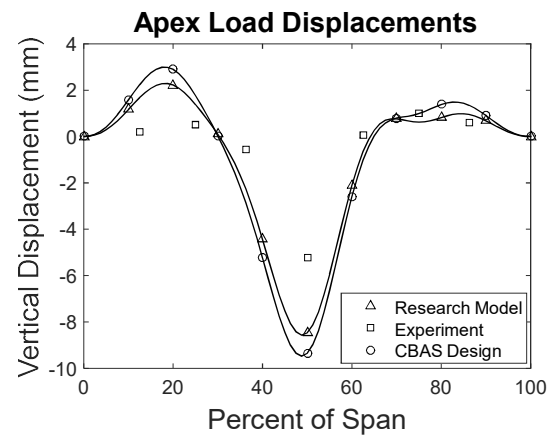


Figure A.8 Tall Arch Apex Load Displacements

Step by Step Example

In this section the step by step process will be detailed for an example structure with the properties given in Table A.3 and Table A.4.

Table A.3 - Structural Properties for Example

Material	2 Layer Carbon
Concrete Strength	6 ksi
Tube Diameter	12 in
Span Length	38 ft
Span Rise	9.5 ft
Arch Spacing	36 in
Apex Soil Cover	36 in
Soil Lift Height	12 in
Soil Friction Angle	37°
Soil Density	131 pcf
Soil Compaction Level	Dense
Arch Boundary Conditions	Fixed
Number of Elements	60

Table A.4 - Load Configuration for Example

Number of Patch Loads	1
Load Magnitude	20 kips
Load X Position	0 in
Load Z Position	0 in
Load Length	30 in
Load Width	30 in

The first tab visible when opening *CBAS Design* is the *Structural Properties*. In the *Arch Properties* panel select the 2 Layer Carbon, 6 ksi Fpc, 12 inch diameter material in the *Select Layup* popup menu. Enter a span of 38 feet into the text box. The figure changes as properties are entered as well as the Span to Rise Ratio to depict the structure being analyzed. Enter a rise of 9.5 feet and spacing of 36 inches into the correct text boxes.

In the *Soil Properties* panel enter the values for *Apex Soil Cover*, *Lift Height*, *Friction Angle*, and *Soil Density* into the text boxes. In Figure A.9 below, the *Elevation View of the Structure* will depict the NCHRP soil relationship between lateral earth

pressure and element movement corresponding to the soil friction angle and level of compaction entered (Barker et al., 1991). In the *Boundary Conditions* panel, the *Fixed* option is already selected. The Structure Properties tab should look similar to the screenshot below in Figure A.9.

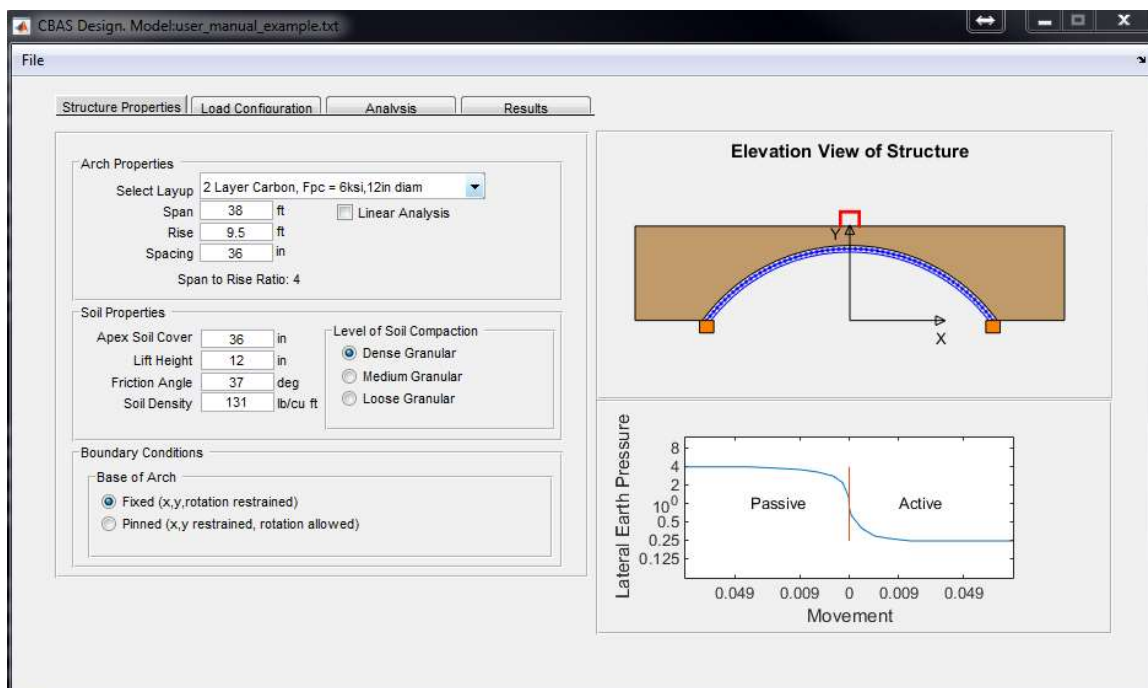


Figure A.9 Structure Properties, Example Verification

Switch to the *Load Configuration* tab to enter the loads to apply to the structure. One patch is already selected in the dropdown menu. Enter the load magnitude, x position, z position, patch length, and patch width in the table in that order. As seen in Figure A.10, both images to the right will change to represent the applied patch.

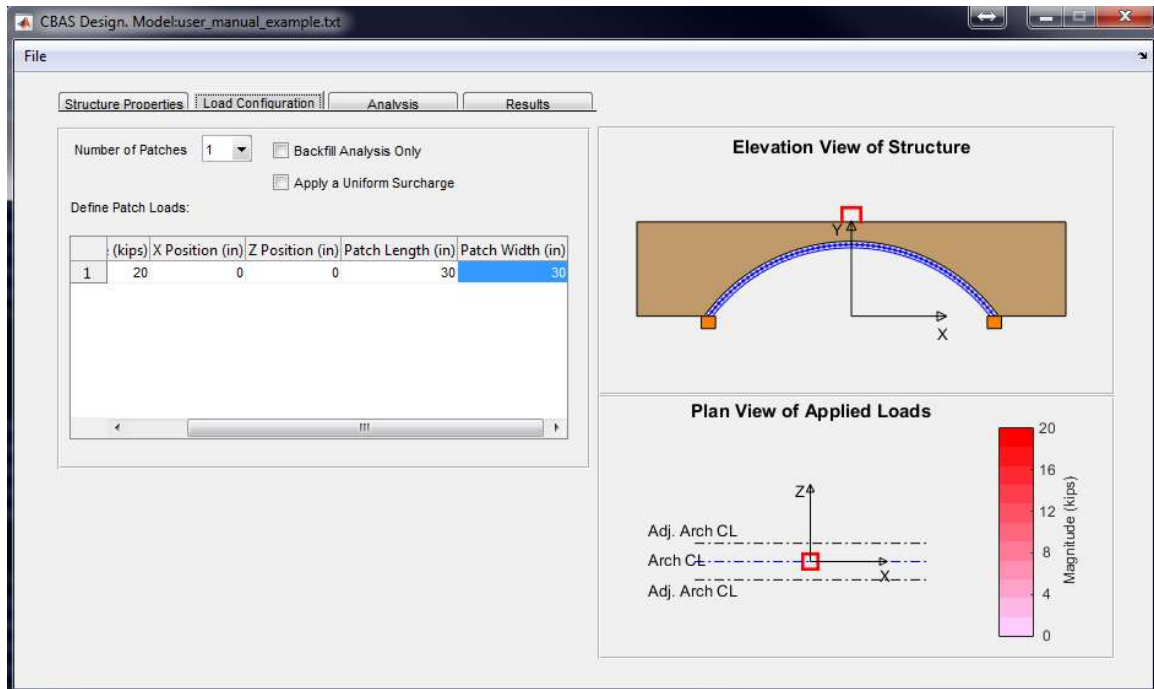


Figure A.10 Load Configuration, Example Verification

In the *Analysis* tab, shown in Figure A.11, change the number of *Elements in Arch* to 60. The default analysis is a *Large Deformation Analysis*, which will more accurately calculate the nodal displacements using a large deformation solver.

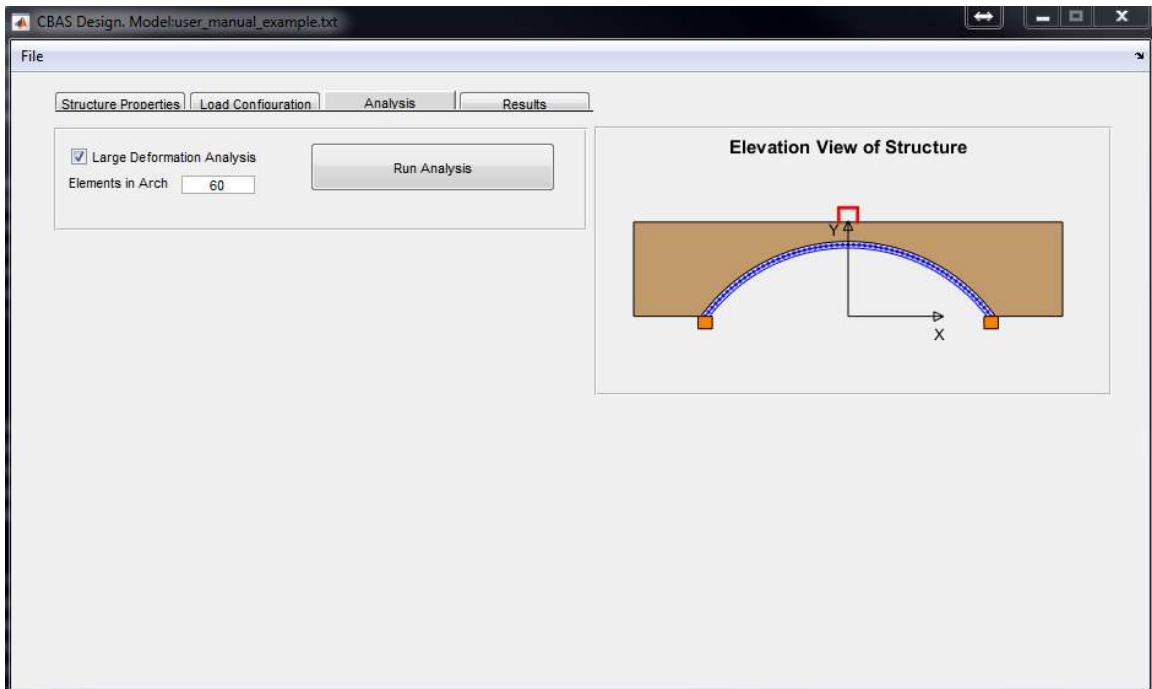


Figure A.11 Analysis, Example Verification

Clicking the *Run Analysis* button prompts the user to enter a name for the model if it hasn't already been saved. While the analysis is running, the figure will change to show where the solver is

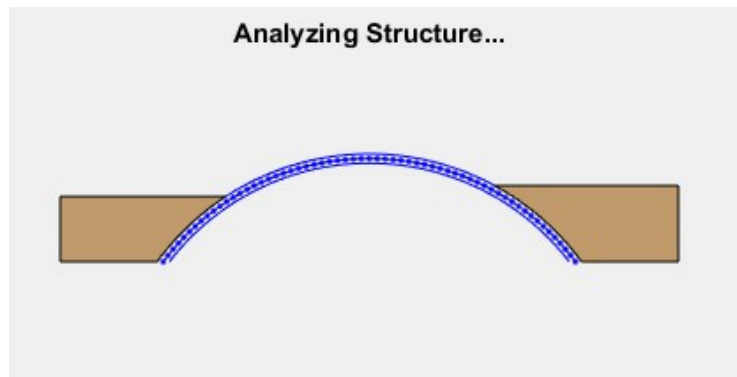


Figure A.12 Analysis in Progress

currently in the backfilling sequence. In Figure A.12, it can be seen that the backfill height is half of the arch height.

The *Results* tab will be clickable after the analysis is complete allowing the user to review total member moments, shears, and axial forces as well as the displaced shape for the arch for each step in the analysis process, as in Figure A.13.

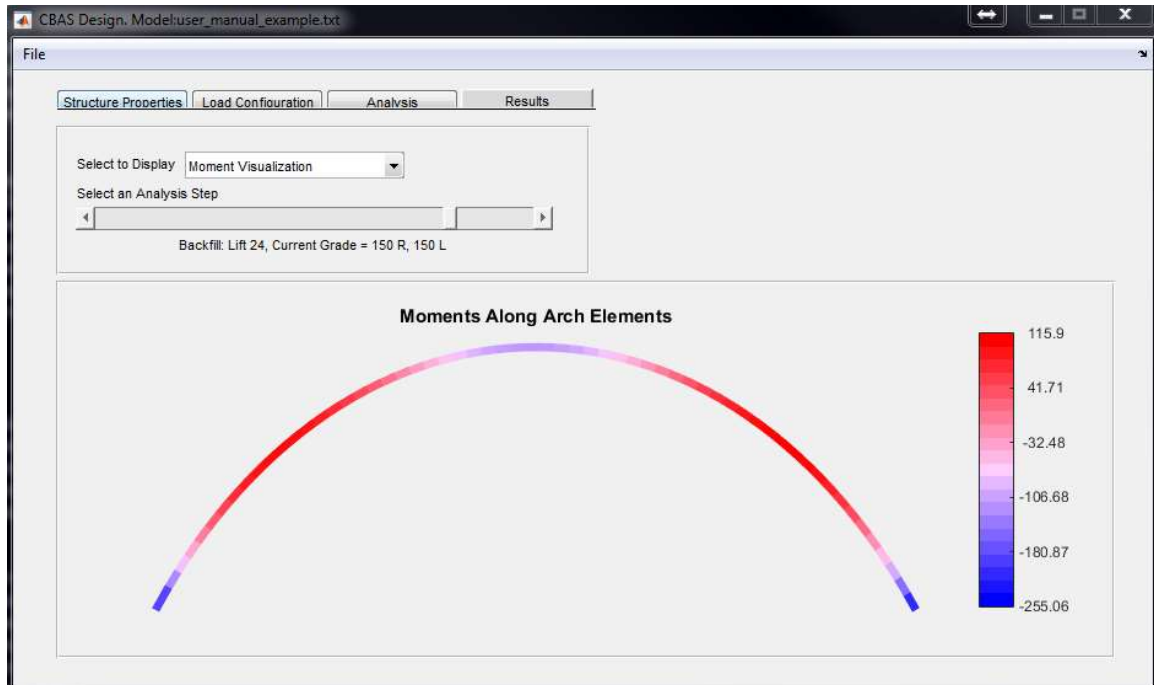


Figure A.13 Results Tab, Moment Visualization

Output Database Description

After each model has run, an output database is created that contains results in separate files. Member forces, nodal displacements, and soil pressures and forces are contained in a folder titled `model_name_results`. Each row in the tab files represents a node, the columns represent the analysis step. The following can be located in the results folder as .tab files:

- *Moment* - kip*inches.
- *Axial force*- kips
- *Shear force*- kips
- *Complete nodal displacements*- inches and radians
- *Vertical nodal displacements*- inches
- *Horizontal nodal displacements*- inches
- *Lateral earth pressure coefficients*- unit-less
- *Vertical soil pressure*- ksi
- *Vertical soil force*- kips
- *Horizontal soil pressure*- ksi
- *Horizontal soil force*- kips

Along with these results, a text file is included that shows each step in the analysis as well as time of completion. This file is named, `model_name_analysis_statistics.txt`.

Input File Description

The input file is an ASCII text file containing all variables required by the software to run an arch analysis. The file is automatically generated when a model is saved or run. An input file can be created by hand, but it is recommended that the user let the software write the file. This is due to the software's inability to check the values from an input file to be within the limits enforced by the user interface when the file is loaded which can result in inaccurate or non-converging models. There are two general formats that the software uses when creating an input file. For a nonlinear model, the following input file format is used. However if the model is linear, the software will use the input file format seen on the following page. Two examples of input files can be seen on the following pages. Note that after the `*Run a Linear Analysis` line, the next three values represent different properties in each case. Also, of more than one patch load is applied to the structure the last line of the input file repeats for each load.

*Input file for...user_manual_example
*Large Deformation Analysis Indicator
1
*Run a Linear Analysis
0
*Moment Curvature Relationship
Type3Fpc6_mphi.xlsx
*Diameter of Cross Section
11.79
*Fpc, Compressive Strength of Concrete
6
*Arch Rise
9.5
*Arch Span
38
*Arch Spacing
36
*Depth of Soil Cover
36
*Lift Height
12
*Soil Properties Friction Angle
37
*Soil Properties Level of Compaction
1
*Soil Density
131
*Number of Elements in Arch
60
*Boundary Condition, 1 for pinned, 0 for fixed
0
*Applied Surcharge
0
*Number of Applied Live Load Patches
1
*Patch Loads
8 0 0 10 20

*Input file for... linear_example
*Large Deformation Analysis Indicator
1
*Run a Linear Analysis
0
*Elastic Modulus of Structure
4286
*Area of Cross Section
112
*Moment of Inertia
1011
*Arch Rise
9.5
*Arch Span
38
*Arch Spacing
36
*Depth of Soil Cover
36
*Lift Height
12
*Soil Properties Friction Angle
37
*Soil Properties Level of Compaction
1
*Soil Density
131
*Number of Elements in Arch
60
*Boundary Condition, 1 for pinned, 0 for fixed
0
*Applied Surcharge
0
*Number of Applied Live Load Patches
1
*Patch Loads
8 0 0 10 20

USER'S MANUAL REFERENCES

- Barker, R.M., Duncan, J.M., Rojiani, K.B., Ooi, P.S.K., Tan, C.K., Kim, S.G. (1991). "NCHRP 343: *Manuals for the design of bridge foundations.*" Transportation Research Board, Washington D.C.
- Clough, G.W., Duncan, J.M. (1990). "Earth pressures." *Foundation Engineering Handbook*, 2nd ed., editor: Fang H.S., Van Nostrand Reinhold, Norwell MA, 224-235.
- Holtz, R.D., Kovacs, W.D. (1981) *An Introduction to Geotechnical Engineering*, Prentice Hall, Upper Saddle River, New Jersey.
- MATLAB (2014), MATLAB R2014b 8.4.0.150421, The MathWorks Inc., Natick, Massachusetts.
- Walton, H.J, Davids, D.G., Landon, M.E., Clapp, J.D. (2015a) "Experimental Evaluation Buried Arch Bridge Response." Submitted to the ASCE *Journal of Bridge Construction*.
- Walton, H.J, Davids, D.G., Landon, M.E., Clapp, J.D. (2015b) "Simulation Buried Arch Bridge Response." Submitted to the ASCE *Journal of Bridge Construction*.

BIOGRAPHY OF THE AUTHOR

Leo Nicolaas Helderma was born in Willcox, Arizona on August 5, 1992. The son of Nic and Janet Helderma, Leo grew up in Willcox. His family moved to Madison, Maine in 2006 and Leo graduated from Madison Area Memorial High School in 2010. Leo enrolled at the University of Maine, fall, 2010 and earned a B.S. in Civil Engineering, May, 2014. Leo began his graduate studies at the University of Maine in the fall of 2014, and is currently planning to graduate with a M.S. in Civil Engineering in May 2016. He is a candidate for the Master's degree in Civil Engineering from the University of Maine in May 2016.